

FINAL REPORT

Coupled Diffusion and Reaction Processes in Rock Matrices: Impact on Dilute Groundwater Plumes

SERDP Project ER-1685

DECEMBER 2015

Charles Schaefer
CDM Smith

Rachel Towne
David Lippincott
CB&I Federal Services

Hailiang Dong
Miami University

Distribution Statement A
This document has been cleared for public release



This report was prepared under contract to the Department of Defense Strategic Environmental Research and Development Program (SERDP). The publication of this report does not indicate endorsement by the Department of Defense, nor should the contents be construed as reflecting the official policy or position of the Department of Defense. Reference herein to any specific commercial product, process, or service by trade name, trademark, manufacturer, or otherwise, does not necessarily constitute or imply its endorsement, recommendation, or favoring by the Department of Defense.

| | | | | | |
|---|--------------------|-----------------------|---------------------------------------|---|--|
| REPORT DOCUMENTATION PAGE | | | | <i>Form Approved OMB No. 0704-0188</i> | |
| <small>The public reporting burden for this collection of information is estimated to average 1 hour per response, including the time for reviewing instructions, searching existing data sources, gathering and maintaining the data needed, and completing and reviewing the collection of information. Send comments regarding this burden estimate or any other aspect of this collection of information, including suggestions for reducing the burden, to Department of Defense, Washington Headquarters Services, Directorate for Information Operations and Reports (0704-0188), 1215 Jefferson Davis Highway, Suite 1204, Arlington, VA 22202-4302. Respondents should be aware that notwithstanding any other provision of law, no person shall be subject to any penalty for failing to comply with a collection of information if it does not display a currently valid OMB control number.</small> | | | | | |
| PLEASE DO NOT RETURN YOUR FORM TO THE ABOVE ADDRESS. | | | | | |
| 1. REPORT DATE (DD-MM-YYYY) | | 2. REPORT TYPE | | 3. DATES COVERED (From - To) | |
| 4. TITLE AND SUBTITLE | | | | 5a. CONTRACT NUMBER | |
| | | | | 5b. GRANT NUMBER | |
| | | | | 5c. PROGRAM ELEMENT NUMBER | |
| 6. AUTHOR(S) | | | | 5d. PROJECT NUMBER | |
| | | | | 5e. TASK NUMBER | |
| | | | | 5f. WORK UNIT NUMBER | |
| 7. PERFORMING ORGANIZATION NAME(S) AND ADDRESS(ES) | | | | 8. PERFORMING ORGANIZATION REPORT NUMBER | |
| 9. SPONSORING/MONITORING AGENCY NAME(S) AND ADDRESS(ES) | | | | 10. SPONSOR/MONITOR'S ACRONYM(S) | |
| | | | | 11. SPONSOR/MONITOR'S REPORT NUMBER(S) | |
| 12. DISTRIBUTION/AVAILABILITY STATEMENT | | | | | |
| 13. SUPPLEMENTARY NOTES | | | | | |
| 14. ABSTRACT | | | | | |
| 15. SUBJECT TERMS | | | | | |
| 16. SECURITY CLASSIFICATION OF: | | | 17. LIMITATION OF ABSTRACT | 18. NUMBER OF PAGES | 19a. NAME OF RESPONSIBLE PERSON |
| a. REPORT | b. ABSTRACT | c. THIS PAGE | | | 19b. TELEPHONE NUMBER (Include area code) |

Contents

| | |
|--|-----|
| TABLE OF CONTENTS..... | i |
| LIST OF FIGURES | iii |
| LIST OF TABLES | iv |
| LIST OF ACRONYMS | v |
| ABSTRACT..... | 1 |
| Objectives | 1 |
| Technical Approach..... | 1 |
| Results..... | 2 |
| Benefits | 3 |
| 1. OBJECTIVES..... | 4 |
| 2. BACKGROUND | 6 |
| 2.1 Bedrock Matrix Diffusion..... | 6 |
| 2.2 Weathering and Redox Fronts | 7 |
| 2.3 Chemical Oxidants..... | 8 |
| 2.4 Ferrous Iron..... | 10 |
| 2.5 Impacts of Long-Term Exposure on Rock Matrix Reactions..... | 12 |
| 3. MATERIALS AND METHODS..... | 14 |
| 3.1 Overall Approach and Rationale..... | 14 |
| 3.2 Site Geology and Core Collection | 15 |
| 3.3 Groundwater Characterization | 21 |
| 3.4 Rock Characterization..... | 22 |
| 3.5 Diffusion and Reaction Experiments - Rock Outside TCE Plume | 25 |
| 3.6 Diffusion and Reaction Experiments - Rock Within TCE Plume | 33 |
| 3.7 Contaminant Profiles in Rock Matrices..... | 39 |
| 3.8 Assessment of Abiotic Reaction with EDB..... | 42 |
| 3.9 Model Development to Assess Diffusion and Reaction in Rock Matrices..... | 43 |
| 4. RESULTS & DISCUSSION: | 48 |
| 4.1 Intact Rock Core Collection – Phase I..... | 48 |
| 4.2 Groundwater Characterization | 53 |
| 4.3 Rock Characterization..... | 54 |
| 4.4 Diffusion Experiments - Outside the TCE Plume | 60 |
| 4.5 Diffusion Experiments - Rock Collected Within the TCE Plume | 86 |
| 4.6 Contaminant Profiles in Rock Matrices..... | 92 |
| 4.7 Assessment of Abiotic Reaction with EDB..... | 94 |
| 5. CONCLUSIONS AND IMPLICATIONS FOR FUTURE RESEARCH | 97 |
| 6. LITERATURE CITED | 100 |



| | |
|--|-----|
| APPENDIX A: SUPPORTING DATA | 105 |
| APPENDIX B: LIST OF PUBLICATIONS | 108 |

LIST OF FIGURES

| | |
|---|-----|
| Figure 2.2 Natural Redox Front Propagation in Bedrock | 8 |
| Figure 3.1 Experimental Approach, Broken Down by Task | 15 |
| Figure 3.2.2 The Naval Air Warfare Center (NAWC) in Trenton, NJ | 18 |
| Figure 3.2.3 Phase 2 rock core collection at (NAWC) in Trenton, NJ | 20 |
| Figure 3.5.3 Diffusion cell | 28 |
| Figure 3.5.6 Plastic dish used for permanganate diffusion experiment | 32 |
| Figure 3.6.5 Preparation of rock slices and disks for coupled diffusion/reaction experiments | 38 |
| Figure 3.6.6 Rock rods within epoxy-sealed 40 mL vials | 38 |
| Figure 4.1 SEM images along a mudstone core 36 ft. bgs | 50 |
| Figure 4.1.1 SEM images along a mudstone core 50 ft. bgs | 51 |
| Figure 4.1.2 SEM images along a mudstone core 43 ft. bgs | 52 |
| Figure 4.3.1 SEM images of normal and parallel orientations | 56 |
| Figure 4.4.2 Iodide diffusion data | 63 |
| Figure 4.4.2.2 Prediction of experimental data | 66 |
| Figure 4.4.3 Comparison of experimental data and model simulations for TCE | 67 |
| Figure 4.4.3.2 TCE and iodide concentrations | 71 |
| Figure 4.4.3.3 Approach used for estimating the available ferrous iron in each rock | 73 |
| Figure 4.4.3.4 Measured bulk first order rate constants | 73 |
| Figure 4.4.4 Sulfur profiles following sodium persulfate experiments | 73 |
| Figure 4.4.4.1 Carbon profiles following sodium persulfate experiments | 77 |
| Figure 4.4.4.2 Manganese profiles following permanganate experiments | 78 |
| Figure 4.4.4.3 Carbon profiles | 81 |
| Figure 4.4.4.4 SEM-EDS elemental maps showing the distributions of C, O, K, Mn, and Fe | 82 |
| Figure 4.5.2 Comparison of abiotic degradation of TCE in TCE-spiked and un-spiked samples | 88 |
| Figure 4.5.3 Abiotic TCE degradation in the TCE-spiked samples | 91 |
| Figure 4.6 PCE concentration profiles into rock matrix for Loring and Edwards AFB | 93 |
| Figure 4.6.1 Abiotic PCE dechlorination at Loring and Edwards AFB | 94 |
| Figure 4.7.2 Abiotic EDB degradation for light grey mudstone | 96 |
| Figure 4.7.3 Abiotic EDB degradation for red sandstone | 96 |
| Figure A.1 Prediction of iodide diffusion using Eq. 3.9.1 | 105 |
| Figure A.2 Generation of daughter products shown for one experiment for each rock | 106 |
| Figure A.3 SEM images and EDS spectra of permanganate-reacted surfaces | 107 |

LIST OF TABLES

| | |
|---|----|
| Table 4.1. Results of bromide tracer testing in rock matrices | 49 |
| Table 4.2. Results of groundwater characterization..... | 53 |
| Table 4.2.1. Composition of Synthetic groundwater (SGW) recipes | 54 |
| Table 4.3.1. Rock mineralogy and porosity | 57 |
| Table 4.3.4. Rock total organic carbon (TOC) and rock permanganate oxidant demand | 59 |
| Table 4.3.5. Total oxidant demand per rock | 60 |
| Table 4.4.1 Partition coefficient (K) and matrix retardation factor (R) for iodide | 61 |
| Table 4.4.1.2. Partition coefficients (K) and matrix retardation factors (R) for TCE | 62 |
| Table 4.4.2.1. Measured iodide effective diffusion coefficients..... | 63 |
| Table 4.4.2.2. Characterization of rock porosities | 65 |
| Table 4.4.3. Coupled TCE diffusion and reaction | 69 |
| Table 4.4.3.1. Comparison of rock mineralogy before and after exposure to TCE..... | 76 |
| Table 4.4.4.1. Permanganate D_{obs} values and effective diffusion coefficients | 80 |
| Table 4.4.4.2. D_{eff} values prior to oxidant exposure compared to D_{eff} after exposure to oxidant | 80 |
| Table 4.4.4.3. Mineralogy on permanganate reactive surfaces of sedimentary rocks | 85 |

LIST OF ACRONYMS

| | |
|--------|--|
| AFB | Air Force Base |
| DCE | <i>cis</i> -1,2-dichloroethene |
| DHC | <i>Dehalococcoides</i> sp. |
| DNAPL | dense non-aqueous phase liquid |
| DO | dissolved oxygen |
| DoD | Department of Defense |
| EDB | ethylene dibromide |
| EELS | electron energy loss spectroscopy |
| FID | flame ionization detector |
| ft bgs | feet below ground surface |
| GC | gas chromatograph |
| HPLC | high-performance liquid chromatography |
| ISCO | <i>in situ</i> chemical oxidation |
| MNA | monitored natural attenuation |
| NAWC | Naval Air Warfare Center |
| NCBC | Naval Construction Battalion Center |
| NOD | natural oxidant demand |
| PCE | tetrachloroethene |
| SGW | synthetic groundwater |
| SEM | scanning electron microscopy |
| TCE | trichloroethene |
| TOC | total organic carbon |
| VC | vinyl chloride |
| VOC | volatile organic compound |
| XPS | x-ray photoelectron spectroscopy |
| XRD | x-ray diffraction |

Abstract

Objectives

The overall goal of this research was to measure and evaluate the impacts of bedrock structure and mineralogy on the persistence and diffusive flux of trichloroethene (TCE) from rock matrices to groundwater, and to verify that abiotic dechlorination reactions capable of significantly reducing monitored natural attenuation (MNA) time frames actually occur in the field within bedrock matrices. Rates of abiotic chlorinated ethene degradation due to reaction with naturally occurring ferrous minerals within the rock matrices were compared to the rate of diffusive flux through the rock matrix. The impact of this degradation on attenuation timeframes subsequently was assessed.

The specific objectives of this project were as follows:

- Measure and evaluate the effective diffusivity of TCE in the rock matrix as a function of rock type, mineralogy, and orientation of mineral bedding planes;
- Measure and evaluate the rate and extent of abiotic dechlorination in TCE-impacted rock matrices and how rock mineralogical and physical properties affect these processes;
- Measure and evaluate the coupled diffusion and reaction of chemical oxidants into rock matrices;
- Determine the impact of chemical oxidation fronts emanating from the fracture plane on rock structure and mineralogy, and ultimately on the diffusion and reaction of TCE from the rock matrix;
- Identify the rate of TCE dechlorination due to the presence of ferrous iron in the rock matrix;
- Measure and evaluate the rate and extent of abiotic dechlorination of additional volatile organic compounds (e.g., chlorinated ethanes) in rock matrices and how rock mineralogical and physical properties affect these processes;
- Develop and validate a conceptual and mathematical model to describe the above processes for the purpose of providing improved estimates of timeframes for which matrix diffusion can sustain a contaminant groundwater plume.

Technical Approach

Our approach for measuring and evaluating the impacts of bedrock structure and mineralogy on the persistence and diffusive flux of TCE from rock matrices to groundwater consisted of a series of diffusion and reaction experiments performed on intact rock cores collected from DoD facilities. Rocks were first assessed for mineralogy, porosity, and pore structure. Diffusion experiments were performed using a modified diaphragm cell technique, as described in detail by Boving and Grathwohl (2001) and Cussler (1984). Diffusive flux of tracers and TCE, coupled

with the abiotic reaction of TCE in rock matrices, were measured for multiple rock types. Experiments were performed on both pristine (i.e., no historical TCE impacts) and TCE-impacted (i.e., exposed to TCE for decades) rock to assess the extent to which the measured abiotic dechlorination reactions are occurring *in situ* at TCE-contaminated bedrock sites. The relative importance of these reactions in rock matrices at the field scale were assessed by comparing reaction and diffusion timescales.

To verify the extent to which application of *in situ* chemical oxidation can be effective for treating TCE mass within the rock matrix, additional experiments were performed with permanganate and persulfate. In these oxidant experiments, the migration of oxidant into the rock matrix was measured as a function of rock type, and the impact of oxidant exposure on the effective diffusion coefficient was subsequently determined. Both the extent of oxidant migration into the rock, and the impact of oxidant exposure on the effective diffusion coefficient, will play a large role in the overall effectiveness of *in situ* chemical oxidation in fractured bedrock where contaminant uptake into the rock matrix is substantial.

Results

Results from the diffusion experiments showed that the orientation of mineral bedding relative to the direction of diffusion could have a substantial impact on the diffusive flux. By attaining a measurement of the rock matrix porosity in the orientation of the diffusion gradient, a reasonable prediction of the effective diffusion coefficient was attained.

Experiments examining the coupled diffusion and reaction of TCE in rock matrices showed that, for all rock types examined, measureable abiotic dechlorination occurred within the rock matrices. Abiotic reactions, which generated ethene, ethane, acetylene, and/or propane, were well described by a first-order rate constant. The observed first-order rate constants for the various rock types were related to the ferrous mineral content of the rock that was in contact with the rock matrix porosity. The observed rate constants in rock that been exposed to TCE for decades were on the same order of magnitude as rate constants observed in rocks that had no known prior exposure to TCE, suggesting that these reactions likely are occurring *in situ* in bedrock plumes. Furthermore, results show that the measured rates of reaction are significant when considering the time and length scales of matrix diffusion in the field.

Oxidant penetration into the rock matrix over a two month period was on the order of 100 microns. This diffusional migration was well predicted based on the measured effective diffusion coefficient and oxidant demand for each rock type examined. Furthermore, manganese oxide precipitate coating of the rock matrix did not provide a significant diffusion barrier. Thus,

the use of chemical oxidants is unlikely to be effective for treating chlorinated ethene contaminants within rock matrices, or in mitigating matrix back diffusion.

Benefits

This research has resulted in improved approaches, both experimental and conceptual, for estimating contaminant flux and longevity in rock matrices. Identifying and quantifying the abiotic dechlorination reactions in rock matrices have highlighted an important attenuation mechanism in fractured bedrock aquifers that are impacted by chlorinated solvents. Results of this study suggest that, at least for some bedrock sites where ferrous iron minerals are present within the rock matrices, abiotic reaction in rock matrices may serve as an important mechanism for mitigating the adverse impacts of matrix back diffusion on plume intensity and longevity. This research highlights the importance of understanding these diffusion and reaction processes for improved insight into managing chlorinated solvent plumes in fractured bedrock aquifers.

1.0 Objectives

The SERDP Statement of Need (ERSON-09-01) addressed the need to improve management and reduce uncertainty associated with large, dilute groundwater contaminant plumes. The demonstration of relatively slow attenuation mechanisms and improved understanding of the processes responsible for sustaining chlorinated solvent plumes were identified as targeted areas of interest. The overall goal of this research was to measure and evaluate the impacts of bedrock structure and mineralogy on the persistence and diffusive flux of trichloroethene (TCE) from rock matrices to groundwater, and to verify that abiotic reactions capable of significantly reducing monitored natural attenuation (MNA) time frames are actually occurring in the field within bedrock matrices. The impacts of oxidation fronts (generated naturally or via *in situ* chemical oxidation) between the fracture and matrix on these processes were investigated, and TCE dechlorination kinetics via ferrous iron minerals within the rock also were evaluated. Rates of abiotic chlorinated ethene degradation due to reaction with naturally occurring ferrous minerals within the rock matrices were compared to the rate of diffusive flux through the rock matrix.

We hypothesized that mineralogy and bedding would have a substantial impact on TCE fate and transport within rock matrices. Experiments were performed using bedrock cores collected from non-impacted as well as TCE-impacted locations within DoD sites, and conceptual/mathematical models were validated based on laboratory data. The specific objectives of this project were as follows:

- Measure and evaluate the effective diffusivity of TCE in the rock matrix as a function of rock type, mineralogy, and orientation of mineral bedding planes;
- Measure and evaluate the rate and extent of abiotic dechlorination in TCE-impacted rock matrices and how rock mineralogical and physical properties affect these processes;
- Measure and evaluate the coupled diffusion and reaction of chemical oxidants into rock matrices;
- Determine the impact of chemical oxidation fronts emanating from the fracture plane on rock structure and mineralogy, and ultimately on the diffusion and reaction of TCE from the rock matrix;
- Identify the rate of TCE dechlorination due to the presence of ferrous iron in the rock matrix;

- Measure and evaluate the rate and extent of abiotic dechlorination of ethylene dibromide (EDB) in rock matrices and how rock mineralogical and physical properties affect these processes;
- Develop and validate a conceptual and mathematical model to describe the above processes for the purpose of providing improved estimates of timeframes for which matrix diffusion can sustain a contaminant groundwater plume.
- Determine how abiotic processes are contributing to natural attenuation, and can the rates and extent of attenuation be predicted for incorporation into site fate and transport models.

The scope of work was designed to directly measure 1) diffusion of tracers, TCE, and oxidants into the rock matrix, 2) geochemical and physical impacts of chemical oxidation on the rock matrix and matrix-fracture interface, 3) abiotic dechlorination rates of TCE and other VOCs in rock matrices, and 4) measuring the rates of TCE diffusion and reaction that are occurring in the bedrock matrices at TCE-impacted DoD sites. These experiments facilitated the development of a conceptual and mathematical model that can be used to predict source longevity and long term impacts to groundwater quality after sources and flux emanating from bedrock fractures have been significantly reduced, and can be used as a tool to evaluate the fate of dilute contaminant plumes; the developed bedrock matrix diffusion/reaction model is best applied within the framework of a site-wide fate and transport model. In addition, verification and quantification of these processes, and the substantial natural attenuation resulting from ferrous minerals in rock matrices, has the potential to serve as a basis for natural attenuation remedies at several DoD facilities.

Improved understanding regarding these coupled diffusion and reaction processes is needed so that the resultant long-term impacts of contaminant mass in rock matrices on groundwater quality can be quantified and predicted. Specifically, this research addressed the following questions: 1) How does rock mineralogy (bedding plane and oxidation fronts) impact diffusive flux of chlorinated solvents from the rock matrix to adjacent fracture zones?; 2) What impacts do chemical oxidants, delivered to bedrock fractures, have on rock mineralogy and contaminant flux from the adjacent rock matrix?; 3) What are the rates of ferrous iron-induced reductive dechlorination in rock matrices?; 4) How do these processes impact the longevity and intensity of dilute groundwater plumes?; 5) How can naturally occurring attenuation process in rock matrices best be determined?; and 6) How are these abiotic processes contributing to natural attenuation, and can the rates and extent of attenuation be predicted for incorporation into site fate and transport models?

2.0 Background

2.1 Bedrock Matrix Diffusion

Several studies have demonstrated that, following removal of chlorinated solvent sources from fractured zones in bedrock, contaminant diffusion from the rock matrix can sustain the groundwater plume for a relatively long period of time (Mutch et al., 1993; Goldstein et al., 2004; Lipson et al., 2005). Thus, estimation of the effective diffusion coefficient through the bedrock matrix is critical for predicting the long-term flux of contaminants from the rock to groundwater, and for estimating natural attenuation timeframes. Studies performed by Boving and Grathwohl (2001) and Polak et al. (2002) show that contaminant diffusion through the rock matrix can be reasonably estimated based on the porosity of the rock matrix. Their results indicate that the effective diffusion coefficient (D_{eff}) through the bedrock matrix can be estimated as follows:

$$D_{\text{eff}} = D_{\text{aq}} \varepsilon^m \quad (2.1)$$

Where D_{eff} is the effective diffusion coefficient [cm^2/s], D_{aq} is the aqueous phase diffusivity [L^2/t], ε is the physical matrix porosity, and m is an empirical coefficient, which was found to be approximately 2.

Although Equation 2.1 provides a useful approximation, estimating effective diffusion coefficients in rock matrices is complicated by the heterogeneous structure and geochemistry of the bedrock. Studies performed by Tidwell et al. (2000) and Wersin et al. (2004) have shown that the presence of rock bedding planes can have a substantial impact on diffusion, and that relatively simple correlations relating the effective diffusivity to overall matrix porosity are insufficient for describing diffusive flux through rock. The relevance of bedding plane orientation and diffusive flux is particularly important at the aquifer scale, as the presence of both vertical and horizontal fractures will intersect bedding planes at different angles. Samper et al. (2006) and Wersin et al. (2004) showed that the effective diffusion coefficient was several times greater when diffusion occurred parallel to bedding compared to diffusion normal to bedding for anisotropic claystones. Cavé et al. (2010) showed that the effective diffusion coefficient was 2 to 3-times greater parallel to bedding than normal to bedding. Comparison of the solute-effective porosity to the effective diffusion coefficient in each orientation did not reveal any correlation. Applying Eq. (2.1) to their data, Cavé et al. (2010) showed that an exponent (m) of 2 to 2.5 was appropriate for diffusion parallel to bedding, while an exponent of 2.5 to 3 was appropriate for diffusion perpendicular to bedding.

Nakashima et al. (2008) employed a combination of X-ray computed tomography (CT) and diffusion simulations to evaluate porosity and diffusion in anisotropic rocks. Results showed that pore anisotropy controlled diffusion. Furthermore, diffusion could be greater in either the parallel or normal orientation. *However, to the best of our knowledge, a comprehensive study has not been performed to quantitatively evaluate the impacts of rock bedding plane orientation on diffusive flux from rock matrices. The objective of this study was to measure and compare the effective diffusion coefficient and apparent porosity (or, pore cross-sectional area) of both normal and parallel to bedding in several sedimentary rocks.*

2.2 Weathering and Redox Fronts

The geochemical structure and nature of bedrock often varies as a function of distance from a prominent fracture interface as weathering and oxidation processes proceed from the fracture interface inwards through the rock matrix. For example, Landström et al. (2001) showed that erosion and weathering impacted rock matrix properties (i.e., increased porosity) within approximately 2.5 cm of the fracture interface. Marcos et al. (2001) showed that matrix porosity in oxidized or “weathered” zones were greater than the porosity in “un-weathered” zones by approximately a factor of two. In contrast, studies by Akagawa et al. (2006) showed that porosity was reduced in weathered zones due to formation of ferric iron precipitates. Other studies (Fu et al., 1994; Dong et al., 2003; USEPA, 2006) have shown that mineral and/or organic coatings can form on fracture surfaces, potentially reducing diffusional flux across the fracture-matrix interface. Mazurek et al. (1996) showed that fractures within shales were coated with birnessite and gypsum. Thus, the impacts of weathering and mineral precipitation on rock characteristics are complex and likely vary for differing rock types.

Yoshida et al. (2006) showed that naturally-occurring redox fronts often exist at the fracture-rock interface, as indicated by the transition of ferrous to ferric iron within the rock. Figure 2.2 below shows a picture of the redox front observed in their work, with an impacted zone of approximately 15 cm from the fracture interface. Mazurek et al. (1996) showed similar results, as the shale matrix near fracture faces consisted of goethites and iron oxyhydroxides (ferric iron species), but fresh (unweathered) rock residing away from the fracture interface did not contain these ferric iron species, but were apparently replaced with siderite (ferrous iron). Akagawa et al. (2006) considered the impacts of these redox fronts on radionuclide migration.

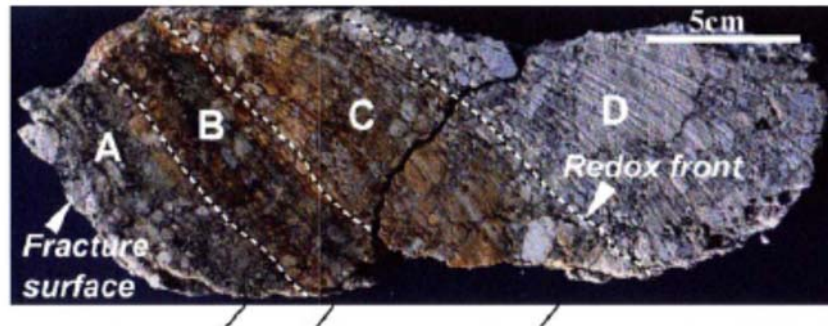


Figure 2.2 Natural redox front propagation in bedrock (picture taken from Yoshida et al., 2006).

These gradients are caused by the diffusion of oxidant (e.g., oxygen) from the rock fractures into the matrix, which occurs on geologic timescales. *Changes caused by this diffusive oxidation front can result in changes to the rock porosity (through mineral dissolution and precipitation), and ultimately to the diffusive flux and impact to groundwater (Steefel and Lichtner, 1994; Siitari-Kauppi et al., 1997; Sidborn and Neretnieks, 2007).* The impacts of these naturally occurring oxidation fronts and surface coatings have been studied, in part, with respect to their effects on radioactive waste migration through fractured rock systems. *However, impacts of these oxidation fronts on the diffusive release of chlorinated solvents and long term sustainability of groundwater plumes has not been examined, and current contaminant transport models do not take these phenomena into account.*

2.3 Chemical Oxidants

The weathering and oxidation processes occurring between fractures and rock matrices described in the previous paragraphs occur naturally on geologic timescales. Dissolved oxygen is a relatively mild oxidant, and changes to rock mineralogy occur slowly. However, during implementation of *in situ* chemical oxidation, relatively strong oxidants (e.g., permanganate, persulfate) are delivered into bedrock fractures. These oxidants come into direct contact with the surface of the rock matrix, and are able to enter the rock matrix itself via diffusion.

Chemical oxidants have been shown to oxidize naturally occurring ferrous minerals (Al et al., 2003; Honning et al., 2007). Thus, oxidation fronts (similar to those shown in Figure 2.2) also can occur in rock matrices as a result of implementing *in situ* chemical oxidation for treatment of chlorinated solvent sources in bedrock fractures. *In situ* chemical oxidation (ISCO) using strong oxidants (e.g., permanganate, persulfate, ozone, and hydrogen peroxide) have been effectively

applied for treatment of chlorinated solvents (Conrad et al., 2002; Krembs et al., 2010; Schnarr et al., 1998; Siegrist et al., 2011). Several studies have demonstrated that uptake and back-diffusion of contaminants from the bedrock matrix can have a substantial impact on contaminant fate and treatment potential (Goldstein et al., 2004; Lipson et al., 2005; Sterling et al., 2005; West and Kueper, 2010). In these instances, three key questions arise: ***1) What is the rate and extent of oxidant diffusion into the bedrock matrix, 2) What impact will the oxidant have on the rock structure/porosity and ultimately the back-diffusion of contaminant from deeper within the rock matrix to fracture zones, and 3) How do these processes ultimately impact contaminant fate & transport in large dilute plumes?***

Honning et al. (2007) showed that the rate of permanganate diffusion into clay was approximately 0.05 cm/day, which is several orders of magnitude greater than the rate of oxidation front movement due to natural processes in rocks; this difference in rate can not be explained by differences in porosity or the effective diffusion coefficient in the rock versus the clay, but rather by the oxidative potential of the permanganate. Honning et al. (2007) also showed that the rate of permanganate diffusion into oxidized (i.e., weathered) clay was 5-times greater than the rate of permanganate diffusion into reduced (i.e., ferrous iron containing) clay, due to the redox reaction between permanganate and ferrous iron containing clay. Together, these results demonstrate that matrix mineralogy can have a substantial impact on both the extent and rate of oxidant diffusion into the matrix. Al et al. (2007) showed that permanganate diffused into a shale rock, reacted with pyrite, and formed manganese oxide precipitates within the rock matrix. Due to substantial reaction of the permanganate with pyrite and the relatively low porosity of the shale, the diffusion distance was approximately 150 μm over one year duration. Other studies, based on the matrix oxidant demand and porosity, suggest that substantially greater rate of permanganate diffusion would be expected (Tunnicliffe and Thomson, 2004).

In addition to manganese oxides formed from the rock matrix mineralogy or naturally occurring organic carbon, chemical oxidation of organic contaminants (e.g., TCE) with permanganate also typically results in the formation of manganese oxide solids (Crimi and Siegrist, 2004). Loomer et al. (2010) studied the manganese oxidation state in manganese oxides formed by oxidation of TCE with permanganate using electron energy loss spectroscopy (EELS) and X-ray photoelectron spectroscopy (XPS). The authors found that the valence of manganese in such manganese oxides can vary from 2.2 to 3.6 depending on the amount of permanganate, pH, and aging (Loomer et al., 2010; Scott et al., 2011). This study raises the possibility that different manganese minerals can form depending on specific experimental conditions; however, the exact nature of such manganese solids remains unknown, especially in different rock types (e.g., mudstones vs. sandstones).

None of the studies described in the above paragraphs considered the impacts of geochemical transformation within the rock matrix or at the matrix-fracture interface. Specifically, the impacts of the oxidant on speciation of ferrous iron-containing minerals, rock porosity, and diffusivity were not monitored. In addition, these studies did not investigate the subsequent impact of chemical oxidation on the diffusive release of dissolved contaminants from the rock matrix. *To the best of our knowledge, no comprehensive studies have been performed to evaluate the impacts of oxidant type (e.g., permanganate, persulfate), oxidant dosage, or rock type on the rate of chlorinated solvent flux from bedrock matrices to fractures/groundwater following in situ chemical oxidation in fractured bedrock.* Thus, improved understanding of these processes are needed to estimate MNA timeframes and the intensity of groundwater plume concentrations following remedial activities in fractured bedrock, which may determine the extent to which *in situ* chemical oxidation be implemented in contaminated bedrock aquifers.

2.4 Ferrous Iron

In addition to the impacts of oxidation and rock mineralogy on matrix diffusion discussed in the previous sections, the presence of ferrous iron minerals in the rock matrix serves as a potential long-term dechlorination mechanism for dissolved chlorinated solvents such as TCE. Several studies have demonstrated that the presence of ferrous iron minerals such as pyrite, magnetite, chlorite, biotite, lepidocrocite, and siderite facilitate the reductive dechlorination of ethenes and ethanes (Weerasooriya and Dharmasena, 2001; Lee and Batchelor, 2002; Elsner, 2002; O'Loughlin and Burris, 2003; Wilson, 2007). Ferrous iron induced dechlorination of TCE typically occurs via a reductive beta-elimination pathway, with the formation of chloroacetylene. Chloroacetylene transforms very rapidly to form acetylene, which may be further reduced to ethene and ethane. Measured abiotic rate constants in natural ferrous-mineral containing soils were shown to be on the order of 1 yr^{-1} (Ferrety, 2004), which may result in a significant reduction in monitored natural attenuation (MNA) timeframes for some sites. Such abiotic processes may be the primary degradation mechanism where biological processes are not a significant contributor (Brown, 2007).

These abiotic reduction processes may be particularly important for sandstones and shales, which often contain significant quantities of ferrous iron within the rock matrix, and are common bedrock types found at DoD and DoE sites contaminated with chlorinated solvents. *Ferrous minerals are likely present in bedrock formations at several DoD chlorinated solvent sites, including South Weymouth Naval Air Station (biotite in the Dedham Granite formation), the Naval Air Warfare Center in Trenton, NJ (pyrite in the Lockatong formation), and Letterkenny Army Depot (chlorite in the Martinsburg formation).* However, while reductive

dechlorination via ferrous iron has been studied in unconsolidated media (e.g., clays, sands), we are unaware of any similar studies performed within rock matrices that contain ferrous minerals. The potential importance of ferrous-iron induced reductive dechlorination in rock matrices can be evaluated in terms of a dimensionless Damkohler (D_a) number, which is defined as:

$$D_a = \frac{kL^2}{D_{\text{eff}}} \quad (2.2)$$

where k is the first-order rate constant for reductive dechlorination via ferrous iron and L is the rock matrix diffusion length. Values of $D_a > 1$ suggest that the relative rate of reaction is large relative to the rate of diffusion. Assuming a ferrous iron dechlorination rate constant of 1×10^{-6} /sec (Lee and Batchelor, 2002; Elsner, 2002), a matrix diffusion length of 100 cm, an effective diffusion coefficient of 5×10^{-7} cm²/sec, and that the rock is composed of 1% (by weight) ferrous iron, the value for D_a is 200. ***This value of D_a suggests that ferrous iron reduction can potentially serve as a significant attenuation mechanism for dissolved chlorinated solvents diffusing through ferrous iron-containing rock matrices.*** Thus, improved insight into the extent and rates of ferrous iron dechlorination in rock matrices is needed to verify this critical attenuation parameter, and ultimately quantify its effects on the intensity and longevity of dilute groundwater plumes in bedrock aquifers.

The impacts of remedial processes on ferrous iron-facilitated reduction of TCE in rock matrices are currently unknown. ***Diffusion of oxidant into the rock matrix can oxidize ferrous minerals, potentially limiting the extent of ferrous iron reductive processes in rocks.*** In addition, implementation of bioremediation for treatment of sources located in bedrock fractures can facilitate diffusion of biologically reduced iron into the rock matrix (Yoshida et al., 2006). Previous studies have shown that addition of dissolved ferrous iron can substantially enhance ferrous mineral dechlorination rates of chlorinated ethenes (Lee and Batchelor, 2002). ***This result suggests that dissolved iron, which typically is generated during implementation of biostimulation for chlorinated solvents, will likely have a beneficial remedial impact on dechlorination kinetics as it diffuses into the rock matrix.*** Both chemical oxidation and bioremediation for removal of chlorinated ethene sources in fractures have been employed at many chlorinated solvent impacted bedrock sites. However, the potential impacts of these remedial technologies on relatively slow abiotic reductive dechlorination process in the rock matrices require additional study.

Based on the above discussions on diffusion and reaction processes in rock matrices, the need for additional studies to evaluate diffusion and reaction process in rock matrices is imperative. The consequences of remedial technologies such as *in situ* chemical oxidation and biostimulation on these processes are particularly important, as these processes could substantially impact diffusion

and reaction kinetics within the rock matrix. *It is expected that the study proposed herein will lead to improved fundamental understanding of transport and reaction processes within rock matrices, and ultimately to development of models that are able to predict both the short and long term contaminant flux from bedrock matrices to groundwater in bedrock aquifers.*

2.5 Impacts of Long-Term TCE Exposure on Rock Matrix Reactions

Dissolved TCE in bedrock matrices is one of the most persistent, and difficult to manage, groundwater sources of these contaminants. After removal of sources from conductive fractures, the back-diffusion of dissolved TCE from the low porosity and low permeability rock matrix can serve as a long term source. Studies have suggested that back-diffusion of contaminants from rock matrices to water-bearing fractures will likely inhibit attainment of remedial goals at many bedrock sites (Lipson et al., 2005; Seyedabbasi et al., 2012). Flux of the dissolved contaminants into adjacent water bearing fractures is controlled by diffusion through the rock matrix. The effective diffusivity, and corresponding diffusional flux, is low, thereby enabling rock matrices to serve as a long term contaminant source for the water bearing fractures. Because of the low permeability of the rock matrices, delivery of remedial amendments is difficult, which results in either limiting treatment to the conductive water fractures (which typically represents only a small fraction of the total rock porosity and contaminant mass) or applying an aggressive (and costly) technology such as thermal remediation. However, as noted by West and Kueper (2010), even relatively slow contaminant degradation within the rock matrix can have a substantial mitigating effect on the impacts of back-diffusion on the contaminant plume.

Several DoD facilities, including Edwards AFB, the former Naval Air Warfare Center (NAWC, Trenton, NJ), Loring AFB, Wartonvliet Arsenal, AFP4, and Redstone Arsenal, likely contain dissolved PCE and TCE sources in the bedrock matrices. No remedial technologies have been cost effectively applied to treat these sources. As a result, site managers have relied on containment technologies, or some other interim measure, to address the resultant plume.

Ideally, a monitored natural attenuation remedy would be desirable for PCE and TCE impacted bedrock matrices. However the attenuation processes within rock matrices are poorly understood, and obtaining direct measurements of any attenuation processes (e.g., reaction, diffusion, sorption) is difficult. Most traditional model predictions base contaminant attenuation for the rock matrices solely on diffusional flux. The resultant long remedial time frames from such models make a Monitored Natural Attenuation (MNA) approach unpalatable to most regulators. As such, management of contaminated bedrock aquifers continues to demand DoD resources and attention.

It has not been demonstrated that the abiotic ferrous iron-induced reactions described previously within this section are ongoing at bedrock sites that have been exposed to TCE for decades. Furthermore, it has not been demonstrated that such long-term reactions are occurring at rates that can reduce the mass of contamination available for back-diffusion. Such confirmation is critical, as determination as to whether such abiotic reactions are short lived (i.e., months to years) due to oxidation of ferrous iron minerals, or are long-lived (i.e., decades), have important implications for inclusion of such reactions in natural attenuation modeling of bedrock sites. As noted by Lipson et al.(2005), any degradation of TCE that might occur within the rock matrix could substantially reduce the time scales associated with the slow back-diffusion of the contaminants from the rock matrix. ***Demonstrating that additional attenuation processes in rock matrices are actually occurring in the field, and that these processes can substantially reduce both the impact of the TCE sources on the aquifer and the plume extent and duration will provide the DoD, stakeholders, and regulators with a verified approach for managing and ultimately closing these challenging sites.***

3.0 Materials and Methods

3.1 Overall Approach and Rationale

Our approach for measuring and evaluating the impacts of bedrock structure and mineralogy on the persistence and diffusive flux of TCE from rock matrices to groundwater consisted of a series of diffusion and reaction experiments performed on intact rock cores collected from DoD facilities. Rocks were first assessed for mineralogy, porosity, and pore structure. Diffusion experiments were performed using a modified diaphragm cell technique, as described in detail by Boving and Grathwohl (2001) and Cussler (1984). Diffusive flux of tracers and TCE, coupled with the abiotic dechlorination reaction of TCE in rock matrices, were measured for multiple rock types. Experiments were performed on both pristine (i.e., no historical TCE impacts) and TCE-impacted (i.e., exposed to TCE for decades) rock to assess the extent to which the measured abiotic dechlorination reactions are occurring *in situ* at TCE-contaminated bedrock sites. The relative importance of these reactions in rock matrices at the field scale were assessed by comparing reaction and diffusion timescales.

To verify the extent to which application of *in situ* chemical oxidation can be effective for treating TCE mass within the rock matrix, additional experiments were performed with permanganate and persulfate. In these oxidant experiments, the migration of oxidant into the rock matrix was measured as a function of rock type, and the impact of oxidant exposure on the effective diffusion coefficient was subsequently determined. Both the extent of oxidant migration into the rock, and the impact of oxidant exposure on the effective diffusion coefficient, will play a large role in the overall effectiveness of *in situ* chemical oxidation in fractured bedrock where contaminant uptake into the rock matrix is substantial.

Taking advantage of on-going research and remedial activities at fractured bedrock sites, the concentrations of PCE and TCE in rock matrices were measured as a function of distance from the face of a hydraulically conductive fracture; these fractures were impacted with PCE and/or TCE. Measured diffusion profiles into the rock matrices were compared to parallel batch testing where abiotic dechlorination rates were measured. This comparison provided additional insight into the importance of abiotic dechlorination reaction in rock matrices.

Finally, another volatile organic compound ethylene dibromide (EDB) was evaluated with respect to potential abiotic dehalogenation in rock matrices. Experiments were performed on the pristine rocks in a similar fashion to the previous rock experiments.

The overall approach for this project is outlined in Figure 3-1. Details of the methodologies for these approaches are provided in the following sections.

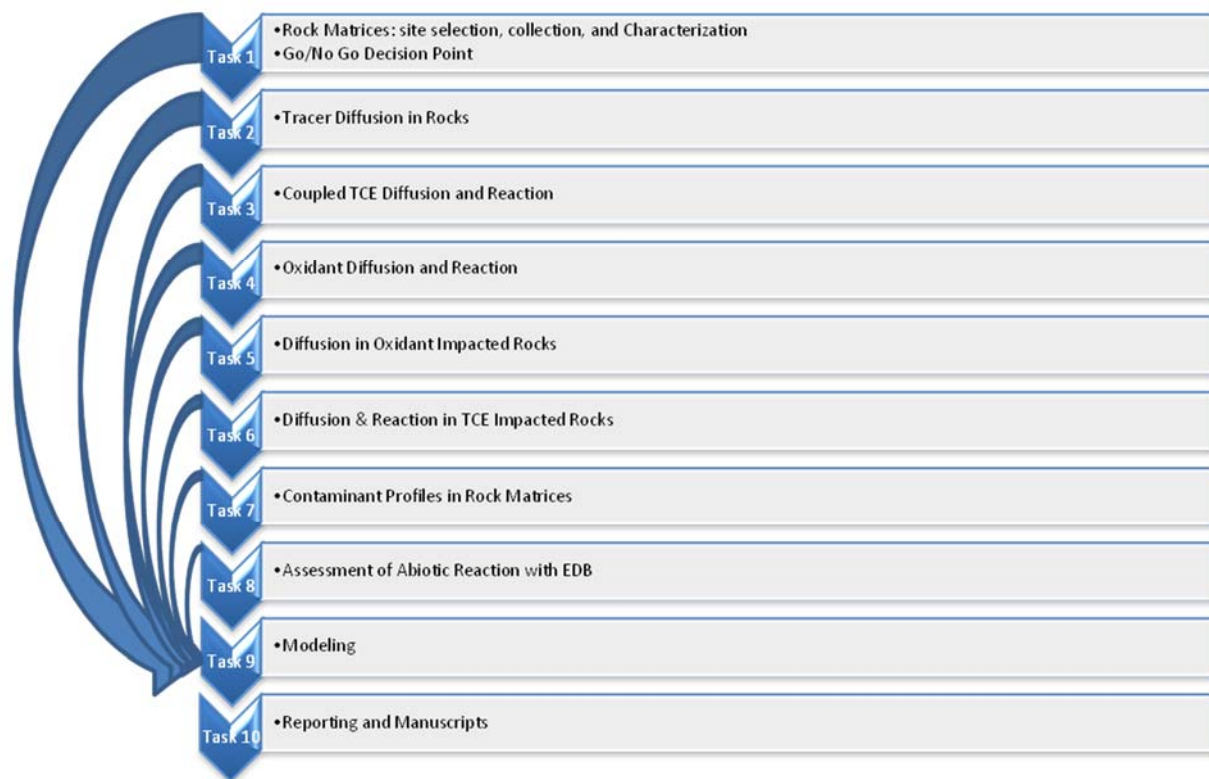


Figure 3.1. Experimental approach, segregated into Tasks.

3.2 Site Geology and Core Collection

3.2.1 Site Selection

The Naval Air Warfare Center (NAWC) in Trenton, New Jersey was selected for the collection of rock cores for this project. The geology and hydrogeology of this site have been extremely well-characterized by the U.S. Geological Survey (USGS) and others. Because of its varied geology, the NAWC site offered the opportunity to collect many different rock types, including mudstones, red sandstones, and white sandstones. Initial rock core collection was performed at locations outside the TCE groundwater plume, and a subsequent rock core collection (to attain rock that had been impacted long-term by TCE) was performed at a location within the TCE groundwater plume.

The NAWC site is underlain by 0 to 10 feet of unconsolidated sediments. Dipping layers of fractured mudstone, siltstone, shale and sandstone of the Lockatong and Stockton Formations are beneath the unconsolidated sediments (USGS, 2003). The units strike N. 60° E. to N. 70° E. and dip 15° to 20° NW. Each bedding unit consists of several water-bearing zones, alternating with confining zones. Water is transmitted primarily through fractures and joints in the rock. A fault

cuts through the bedding units at or near the contact between the Stockton and Lockatong Formations. The fault strikes about N. 70°E and dips about 40° SE (USGS, 2003).

The rock core collection for Tasks 1-5, and 8 (Figure 3.1) was performed from within areas at NAWC that were *not* within the contaminant plume. This was the first phase of core collection. The locations for collection of these cores are shown in Figure 3.2.2. Core locations within the Lockatong formation consisted of sandstones, dark gray mudstones, and light gray mudstones. Core locations within the Stockton formation consisted of red and white sandstones.

The second phase of core collection was intended for Tasks 6 and 7 (laboratory studies focused on TCE-impacted rocks). For these tasks, bedrock cores were collected at a location at NAWC that was within the TCE plume. Using available site information from the USGS as a guide, a single borehole location (90BR) was selected for rock core within a historically contaminated TCE plume, and adjacent to TCE-contaminated conductive fractures. Rock at this location consisted primarily of light gray and dark gray mudstones. Additional rock cores were collected for Task 7 at Edwards AFB (Site 37 source area, which is part of the South Air Force Research Laboratory, California), and Calf Pasture Point (Naval Construction Battalion Center, Rhode Island).

3.2.2 Core Collection – Phase 1 (outside of the TCE Plume)

The objective of rock core collection for this initial phase was to attain minimally disturbed rocks collected from the saturated zone for both the rock the characterization (Task 1) and bench scale testing (Tasks 2 through 7). Rock matrix diffusion experiments typically have been performed using small (<5 cm dia.) rock cores (Siitari-Kauppi et al., 1997; Boving and Grathwohl, 2001). A similar approach was used for this project, but precautions were made during sample collection to limit and identify potential geochemical (i.e., oxidation due to air exposure) and physical (i.e., microfractures) disturbances to the rock cores during sample collection.

The first phase of drilling activities (i.e., outside of the TCE-impacted zone) at NAWC was performed between November 16, 2009 and December 7, 2009, with locations shown in Figure 3.2.2. The second phase of drilling activities (i.e., within the TCE-impacted zone) at NAWC occurred between March 20, 2013 and March 25, 2013, with the location shown in Figure 3.2.3. For the first phase of core collection, a 10 ¼-inch nominal borehole was advanced through overburden and weathered bedrock using 6 ¼-inch inner diameter (ID) hollow stem augers (HSAs). The HSAs were left in place as temporary casing. A 5¾-inch rotary bit and recirculation of drilling fluids (potable water) was used to remove soil and weathered bedrock remaining within the augers. The rotary bit was then advanced until competent bedrock was observed. Rock cores were collected using a triple tube wireline PQ Core Barrel system. This system created a

nominal 4.82-inch diameter core hole, and allowed for the collection of minimally-disturbed 3.27-inch diameter rock core sections. Rock core sections were collected in up to 5-foot lengths. Rather than extruding the rock core from the inner tube (as with traditional dual tube methods), the triple tube system contains a third tube made of stainless steel that is split lengthwise and nested inside the second tube. When the rock core was retrieved from the subsurface, the split tube was extruded from the second tube. The upper half of the split tube was carefully lifted off, revealing the core in a virtually undisturbed condition for inspection and transfer.

In addition to collecting sections of relatively unfractured bedrock, cores were collected across prominent (i.e., water-bearing) fracture intersections to facilitate evaluation of natural redox fronts on diffusion coefficients (as part of the planned laboratory experiments). Cores were collected using a moderate drilling speed, with moderate, steady down-pressure and sufficient circulation to cool the drilling bit. 74 feet and 105 feet of rock core were collected from the Lockatong and Stockton Formations, respectively during the initial coring.

Artificial oxidation of reduced minerals in the rock caused by exposure to air during the coring process could potentially limit our ability to evaluate oxidant or TCE reactions with reduced iron species. Tracer studies performed during previous core collections have demonstrated that introduction of aerated fluids during core collection are not expected to impact the interior of the rock matrix (McKinley and Colwell, 1996; Smith et al., 2000; Dong et al., unpublished data). These results are consistent with observations of redox fronts emanating from fractures in ferrous-iron cores, which persist with no observable changes over weeks despite being collected while exposed to ambient air. Nevertheless, to limit potential air exposure during drilling, we used anaerobic (nitrogen sparged) water as the drilling fluid during core collection. Re-circulated drilling fluids used during rock coring also were sparged with argon within the drilling tub to maintain anaerobic conditions. This was accomplished by covering the drilling tub (which served as a reservoir for the re-circulating drilling fluids) with plastic, and sparging argon gas through perforated garden hose (soaker hose) throughout the drilling tub. Dissolved oxygen (DO) concentrations in the tub were continuously monitored, and argon sparging rates were adjusted as needed to maintain DO concentrations below ~1.0 mg/L. The aqueous drilling fluid also contained a bromide tracer. The measured bromide concentration in the re-circulated drilling fluids was approximately 350 mg/L. CB&I sampled for background concentrations of bromide in the vicinity of each of the drilling locations (at existing wells) prior to coring to ensure that significant concentrations of bromide were not present as background.

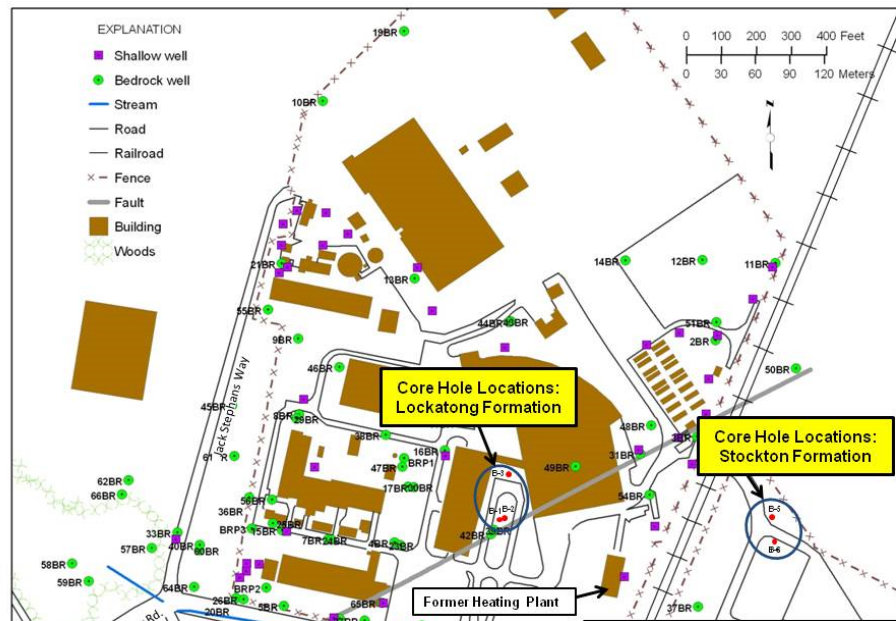


Figure 3.2.2. The Naval Air Warfare Center (NAWC) in Trenton, NJ site selection outside the contamination zone.

Upon retrieval, the bedrock core sections were placed on sections of 4-inch diameter, schedule 40 PVC pipe halves to protect the mechanical integrity of the collected cores during transportation and storage. The cores and PVC pipe halves were placed in argon purged semi-transparent bags for visual inspection. Argon gas was continually delivered into the bags (creating positive pressure) during this process. Some core sections were photographed immediately prior to being placed in the bags. The collected cores (along with the PVC halves and semitransparent bags) were then placed into argon-purged barrier foil bags (VF42 Polyester/Foil/Linear Low Density Polyethylene) (LPS Industries, Inc., Moonachie, NJ) to limit gas permeation (Supplemental Figure 3.2.2). The foil bags, after argon purging, were sealed immediately with a portable heat sealer (model Futura B), thus providing long-term anaerobic conditions for the collected samples. The successful use of barrier materials for anaerobic transportation and storage of core samples has been previously performed and documented (Cragg et al., 1992). According to the property data provided by the manufacturer, the selected material (VF42 Polyester/Foil/Linear Low Density Polyethylene) demonstrates exceptionally low oxygen and moisture vapor transmission rates, which are below $0.0006 \text{ cm}^3/\text{m}^2/\text{day}$ and $0.0006 \text{ g}/\text{m}^2/\text{day}$, respectively. All core samples were hand delivered the day they were collected to CB&I's treatability study laboratory in Lawrenceville, NJ (located approximately 10 miles from the NAWC site).

To verify that the rock cores were minimally disturbed sub-samples of rock core were collected to assess the potential extent of drilling fluid migration into the rock matrices. Sub-samples collected for this analysis were rinsed with water after core collection to remove bromide on the external core surface (if not rinsed, this bromide would slowly diffuse into the rock matrix, thereby skewing our results). Because of this rinsing, sub-samples collected for bromide tracer analysis were not kept anaerobic.

To determine the extent of potential migration of drilling fluids into the rock matrices of these subsamples, rocks (15 to 50 cm³) were crushed and extracted with deionized water for three days. The total mass of bromide in the rock matrices of these sub-samples were estimated, thereby providing an assessment of the exposure of the rock matrix to the drilling fluids, and to any artificial exposure to dissolved oxygen

Sub-samples of rock core also were collected to ensure that the coring process did not introduce any microfractures within the rock matrices. Our approach was to use scanning electron microscopy (SEM) to examine small sections of rock core along a naturally occurring fracture face. SEM images taken along the edges (where micro-fracturing due to the coring is most likely to have occurred) were compared to those in the center of the core. A total of 4 core sections (2 sandstones and 2 mudstones) were imaged and evaluated.

The collected core sub-samples were too large to place into the SEM sample holder directly. Therefore, a positive replica technique was used with Reprosil vinyl polysiloxane impression material. This material is degassed with hydrophilic surface characteristics and excellent dimensional accuracy and detail (<10 microns). Reprosil is a 1:1 mixture of base to catalyst, which sets in ~10 minutes. The repositil was spread onto the surface of the core evenly and allowed to set. The mold was then removed from the core surface. Once the mold was created, well-mixed Spurr's resin was poured into the mold to create a positive replica, and the resin was allowed to harden overnight at 70 C, gold-coated, and viewed in SEM.

3.2.3 Core Collection – Phase 2 (within the TCE Plume)

The objective for this second phase of rock core collection was to verify that abiotic dechlorination reactions capable of significantly reducing MNA time frames are actually occurring in the field within bedrock matrices. Our experiments involved measuring the rates of TCE diffusion and reaction that are occurring in the bedrock matrices at TCE-impacted DoD sites.

Bedrock cores and water samples were collected for this phase of testing from within the known TCE plume within the Lockatong formation (Lacombe and Burton, 2010) at the NAWC in

Trenton, New Jersey (See Figure 3.2.3). Rocks from the Lockatong portion of the NAWC site consist of light to dark gray mudstones, with dipping layers. Each bedding unit consists of several water-bearing zones, alternating with confining zones. Rock sections directly adjacent to the water bearing fractures through which TCE is migrating were chosen.



Figure 3.2.3 Phase 2 rock core collection at the former Naval Air Warfare Center (NAWC) in Trenton, New Jersey

Rock coring and discrete groundwater sampling activities at a single borehole (90BR) at the NAWC Site were performed between March 18 and March 25, 2013. The borehole was hand dug to 5 feet below ground surface (bgs) to clear for any potential underground utilities. The borehole was advanced through the overburden and weathered bedrock using mud rotary drilling methods and a 3 7/8-inch drill bit. Competent bedrock was encountered at 24 feet bgs, and 3-inch

inner diameter temporary casing was installed to 25 feet bgs, one foot into competent rock. A wireline system with NQ core barrel was used to collect 1 7/8-inch (47.6 mm) rock core from 24 to 85 feet bgs.

Rock core was collected and retrieved in 5-foot runs and placed temporarily on individual PVC liners (3" PVC pipe cut in half). The cores were handled carefully to minimal disturbance to the sections of rock core. The length of the core was screened with a photoionization detector (PID), and visual observations of the rock were made to identify potential water-bearing fractures/zones. Rock core sections were collected for laboratory analysis from both sides of what appeared to be three water-bearing fractures. Upon retrieval, the selected rock core sections (along with the PVC liners) were placed and sealed in nitrogen-purged clear bags for visual inspection and core logging. The collected cores were then placed into nitrogen-purged barrier bags (as described in Section 3.2.2) and sealed immediately with a portable heat sealer, thus providing anaerobic conditions for the collected samples. Samples were immediately hand delivered the day they were collected to CB&I's treatability study laboratory in Lawrenceville, NJ (approximately 10 miles from the NAWC site).

3.3 Groundwater Characterization

Groundwater samples during the initial field activities in 2009 were collected from both the Stockton and Lockatong formations in the vicinity of where the bedrock cores were collected to provide a geochemical characterization of the site groundwater. Extensive analytical characterization of both groundwater samples was performed including pH, alkalinity, and concentrations of major anions and cations. This information was used to develop a recipe for preparing synthetic groundwater (SGW) that was used in the laboratory experiments

During the second phase of coring activities (March 2013) three discrete groundwater samples were collected from intervals 45 to 50 feet bgs, 50 to 55 feet bgs, and 80 to 85 feet bgs. These water bearing zones were visually determined by the CB&I geologist as the borehole was advanced. Rock coring was halted once a water bearing zone is identified. A packer with a sampling pump below it was lowered to the 5 foot discrete sampling interval. The packer was inflated to isolate the sampling interval from the borehole above. Each of the discrete intervals was purged between approximately 35 and 90 minutes at a low flow rate (~200-800 mL per minute), while field parameter measurements (pH, DO, ORP, specific conductivity) were collected within a flow-through cell using a YSI 600XL multi-parameter meter. Purging continued until the field parameters stabilized. Samples were collected at each of the discrete intervals for volatile organic compounds, reduced gases, carbon isotopes, and microbial analysis.

3.4 Rock Characterization

Rock cores collected during the initial phase were collected from two geologic formations (Stockton and Lockatong Formations), each providing several types of mudstone and/or sandstone. Prior to any laboratory testing to assess diffusion and reaction within the rock matrix, the cores were examined with regard to the rock porosity, mineralogy, bedding plane orientation, presence of water-bearing fractures, and total organic carbon (TOC) content.

3.4.1 Porosity

The total water accessible porosity for the various rock types was determined by measuring the water uptake within the rock. Small slices of rock (50 to 150 cm³) were oven dried at 105° C for three days, and subsequently immersed in synthetic groundwater (SGW) (see Table 4.2.1 for groundwater composition) so that the top of the rock face remained above water to allow for escape of air during imbibition. Wet rock samples were weighed by removing the rock from the water bath and placing it immediately upon an analytical balance. The water uptake experiment continued until moisture equilibrium was established. The effective porosity was estimated by calculating the volume of water taken up by the rock divided by the volume of the rock.

We performed a water uptake test to verify that the surface of the rock was not altered by the cutting procedures (i.e., no decrease in rock permeability on the surface due to cutting). Water uptake into two similarly sized rocks was measured, where one rock had a saw-cut face, and the other rock face had been naturally fractured. The rate of water uptake into the rocks were nearly identical (within 20%), indicating that saw-cutting the rock did not substantially alter the surface permeability of the rock, and would not impact our measurement of effective diffusivity through the rock.

Total porosity also was estimated by the use of mercury (Hg) porosimetry. The technique involves the intrusion of mercury at high pressure into a rock through the use of a mercury porosimeter. The pore size can be determined based on the external pressure needed to force the mercury into a pore against the opposing force of the mercury's surface tension.

Several researchers also have employed the use of emission Scanning Electron Microscopy (SEM) with image analysis to provide an estimate of the porosity based on 2-dimensional imaging (Ziel et al., 2008; Bruckschen et al., 2005; Ruzyla, 1986; Pye, 1984). These techniques use the fraction of porous area measured in 2-dimensions to estimate the 3-dimensional porosity (Ziel et al, 2008). Thus, SEM-measured porosity is actually a measure of the effective pore cross-sectional area in the orientation (e.g., normal or parallel to bedding) of the image. We employed the use of a Zeiss Supra 35 VP Field Emission Scanning Electron Microscopy to

estimate an “apparent porosity” both normal and parallel to bedding. Although porosity is a scalar quantity that is independent of orientation, our use of “apparent porosity” incorporates the effects of pore cross-sectional area associated with bedding orientation. SEM images collected from thin sections cut normal and parallel to bedding were analyzed with the Image J software (NIH) to determine apparent porosity (based on the pore cross-sectional area) in each orientation. The whole range of brightness of the images was divided into multiple intervals, and the lowest level was considered porosity. This brightness setting was periodically checked against standards of known porosity. The resulting porosity was also manually checked against water uptake measurements.

3.4.2 Mineralogy

Mineralogy of each rock type was assessed using X-ray diffraction (XRD). XRD was performed to identify the mineralogy of the rock cores by using a Scintag X1 powder diffractometer system using CuK α radiation with a variable divergent slit and a solid-state detector. For the XRD analysis, rock cores were ground into powder, and tightly packed into the well of low-background quartz XRD slides (GemDugout, Inc., Pittsburgh, PA, USA). To facilitate qualitative comparisons among the samples, a similar amount of solid powder from each sample was packed into a rectangular volume of the same dimensions. The routine power was 1400 W (40 kV, 35 mA). Samples were scanned from 2 to 70 degrees in 0.02 two-theta steps with a count time of 5 seconds per step. Search-match software was combined with manual check to conduct mineral identification.

Rocks were further characterized for ferrous and total iron contents. This was determined by using the 1,10-phenanthroline method (Amonette and Templeton, 1998) and direct current plasma emission spectrometry, respectively. To determine the amount of Fe(II) that was readily available to react with TCE, the total Fe(II) (mmol g⁻¹) was multiplied by the fraction of Fe(II) accessible to the rock porosity. To estimate this fraction of Fe(II) available to the rock porosity, 1) elemental maps of total Fe were obtained with SEM electron dispersive spectroscopy (unit: signal intensity or brightness); and 2) assuming that the total Fe distribution was proportional to the ferrous iron distribution (i.e., a uniform distribution of ferrous iron throughout the total Fe elemental map), the elemental maps of total Fe were converted to elemental maps of Fe(II) by multiplying the total Fe signal intensity by the chemically determined ratio of Fe(II)/total Fe. The fraction of Fe(II) available to the rock porosity was then quantified by overlaying the elemental Fe(II) maps over porosity distribution maps. The unit of the summed Fe(II) available for TCE reaction was converted from signal intensity to mmol g⁻¹ assuming that total Fe(II) signal intensity (available + unavailable to the rock porosity) is equal to the chemically determined Fe(II) concentration (mmol g⁻¹).

3.4.3 Total Organic Carbon

Naturally present reactive reductants, such as total organic carbon (TOC), can impact the migration of chemical oxidants into the rock matrices. TOC also can cause sorption of the TCE in the rock matrices. A measurement of the TOC for each rock matrices was taken. TOC was measured by crushing 1g of rock into a fine powder. A slurry was created with ultra-pure water, and the pH was decreased to less than 2 with 85% phosphoric acid to remove inorganic carbon. Samples were then dried at 105 degrees C overnight. The samples are run on an Apollo 9000 TOC analyzer with the 183 Boat Sampling Module according to EPA Method 9060.

3.4.4 Rock Oxidant Demand

To facilitate evaluation of oxidant reaction and diffusion through the rock matrices, select rocks were evaluated with respect to their natural oxidant demand. Oxidant demand testing was performed using both permanganate and persulfate. Testing on four primary rock types from the Naval Air Warfare Center site (tan sandstone, red sandstone, dark gray mudstone, and light gray mudstone) was selected. These rocks were chosen because they were to be used in the oxidant diffusion and reaction experiments described in Section 3.5.6. For each rock type, 10 g of crushed rock (approx. 1 cm) were placed in a 60 mL amber glass serum bottle, and with 2000 mg/L permanganate or 2000 mg/L persulfate. All samples were prepared in duplicate with two control samples containing only synthetic groundwater, and either persulfate or permanganate. The time course decrease of aqueous permanganate concentration was measured using a Mattson Genesis II spectrophotometer at a wavelength of 526 nm. Measurements were taken at time zero and once a week thereafter. Once the aqueous permanganate concentration stabilized (about 1 month), oxidant demand was calculated in terms of the mass of permanganate reduced per kilogram of crushed rock. Persulfate concentrations were measured by adding an excess of potassium iodide to the collected samples, and then titrating with sodium thiosulfate.

We repeated this initial oxidant demand testing using powdered rock to see if the increased surface area and smaller particle size caused an increase in the measured oxidant demand. Our speculation was that use of the powdered provided a more representative bulk oxidant demand than the crush (cm-scale) rock when considering oxidant diffusion into the rock matrix. The same four rock types were tested. For each rock type, we placed 2 g of the powdered rock in a 25mL amber glass serum bottle, and with 2000 ppm permanganate or 2000 ppm persulfate. All samples were prepared in duplicate. The permanganate concentrations were measured using a Genesis 2 spectrophotometer at a wavelength of 526 nm, and persulfate concentrations were measured via titration.

3.5 Diffusion and Reaction Experiments – Rock Collected *Outside* the TCE Plume

The purpose for these experiments was to attain insight into the diffusional and reactive processes occurring within the rock matrix, and to attain improved insight into how rock properties (mineral bedding, ferrous iron content, porosity, etc.) potentially impact these processes. We note that all testing described in Section 3.5 was performed using rock collected during the first phase of core collection, and therefore had not been historically exposed to TCE.

3.5.1 Batch Sorption and Reaction Testing

In preparation for the diffusion cell testing, a series of batch tests was conducted to assess sorption of model solutes, thereby allowing us to estimate diffusional timeframes prior to the diffusion experiments. Both TCE and iodide batch experiments were conducted for five rock types (selected based on the core collection described in Section 3.2.2 and 3.2.3): red sandstone, dark gray mudstone, light gray mudstone, a pyrite seam (within the mudstone), and a weathered mudstone.

Batch iodide experiments were prepared in order to determine the extent of sorption or reaction of iodide with the various rock types, thereby serving to confirm that iodide can be considered a conservative tracer for the diffusion experiments. We note that, because diffusion coefficient were determined during the steady-state portion of the diffusive flux curve (described in subsequent Section 3.9 and Figure 4.4.2.1), sorption of the iodide did not exclude its use for estimating the effective diffusion coefficients through the rock.

Batch experiments were performed in triplicate in 125-ml serum bottles that were sealed with Teflon-lined stoppers and aluminum crimp seals. Red sandstone and dark grey and light grey mudstones were crushed into small pieces (< 20mm), weighed, and placed into the bottles (separate bottles were prepared for each rock type). Approximately 30 to 40 g of each rock were used. Bottles were next amended with SGW (60 or 80 mLs). The bottles were amended with iodide (I⁻) for a final concentration of 100 mg/L (as KI). The bottles were incubated on an orbital shaker at room temperature, and the aqueous phase was periodically analyzed for iodide. A set of controls (with no rock present) accompanied each batch experiment.

Batch experiments with TCE were performed to evaluate the sorption and reaction of TCE with crushed rock. In the TCE batch experiments, 10 g of crushed rock (< 20mm) were combined with 10 ml of SGW in 25-ml serum bottles. Due to the limited amount of pyrite available for the experiment, only about 2 g of crushed pyrite and 10 ml of SGW were used in these batch tests. The bottles were sealed with Teflon-lined stoppers and aluminum crimp seals. The bottles then were spiked with 0.5 ml of a saturated TCE solution using a gas-tight glass syringe. All batch

experiments with TCE were performed in triplicate and conducted under anaerobic conditions (with the exception of brief exposure to air during rock crushing procedure). The bottles were incubated on an orbital shaker at room temperature. Headspace samples were periodically analyzed for TCE (as well as for lesser chlorinated ethenes and reduced gases) using a Varian 3900 GC-FID (Palo Alto, CA).

In addition, preliminary testing was performed using different types of sealants that would potentially be used in the construction of the diffusion cell. This testing was performed to confirm that the TCE was inert (i.e., no sorption or reaction) with respect to the sealant used. J B Kwik epoxy adhesive (J-B Weld, Sulphur Springs, TX), and Devcon plastic steel epoxy (ITW Devcon, Danvers, MA) were each tested. Each sealant was weighed (1-2g of each) and dried overnight. The dried pieces were then placed in a 60mL glass serum vial containing 100 mg/L TCE, and left on a shaker at room temperature. Aqueous samples were collected at 24 hours and 120 hours. *Sorption of TCE to both epoxies was found to be negligible when compared to sorption and reaction of TCE with crushed rock.*

3.5.2 Preliminary Diffusion and Reaction Experiments using Rectangular “Rods” of Rock

Experiments were performed to provide a preliminary assessment of the coupled diffusion and reaction of TCE using the dark gray and light gray mudstones. For these experiments, the rocks were not crushed as described in the previous section, but rather were cut in into small rectangular rods. The rods varied in size and were typically about 4-6 cm long and about 1 cm wide and deep. The sides of the rods were coated with Devcon plastic steel epoxy (ITW Devcon, Danvers, MA), leaving only one exposed face of the rod that was available for diffusion and reaction. The available diffusion area ranged from 4 to 6 cm² for each rod. Once cut and after allowing time for the epoxy to dry, all rock samples were placed in an anaerobic chamber (>99% nitrogen) with a custom airlock (Coy Laboratory Products, Inc., Grass Lake, MI). In the anaerobic chamber the rods were placed in 40-ml glass vials and amended with 25 ml of TCE and iodide anaerobic SGW solution in a way that the rods were completely submerged in the liquid phase. The solution contained approximately 1000 mg/L of I⁻ (as KI) and 20 mg/L of TCE. Anaerobic SGW was prepared by sparging 1 liter of water with nitrogen for 1 hour, and then storing inside the anaerobic chamber. The vials were capped with a Mininert vial valve (VICI Precision Sampling, Baton Rouge, LA), which provided a gas-tight seal and sampling access. The concentrations of TCE and iodide were monitored periodically over a two month period.

3.5.3 Diffusion Cell Construction and Rock Disc Preparation

Diffusion cell experiments were performed to measure the coupled diffusion and reaction of TCE and iodide through selected discs of rock. The conceptual design of the diffusion cell was based on the design of Boving and Grathwohl (2001), but some prominent application-specific differences were added to the design. The key requirements for the cell design included 1) the use of materials and components chemically inert and resistant to TCE and oxidants and 2) the gas-tight construction, crucial for the work with volatile compounds (TCE).

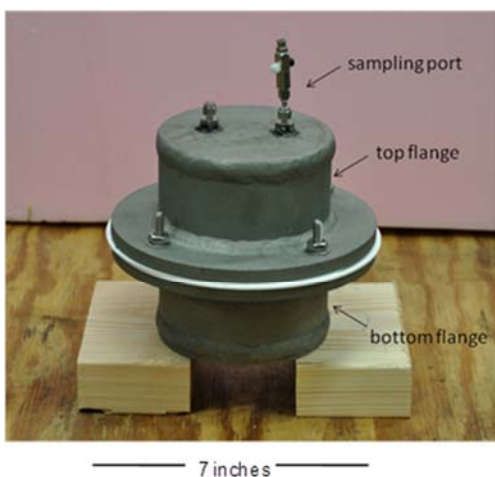
The diffusion cell was constructed to hold thinly-cut (0.5 to 1.5 cm) slices of rock core, oriented either parallel or normal to bedding, so that tracer diffusion across the rock slice could be measured. The body of the designed cell (Figure 3.5.3) consisted of the two stainless steel custom-made flanges (Morrill Industries, Inc., Escalon, CA). The volume of each half was approximately 0.5L, where one half served as the source reservoir and the other half as the sink reservoir for the diffusion experiment. The top of each flange contained two sampling ports. The sampling ports, which ensured the gas-tight conditions during experimental and sampling procedures, consisted of Swagelock® fittings (Penn Fluid System Technologies, Huntingdon Valley, PA) and valves (Supelco, Milwaukee, WI). Only inert materials (e.g., stainless steel, PTFE sealant, GORE™ Joint Sealant, W. L. Gore & Associates, Elkton, MD) were used for sampling port construction. To ensure the seal between the flanges, a double gasket was placed between the top and bottom flange.

After the cell was constructed, pressure-testing was performed to ensure that the cell was gas tight. To further validate test cell design and ensure there was no substantial loss of TCE, a TCE leak test was conducted. 1 L of a 50 mg/L TCE solution was delivered to the cell via a sampling port using a 100-mL gas-tight glass syringe, and TCE concentrations were measured as a function of time over several weeks. Samples were collected by extracting 1-mL aqueous samples from the sampling port, placing the sample into a 3-mL vial capped with a Teflon septum, and then analyzing the sample headspace (after equilibration). Several gasket materials including PTFE gaskets and PTFE gasket envelopes were leak tested. Viton® gaskets and PTFE sealant (GORE™ Joint Sealant, W. L. Gore & Associates, Elkton, MD) demonstrated a satisfactory seal and were selected as the seal materials for the cell flanges.

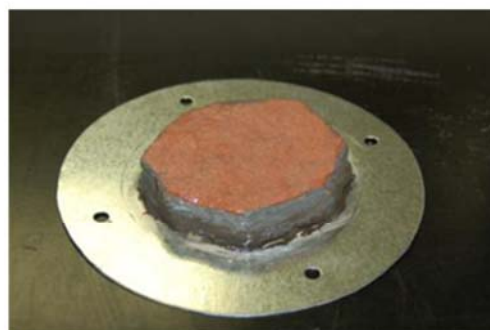
For the rock diffusion and reaction experiments, the investigated rock was pre-cut. Rock sections were cut from the rock cores using a diamond blade electric saw. Rock sections were typically 5 to 10 cm in diameter and 0.5 to 2 cm thick. After cutting the rock, each section was mounted on a thin base of aluminum sheeting (0.2 cm diameter) (Figure 3.5.3) using J B Kwik epoxy adhesive (J-B Weld, Sulphur Springs, TX). A rectangular opening was cut in the aluminum so that the face of the rock section was not covered by the aluminum. The aluminum base was cut so that it would fit between the flanges of the diffusion cell. To ensure that the diffusion of TCE

and iodide occurred solely across the rock (in the direction from the source reservoir to the sink reservoir of the cell), the sides of the rock disc were sealed with Devcon plastic steel epoxy (ITW Devcon, Danvers, MA). Before inserting the aluminum sheet and rock between the flanges of the diffusion cell, the rock was stored inside an anaerobic chamber, and saturated with anaerobic SGW (using the same technique as we used for measuring the water uptake porosity). The Viton® gaskets were used to obtain a seal between the flanges and aluminum sheet. Bolts (1/4 in.) were used to fasten and secure the flanges and aluminum sheet-mounted rock. The sink and the source reservoirs were filled with the corresponding starting solutions. The sink reservoir was filled first, then source side was filled. The volume of the sink reservoir was approximately 520 ml. The attached rock was positioned on the source side. Mounting of the rock inside the diffusion cell was performed outside of the anaerobic chamber for ease of manipulation, but all other tasks such as applying epoxy adhesive, and filling the diffusion cell with TCE/Iodide amended anaerobic SGW were performed inside the anaerobic chamber to limit exposure of the rock to air.

NOTE: As discussed in the results, limited (hours to days) exposure of the rock to air did not have any measureable impact on the abiotic dechlorination reactions that were monitored in the coupled diffusion/reaction experiments described in Section 3.5.5. Regardless, efforts were made throughout this project to limit exposure of the rocks used in the coupled TCE diffusion/reaction experiments to air to the extent practicable.



Sample for TCE and daughter products



Mounted Rock Disc
(0.5 to 2 cm thick)

Figure 3.5.3 Diffusion cell used to measure the effective diffusion coefficient through the cut rock sections

3.5.4 Bedding Plane Orientation Experiments – Iodide Diffusion

To investigate the effect of bedding plane orientation on the diffusion through the rock matrices, experiments were performed to measure diffusion in orientations parallel and perpendicular to mineral bedding. Three different rock types with visually apparent mineral bedding were collected: a red sandstone (Stockton Formation), a tan sandstone (Stockton Formation), and a dark gray mudstone (Lockatong Formation). In addition, a sandstone block (Arizona Buff) obtained from a commercial quarry, which also contained clearly visible mineral bedding, was used for the bedding plane iodide diffusion experiments.

To attain rock discs with the proper bedding orientation, collected rock cores were carefully examined to determine the natural bedding orientation. Rock discs were then saw cut to obtain rock discs, arranged in the appropriate bedding orientation, that could be sealed within the diffusion cell. To facilitate handling, these experiments were not performed under anaerobic conditions (since only diffusion of an inert tracer was being measured, and no TCE was present, exposure to air was not considered a factor).

In a typical diffusion experiment, the source reservoir contained 0.0158 M KI (equivalent to ~ 2000 mg/L I^-) dissolved in SGW, and the sink reservoir contained an iso-osmotic solution of 0.0158 M KNO_3 in SGW. The samples from the sink and source reservoirs were periodically collected and analyzed for iodide via ion chromatography (Dionex DX-120, Sunnyvale, CA). Experiments were performed at least in duplicate for each rock type used. Before reusing rocks for replicate experiments, the rock sections were placed in a water bath (periodically refreshed) until the back-diffusion of iodide from the rock became negligible, indicating that >99% of the iodide had been removed.

3.5.5 Diffusion Cell Experiments – Coupled TCE Diffusion and Reaction

The objectives of this set of experiments was to quantify the abiotic dechlorination reaction of TCE in rock matrices (based on generation of daughter products), and to attain insight into the rock properties that controlled or impacted these dechlorination reactions in intact sections of rock. In particular, these rock properties or characteristics include rock type, location in regard to the fracture interface (e.g., as a function of the distance from the water-bearing fracture), presence of iron minerals (e.g., pyrite), and the oxidation state of the ferrous minerals.

The methods for performing the coupled TCE diffusion and reaction experiments through the rock discs generally followed the same disc and cell assembly procedures as described in Sections 3.5.3 and 3.5.4. The experiments were conducted inside an anaerobic chamber to limit air exposure to the rocks and TCE solution. The source reservoir within the diffusion cell

contained 0.0158 M KI dissolved in anaerobic SGW with approximately 200 mg/L of TCE, and the sink reservoir contained an iso-osmotic solution of 0.0158 M KNO₃ in anaerobic SGW. TCE diffusion reaction experiments were also amended on both the source and the sink side with mercuric chloride (HgCl₂) to a concentration of 300 mg/L to limit any potential biological activity; experiments also were performed without amending with mercuric chloride to assess the relative importance of any biotic processes and/or to assess any impacts of the mercuric chloride on the ferrous mineral-enhanced dechlorination reactions. Experiments were performed at room temperature (approximately 20 degrees C). Typical experiments lasted 30 to 80 days.

For each experiment, aqueous samples (1 mL volume) from the sink and source reservoirs were periodically collected from inside the anaerobic chamber into 2mL amber serum vials crimp sealed with Teflon lined septa. Headspace samples were analyzed from these 2mL vials on a Varian 3900 GC-FID (Palo Alto, CA). Using Henry's Law, the concentrations of TCE and reduced gas daughter products in the cell were determined. The total aqueous volume removed from the diffusion cell during for sampling during each experiment was less than 10% of the total water volume, and the tracer concentration on the sink side of the chamber remained below 2% of the source side tracer concentration. While the cells were prepared with zero headspace, the partitioning of TCE and daughter product mass into a relatively small amount of headspace generated via aqueous sampling was accounted for via Henry's Law. Similar to the iodide diffusion experiments described in Section 3.5.4, rock sections were placed in a water bath within the anaerobic chamber (periodically refreshed) until the back-diffusion of iodide and TCE from the rock became negligible and the rocks were re-used in replicate experiments.

Additional experiments were performed with 100mg/L Fe²⁺ (as FeSO₄·7H₂O) to determine if the presence of dissolved ferrous iron would enhance the observed abiotic reactivity. Such conditions (i.e., enhancement of dissolved iron in groundwater) might exist during application of *in situ* bioremediation, and therefore the potential impact of this dissolved iron on abiotic reaction in the rock matrix was of interest.

Several different rock types, which all were present at the NAWC site, were collected for the diffusion and reaction experiments. Rocks used consisted of red sandstone (Stockton Formation), tan sandstone (Stockton Formation), dark gray mudstone (Lockatong Formation), light gray mudstone (Lockatong Formation), pyrite rich mudstone (Lockatong Formation), and a pyrite seam (Lockatong Formation).

TCE and reduced gas (ethane, ethene, and acetylene) concentrations were determined via headspace analysis using a Varian 3900 gas chromatograph equipped with a Flame Ionization Detector (FID) and Aluminum RT column. Aqueous concentrations were determined by applying Henry's Law. Anions were analyzed via ion chromatography (Dionex DX-120, Sunnyvale, CA).

In addition, Hach test kit HS-C was used to measure hydrogen sulfide in both the sink and reservoir sides for two of the experiments: one using the pyrite rich mudstone, and one using the light gray mudstone. Hydrogen sulfide was measured because dissolved sulfide can be oxidized releasing Fe^{2+} which can then be oxidized to Fe^{3+} , in turn attacking pyrite regenerating Fe^{2+} . For each of these experiments, 3 measurements were collected on both the sink and source sides of the rock.

3.5.6 Oxidant Diffusion and Reaction

Chemical oxidants have been shown to oxidize naturally occurring ferrous minerals in rock matrices as a result of implementing *in situ* chemical oxidation for treatment of chlorinated solvent sources in bedrock fractures. Both sodium persulfate ($\text{Na}_2\text{S}_2\text{O}_8$) and potassium permanganate (KMnO_4) were used in these oxidant diffusion/reaction experiments to evaluate the diffusion and reactivity of chemical oxidants into the rock matrices.

During the preliminary testing it was found that the original epoxies used in the cell diffusion experiments, Devcon plastic steel epoxy and JB Kwik epoxy adhesive, were being consumed by both persulfate and permanganate oxidants. To find a compatible adhesive, oxidant demand was tested on different types of sealants that could be used in the construction of the diffusion cell (silicone, vinyl spackle, and glycol acetate enamel, Pelseal 2531, and Masterbond EP41S-1HT). These sealant tests were prepared in the same fashion as the rock oxidant demand tests with 10 g of epoxy in a 60 mL amber glass serum bottle, with 500 mg/L permanganate or 500 mg/L persulfate. The glycol acetate enamel and Masterbond EP41S-1HT epoxy were the only two that did not react with either oxidant. The enamel and the Masterbond epoxy were then subjected to TCE batch tests to assess potential TCE adsorption. Approximately 1-2g of each was weighed and dried overnight, then placed in a 60mL glass serum vial containing 100mg/L TCE, and left on a shaker at room temperature. Samples were taken at 24hours and 120hours. After the 24 hour time period, TCE concentrations exposed to the enamel decreased by 75%. TCE exposed to the Masterbond EP41S-1HT epoxy did not show any measureable decrease in concentration 120hours. Thus, the Masterbond EP41S-1HT epoxy was used to seal the rock to the diffusion apparatus for the oxidant diffusion/reaction experiments.

For the oxidant diffusion experiments, anaerobic conditions were not required. For ease of handling, a new cell design was employed that used a plastic cell (16.5 cm×6.3 cm×4.5 cm), shown in Figure 3.5.6, that was non-reactive with the oxidant (verified by control tests). A stainless steel frame was used to mount the rock and divide the cell into two halves. We initially attempted to use a galvanized metal (that was the same type used in the TCE diffusion

experiments) to keep the source and sink sides from mixing. However, the oxidant reacted strongly with that metal. Rock slices (~1.0 cm thick) were epoxied onto the stainless steel frame (covering the opening cut into the stainless steel frame to allow for diffusion across the rock) using Masterbond EP41S-1HT. The stainless steel divider, with the mounted rock, was then epoxied into the plastic dish. Roughly, 150 mL of 2000 mg/L potassium permanganate or 2000 mg/L sodium persulfate were prepared in synthetic groundwater and added to the source side of the reaction cell, and 150mL of an equivalent molarity of potassium nitrate to the sink side of the reaction cell to ensure ionic equivalency on each side of the reaction cell. Reaction cells were covered to prevent any photodegradation of the oxidants. Permanganate ion was monitored colorimetrically by removing an aliquot of the sink and reservoir chamber solution and measuring absorbance at 526 nanometers (nm) using a Genesis 2 spectrophotometer. Persulfate ion was measured in both the sink and source chambers using a titration with iodide (I^-). Experiments were performed for up to 8 weeks to monitor for breakthrough of the oxidants.

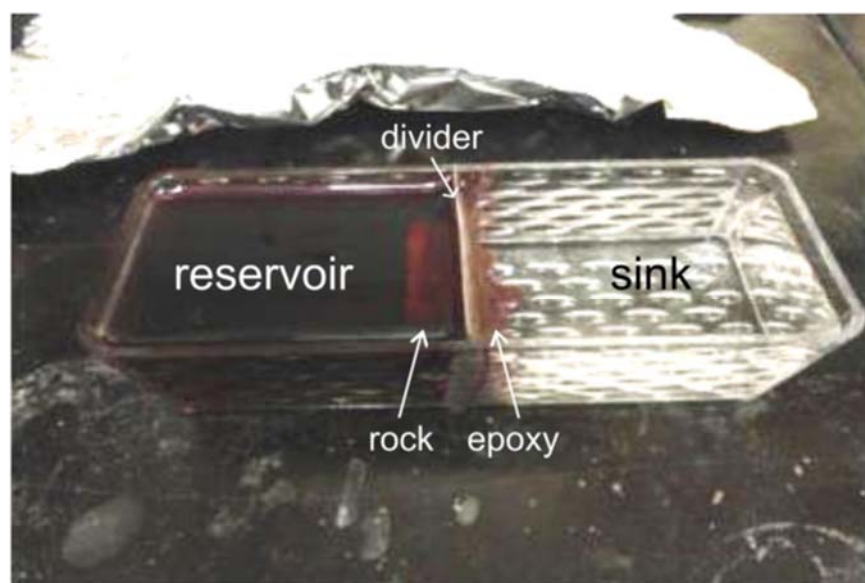


Figure 3.5.6. Plastic dish used for permanganate diffusion experiment. Rock slices were placed between permanganate solution (on the left) and synthetic groundwater (on the right). The pink color on the sink side is epoxy, not permanganate.

The reaction between permanganate and rock matrix is expected to result in formation of various manganese minerals (Li and Schwartz, 2004; Post, 1999). XRD was used to identify Mn precipitates on the rock surfaces that were exposed to permanganate solution using a Scintag X1 powder diffractometer system (Huang et al., 2011). Samples were X-ray scanned from 2 to 70 degrees two theta with Cu K-alpha radiation (40 kV, 35 mA), a 0.02 degree step size, and a count

time of 2 seconds per step. A combination of search-match software and manual check was used to identify mineral phases.

In the absence of any measureable breakthrough of oxidant into the sink half of the diffusion chamber, additional analytical techniques were employed to assess oxidant migration into the rock. To quantify the extent to which permanganate (KMnO_4) had penetrated into the rock matrix during the diffusion cell experiments and to determine the morphology of mineral precipitates formed on the rock, SEM was performed using a Zeiss Supra 35 VP Field Emission Scanning Electron Microscope with an EDX Genesis 2000 X-ray Energy Dispersive Spectrometer (EDS). SEM-EDS line scanning technique was used to measure the penetration distance of permanganate over the experimental duration (~2 months). All line scanning profiles were performed in triplicate. To observe the distribution of Mn minerals in relation to TOC and various other minerals, elemental maps were collected using a SEM-EDS standardized method, with an accelerating voltage of 15kV in a vacuum and a working distance of 8.5 mm.

3.5.7.-Diffusion through Oxidant Exposed Rocks

To determine the extent to which exposure to the oxidants impacted solute diffusion through the rocks (by modifying the porosity due to rock mineral alteration, and/or by formation of mineral precipitates such as manganese oxides on the rock surface), iodide tracer experiments were subsequently performed on the oxidant impacted rocks. Diffusion cells were prepared in a similar fashion as the permanganate and persulfate diffusion experiments (using the rock slices previously exposed to the oxidant), except that a 2000 ppm potassium iodide solution was added to the reservoir side instead of the oxidant. Iodide concentrations were determined using a Dionex dx-600 Ion Chromatograph. Iodide effective diffusion coefficients were calculated based on the flux of iodide through the rock, as described in our previous work (Schaefer et al., 2012).

3.6 Diffusion and Reaction Experiments – Rock Collected *Within* the TCE Plume

The purpose for these experiments was to evaluate the abiotic reaction of trichloroethene (TCE) in sedimentary rock matrices directly adjacent to hydraulically conductive fractures within a historically contaminated TCE bedrock aquifer. We note that all testing described in Section 3.6 was performed using rock collected during the second phase of core collection.

3.6.1-Rock Characterization

Rock core from the second core collection was collected from the Lockatong portion of the NAWC site, and consisted of light to dark gray mudstones, with dipping layers. Each bedding

unit consisted of several water-bearing zones, alternating with confining zones. Characterizations of the physical and chemical properties of the collected core were carried out with a combination of non-destructive physical (porosity and permeability) and destructive chemical (mineralogical) methods.

Similar to what is described in Section 3.4, rocks were subjected to SEM images taken using a Zeiss Supra 35 VP Field Emission Scanning Electron Microscopy with Porosity calculated from ten SEM images with Image J software for all mudstones at the depth intervals of 45-50 feet bgs, 50-55 feet bgs, and 80-85 feet bgs (these three depth intervals correspond to the location of 3 water bearing fractures, as described in as described in Section 3.2.3). X-ray diffraction (XRD) was performed to identify the mineralogy of surfaces of rock types using a Scintag X1 powder diffractometer system. Total organic carbon content was measured using the same method as described in Section 3.4.3 on an Apollo 9000 TOC analyzer using EPA Methods 415.1 and 9060. As well, Ferrozine and 1,10-phenanthroline method were used to measure bulk Fe(II) and total Fe (Amonette and Templeton, 1998).

3.6.2-Groundwater characterization

Water samples were collected from within the known TCE plume within the Lockatong Formation (Lacombe and Burton, 2010) at the former Naval Air Warfare Center (NAWC) in Trenton, New Jersey. Groundwater investigations in NAWC bedrock have shown TCE concentrations in excess of 10 000 $\mu\text{g L}^{-1}$. Discrete interval packer sampling was performed during the core collection as described in Section 3.3 at 3 fracture intervals (45 to 50 feet bgs, 50 to 55 feet bgs, and 80 to 85 feet bgs) to determine TCE and reduced gas concentrations. Groundwater was analyzed for reduced gases (ethene/ethane/acetylene) using a Varian 3900 gas chromatograph equipped with a Flame Ionization Detector (FID) and Aluminum RT column, and VOCs via EPA Method 8260B.

Synthetic groundwater (SGW) was prepared based on the measured groundwater geochemistry at the NAWC. This groundwater consisted of deionized water amended with various salts as described in Table 4.2.1 (Lockatong formation). TCE (99.9% purity) and the salts used for the SGW were purchased from Sigma Aldrich (St. Louis, MO). The SGW was purged with nitrogen for a minimum of 60 min prior to use.

3.6.3-Diffusion-Reaction Cell Construction using 40 mL Vials

Gas tight extraction cells were designed and constructed to serve as a means to extract VOCs and reduced gases from targeted intervals of rock cores. Our design was a simpler and scaled-down version of the stainless steel diffusion cells described in Section 3.5.3. The new diffusion cells consisted of forty milliliter clear glass vials that were fitted with a sealable Mininert syringe valve cap (Restek Corporation, Bellefonte, PA) to facilitate sampling of the headspace. Experimental methods, with respect to monitoring and analysis to assess the extent of abiotic reactions, were performed similarly to that described in Section 3.5.2 for the preliminary assessment of the coupled diffusion and reaction of TCE.

Separate batch tests were completed to assess the gas tight nature of the containers during the time-scale of our experiments. We employed the use of 40ml clear glass VOA vials with Mininert™ Syringe Valves. Lids were sealed using JB Kwik epoxy, set in triplicate, and were flushed with helium. Four mL of 10,000 mg/L stock ethane was injected into them, and headspace samples were analyzed for ethane once a week for 3 weeks using a Varian 3900 GC-FID (Palo Alto, CA). Vials showed no reduction in ethane, thus these epoxy-sealed 40-mL vials were considered appropriate for the coupled diffusion/reaction experiments. Parallel experiments performed identically but without sealing the lids with epoxy showed substantial ethane losses over the 3-week period. Thus, the coupled TCE diffusion and reaction experiments performed in rock historically exposed to TCE (i.e., Section 3.6 experiments) were performed with epoxy-sealed lids.

3.6.4 Sealant Testing

The purpose for this sealant testing was to confirm that TCE was not going to penetrate through JB Kwik epoxy, thus confirming a no-flux boundary condition for TCE on the sealed edges of the rock rods (i.e., 1-dimensional diffusion only on the exposed face of the rock). A 3 mL amber vial was filled with 1mL of deionized water; a visible hole was created in the crimp sealed septa cap to allow for potential diffusive migration of TCE in to the vial. The vial and cap were then coated in JB Kwik epoxy and dried. The epoxy coated vial was placed into a 40mL vial containing 200mg/L TCE. After 20 days TCE was measured via headspace injection using a GC-FID, for both the 40mL vial, and headspace inside the 3mL vial. ***No TCE migration into the sealed 3 mL vial was observed, indicating that the epoxy formed an effective diffusion barrier for TCE.*** Thus, for rock rods that were sealed with epoxy, 1-dimensional diffusion of TCE through the one exposed face of the rock could be assumed.

3.6.5- Reaction Cell Experiments-TCE impacted Rock Core

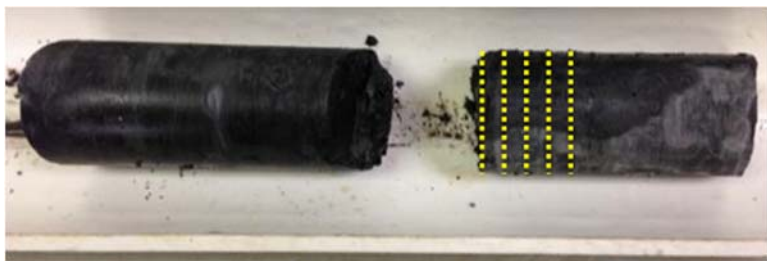
The objective of these experiments was to measure the abiotic reaction of TCE within the rock matrices of the three collected cores (45-50 ft bgs, 50-55 ft bgs, and 80-85 ft bgs) that had been within the historic TCE plume. The resultant TCE abiotic dechlorination rates were determined as a function of distance from the adjacent conductive fracture. Ultimately, results from these experiments were compared to rock samples spiked with TCE (Section 3.6.6) to determine the extent to which the rocks retained their capacity for abiotic dechlorination.

Rock cores were collected using a rotary coring method to obtain 2-in. diameter cores. The cores were collected using a minimum drilling speed and bit pressure to cut the core and maintain water pressure sufficient to remove cuttings and cool the drilling bit. Upon collection, rocks were placed on trays made from half of a 4-in. diameter, schedule 40 PVC pipe. The cores were examined to identify conductive fractures, as indicated by mineral weathering or deposition. Conductive fractures were identified at approximately 49, 53, and 83 feet below ground surface. Indurated rock cores on each side of each conductive fracture were then immediately transferred to a short PVC tray to protect the mechanical integrity of the collected cores during transportation and storage. The cores and tray were placed in nitrogen purged semi-transparent bags for visual inspection. Nitrogen gas was continually delivered into the bags (creating positive pressure) during this process. The cores, tray and semitransparent bags were then placed into nitrogen-purged foil-lined barrier bags and sealed immediately with a portable heat sealer, thus providing long-term anaerobic conditions for the collected samples.

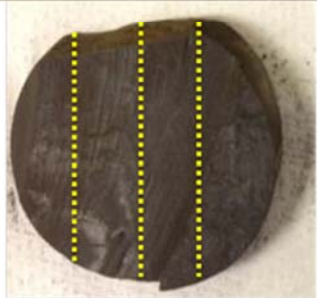
Laboratory experiments were performed to measure the abiotic reaction of TCE within the rock matrices of the three collected cores. Each core was cut at 1 cm intervals to create 5 parallel disks from the fracture face into the rock matrix. Each disk was then cut to create four rectangular rods of rock, which were approximately 6 g each (Figure 3.6.5). Three of the four rods were immediately placed in a 40-mL glass vial with a Mininert cap (epoxy sealed and helium purged, as described in Section 3.6.3), along with approximately 35 mL of anoxic SGW (2 mL of SGW were removed from the glass vial to create 2 mL of headspace for gas sampling). Control samples, containing no rock, also were prepared. All vials were amended with 300 mg L⁻¹ mercuric chloride to inhibit microbial activity. This preparation of the rock samples (where no TCE was added to the vials) was completed within 3 h of core collection. A picture of the epoxy-sealed vials containing the rock samples is provided in Figure 3.6.6. We note that the rock rods were not sealed with any epoxy, as all surfaces of the rock were available for the diffusion of TCE and daughter products from the rock.

Vial headspace in the un-spiked samples was monitored for TCE and reduced gases at 22 and 49 d. Vials were stored in an anaerobic chamber. All experiments were performed at approximately 20 °C. Headspace samples were analyzed for VOCs and reduced gases

(ethane/ethene/acetylene/propane) on a Varian 3900 gas chromatograph equipped with a Flame Ionization Detector (FID) and Aluminum RT column (GC-FID) until steady conditions were reached. Aqueous concentrations were determined by applying Henry's Law.



Core sliced going inwards
from fracture interface
(performed for each depth)



Four rods subsequently cut
from each slide

Figure 3.6.5. Preparation of rock slices and disks for coupled TCE diffusion and reaction experiments with rock collected from within the TCE plume at NAWC. Three of the four rods were immediately (same day of core collection) placed into the 40 mL vials, as described in Section 3.6.5. The fourth rod was sealed with epoxy, leaving only one exposed face, before placing into the 40 mL vials; vials containing these epoxy-sealed rock rods also received a TCE spike, as described in Section 3.6.6



Figure 3.6.6. Rock “rods” within the epoxy-sealed 40 mL vials used for evaluating abiotic dechlorination reactions in rock collected from within the TCE plume at NAWC.

3.6.6- Reaction Cell Experiments-Rock Core spiked with TCE

Since the detection of abiotic dechlorination products (e.g., ethane) in the reaction cells described in the previous section could be due to historically reacted TCE, and the back diffusion of the reduced gases from the matrix, additional testing was performed to verify the current abiotic dechlorination reactivity of the rocks. Our approach was to employ the use of a TCE spike to a subset of the rocks collected from within the TCE plume, where the observation of increased generation of dechlorination products in the presence of a TCE spike would confirm that the rocks were still capable of abiotic dechlorination reactions (despite decades of exposure to TCE).

The fourth rectangular rock rod from each disk described in Section 3.6.5 was used for a parallel experiment where a TCE spike (targeting a TCE concentration of 200 mg L^{-1}) was added to the 40-mL glass vial. For these experiments, only one face of the rock remained exposed, while all other five sides were sealed with JB Kwik epoxy (J-B Weld, Sulphur Springs, TX). Separate batch testing showed that any TCE degradation and daughter product generation due to TCE contact with the epoxy alone was small compared to reactions occurring between the rock and the TCE. Care was taken to ensure that the natural fracture face (which was present on the first slice from each of the three depth intervals), and the saw-cut face for the remaining 4 slices going inwards from the fracture, were the faces that remained exposed. Headspace was monitored for TCE and reduced gases for the spiked samples on days 14, 22, 90, and 118.

All vials were prepared in a nitrogen-purged anaerobic chamber. TCE and reduced gas (ethane, ethene, propane, and acetylene) concentrations were determined via headspace analysis using a Varian 3900 gas chromatograph equipped with a Flame Ionization Detector (FID) and Aluminum RT column. Aqueous concentrations were determined by applying Henry's Law. The detection limit for TCE was $100 \text{ } \mu\text{g L}^{-1}$; the detection limit for the reduced gases was $2 \text{ } \mu\text{g L}^{-1}$. The TCE-spiked samples also were monitored for organic acids (i.e., glycolate, lactate, acetate, formate) on a Dionex 600 Ion Chromatograph, as generation of these acids have been observed by others (Darlington et al., 2013).

3.7 Contaminant Profiles in Rock Matrices

The purpose of this testing was to examine the concentration profiles of PCE or TCE from the interface of hydraulically conductive fractures at fractured bedrock sites that have been historically impacted with TCE or PCE. The abiotic dechlorination activity of these rocks also was determined, and the relationship between abiotic dechlorination activity and PCE/TCE uptake into the rock matrix was examined. Understanding the dissolved contaminant uptake into the bedrock provides for an improved basis for predicting MNA time frames. Rocks were

collected from several different sites including Edwards AFB (Site 37 source area, which is part of the South Air Force Research Laboratory, California), Calf Pasture Point (Naval Construction Battalion Center, Rhode Island), Loring AFB (former Quarry area) and NAWC (Trenton, New Jersey).

3.7.1-Contaminant Site Bedrock Descriptions

Rock core from Edwards AFB - Site 37 was collected within the suspected PCE DNAPL source area. Collected rock core consisted of granitic bedrock characterized as quartz monzonite. Competent bedrock was encountered at depths ranging from 3 feet bgs to 64 feet bgs. Groundwater occurs in the fractured granitic bedrock with groundwater encountered at depths ranging from 24 feet bgs. This core was collected as part of our ongoing ESTCP Project ER-201210.

Rock core for laboratory testing was collected at Calf Pasture Point located in the northeast portion of the Naval Construction Battalion Center (NCBC) Davisville, RI area. According to USGS it is underlain by bedrock belonging to the Pennsylvanian Rhode Island Formation. These rocks consist of light to dark grey, fine to coarse grained meta-sandstone gneiss, shale, phyllite, and mica schist. The site location is adjacent to borehole location MW07-5R, which is within the TCE plume.

Rock core collected at Loring AFB was collected from GMZ-4 (former quarry area), within the known source area of the PCE bedrock plume. This core was collected as part of CB&I's contractual remedial work at Loring AFB. The Loring AFB bedrock consisted primarily of limestone. The rock used for testing was collected at a depth of approximately 93.5 ft below ground surface.

Rock core from the NAWC was described in Section 3.2.3. Rocks collected for experiments were collected from 69 ft bgs and 74 ft bgs, and are characterized as dark grey mudstone.

3.7.2- Rock Profile and Dechlorination Experiments

To further assess the impacts of abiotic dechlorination in the rock matrices on TCE or PCE uptake into the rock matrix, concentration profiles of these chlorinated ethenes emanating from the fracture interface into the rock matrix were measured. To evaluate the potential relationship between abiotic dechlorination reaction and the extent of PCE/TCE uptake into the rock, simple batch testing to measure the generation rate of dechlorination daughter products (e.g., ethene, ethane, acetylene, propane) also was performed; these reaction experiments were performed

similarly to the batch experiments described in Section 3.6.6, except that crushed rock samples were used instead of the intact “rods” of rock.

Rock cores from 4 different bedrock sites (noted above in Section 3.7.1), all impacted with either PCE or TCE, were evaluated. For several of these sites, ongoing ESTCP or remedial work was being performed, which served as an opportunity to collect the core as part of this SERDP study. Rock core was collected from NAWC (mudstone at 69 and 74 feet below ground surface), Calf Pasture Point (fractured quartzite and gneiss at 61 feet below ground surface), Loring AFB (limestone at 93.5 feet below ground surface), and Edwards AFB (granite at 76 and 98 feet below ground surface). Rock core was collected adjacent to hydraulically conductive fractures impacted with PCE or TCE.

Rock core collected at Calf Pasture Point and the NAWC was brought to CB&I’s laboratory where it was then sliced with a saw, taking thin slices of rock going inwards from the fracture interface. These slices of rock were then crushed using a chisel and hammer, and subsequently placed in methanol-filled jars for extraction (described in the paragraph below); rock collected at Loring AFB and Edwards AFB was crushed and extracted in methanol-filled jars in the field. For the rock core that was crushed in the laboratory, care was taken to ensure the rock core remained water saturated prior to crushing in the laboratory; the collected rock cores were immediately placed in sealed bags with excess water present in the bags. Given the measured rates of contaminant diffusion through the aqueous phase, losses of PCE and TCE during rock core shipping and storage were expected to be minimal. Rock core from NAWC was crushed and extracted within hours of collection; for Loring AFB, approximately 72 hours transpired.

For the rock core cut and crushed in the field, the rock was sliced parallel to the fracture interface using a tile saw with diamond bit blade into six 0.5 to 2 cm slices. The rock slices were crushed using a rock crusher (average particle size of less than 1 cm). The crushed pieces of rock (30g) were added to methanol preserved jars (30 mL methanol).

Both field- and laboratory-prepared methanol filled jars were submitted to CB&I’s Biotechnology Development & Applications Laboratory in Lawrenceville, New Jersey. Jars were stored at approximately 4 degrees C, and analyzed for VOCs by EPA Method 8260B. A minimum of two rounds of methanol sampling (over a 2 to 8 week period) were performed to ensure that there was no significant increasing trend in VOC concentrations due to slow diffusive release from the rocks.

3.8 Assessment of Abiotic Reaction with EDB.

*The purposed for these experiments was to attain insight into the diffusional and reactive processes occurring in the rock matrix with other contaminants (ethylene dibromide (EDB)), critical to DoD sites. **We note that all testing described in Section 3.8 was also performed using rock collected during the first phase of core collection, and therefore had not been historically exposed to TCE.***

EDB, also known as ethylene dibromide or 1,2-dibromethane, was selected for additional testing because it is an emerging contaminant of concern, and several recent studies indicate that this compound is amendable to dehalogenation by ferrous minerals. In addition, this compound is a halogenated ethane, and serves as a useful comparison to halogenated ethenes with regard to potential dehalogenation reactions in the rock matrices.

3.8.1- EDB Batch Testing to Assess Potential Interactions with the Epoxy

Batch experiments with EDB were performed to evaluate the sorption and reaction of this compound to the JB Kwick Epoxy. Remaining rocks from the NAWC initial rock core collection at NAWC were sliced 1cm wide and deep, and 4-5cm long with a diamond blade electric saw. The rocks were completely covered (i.e., no rock surfaces exposed) with the JB Kwick epoxy and allowed to dry. The epoxied rocks were placed into 40mL reaction vessels (similar to those described in Section 3.6.3) inside the anaerobic chamber, amended with anaerobic SGW averaging 35mL leaving 2mL headspace volume, and 200mg/L mercuric chloride to limit any biodegradation of the VOCs. The synthetic groundwater was also amended with 100mg/ L EDB. The cells were analyzed for reduced gases via headspace injection on the GC-FID at 1 week and 4 weeks.

3.8.2- Reaction Cell Experiments-EDB.

The objective of these experiments was to measure the abiotic reaction of EDB with ferrous minerals in rock matrices.

Rocks used in these experiments were collected during the initial drilling and characterization in January 2010 at NAWC, as described in Sections 3.2.2 and 3.4. Red sandstone from the Stockton formation, collected from approximately 45 to 49 ft bgs, and a light grey mudstone from the Lockatong formation, collected from 65 to 66 ft bgs, were used for these experiments. Rocks and reaction cells were prepared similarly to those described in Section 3.6.5. Rocks were cut using a diamond-tipped saw blade into rectangular rods that are approximately 1cm wide and deep, and

4 to 5cm long. The rock rods were sealed with JB Kwik epoxy leaving only one exposed face of the rod of rock available for diffusion and reaction. Rocks were placed into 40mL glass vials under anaerobic conditions, and amended with anaerobic synthetic groundwater averaging 35 mL leaving 2 mL headspace volume, and 200 mg/L mercuric chloride. The synthetic groundwater was also amended with 100 mg/ L EDB. The vials caps were sealed using epoxy to limit volatilization losses. Reaction cell experiments were prepared in triplicate, and also accompanied by a set of controls which contained no rock, but were otherwise prepared identically to those previously described.. The vials were incubated at room temperature under anaerobic conditions, and headspace samples were analyzed for reduced gases (ethane/ethene/propane/acetylene) on the GC-FID for up to 2 months.

3.9 Model Development to Assess Diffusion and Reaction in Rock Matrices

The purpose of this task was to develop a conceptual and mathematical model to describe the processes controlling the diffusion and reaction of TCE and oxidant within the rock matrix. The objective of the model was to develop a predictive tool for assessing the long term impacts of TCE present in the rock matrix on dilute contaminant plumes, particularly after contaminant flux has been reduced via natural attenuation and/or active remediation.

3.9.1- Diffusion in Anisotropic Rock Matrices

Predicting diffusional flux through bedrock matrices is challenging due to difficulties associated with predicting the effective diffusion coefficient through the rock matrix, which has resulted in continued efforts to improve predictions regarding both long and short-term impacts on the dissolved contaminant plume. For homogeneous isotropic rocks, Boving and Grathwohl (2001) showed that the effective diffusion coefficient through the rock matrix could be described by the following:

$$D_{\text{eff}} = D_{\text{aq}} \varepsilon^m$$

Eq. 3.9.1

where D_{eff} is the effective diffusion coefficient [cm^2/s], D_{aq} is the solute aqueous diffusivity [cm^2/s], and ε is the physical porosity of the rock matrix. The exponent m was determined to be 2.2 via regression using several rock types. While Eq. 3.9.1 provides a reasonable prediction of the effective diffusion coefficient through homogeneous isotropic rock, the applicability of this correlation for anisotropic rocks has not been fully assessed.

To describe diffusion through rocks with mineral bedding, the model presented in Eq. 3.9.1 is modified as follows:

$$D_{\text{eff}} = D_{\text{aq}} \varepsilon_o^m \quad \text{Eq. 3.9.1.1}$$

where ε_o is the apparent porosity measured in a specific orientation (i.e., normal or parallel to bedding), as measured via SEM, and m is an empirical fitting parameter.

Under steady state conditions, it has been shown (Crank, 1995, Boving and Grathwohl, 2001) that the mass of iodide per cross-sectional area that has migrated to the sink side of the diffusion cell across a rock of thickness d can be described by the following linear equation:

$$M = \frac{C_0 D_{\text{eff}}}{d} t - \frac{C_0 (\varepsilon + K_d \rho) d}{6} \quad \text{Eq. 3.9.1.2}$$

where M is the mass of solute per cross-sectional area that has migrated to the sink side of the diffusion cell [mg/cm^2], C_0 is the initial iodide concentration in the source reservoir [mg/cm^3], d is the rock thickness [cm], t is the time [s], K_d is the iodide sorption coefficient to the rock [cm^3/mg], and ρ is the rock density [mg/cm^3]. Plotting M versus t , and for the case where the iodide concentration on the sink side of the cell is much less than the iodide concentration on the source side of the rock, calculation of the steady-state slope from the experimental data can be used to determine the effective diffusion coefficient of iodide through the rock. Linear regressions were used to determine D_{eff} for each rock diffusion experiment.

3.9.2- Coupled Diffusion and First-Order Reaction Model for TCE in Rock Matrices

For TCE, the effective aqueous diffusion coefficient and the linear adsorption coefficient were determined using the analytical solution from Equation 3.9.1.2 to determine the mass per unit area migrating across the rock under steady state conditions

Plotting M versus t , and for the case where the TCE concentration on the sink side of the cell is much less than in the source side of the cell, calculation of the steady-state slope and intercept from the experimental data was used to determine D_{eff} and K_d , respectively. Thus, this steady state approach allowed for determination of K_d and D_{eff} independent of any determination of the reaction rate. We note that the methodology performed for this study focuses on measurement of a bulk effective diffusion coefficient, and any slow diffusion processes associated with slower diffusing tertiary (or greater) pore regimes, if present, were not assessed.

To determine the first order abiotic TCE degradation rate constant (assumed to occur due to ferrous minerals present in the rock), a numerical solution was employed. The one-dimensional aqueous diffusion and first order reaction equations describing these processes for TCE through the rock are as follows:

$$R \frac{\partial C}{\partial t} = D_{\text{eff}} \frac{\partial^2 C}{\partial x^2} - \frac{\rho K_d}{\epsilon} C \quad \text{Eq. 3.9.2.1}$$

$$R = 1 + \frac{\rho K_d}{\epsilon} \quad \text{Eq. 3.9.2.2}$$

where R is the retardation factor, C is the aqueous molar concentration (TCE or TCE reaction product), and k is the first order reaction rate constant (assumed to occur in the sorbed phase) [s^{-1}]. For TCE, D_{eff} and K_d were determined based on the analytical solution in Eq. 3.9.1.2 (i.e., independently determined from the steady state solution). The reaction term in Equation 3.9.2.1 was multiplied by -1 to describe the diffusion and generation of the dissolved gaseous TCE degradation products, where for simplicity gaseous degradation products (ethane, ethene, acetylene, and propane) were lumped together as a single aggregate species, thereby enabling a single lumped first order rate constant describing TCE degradation and daughter product generation to be determined. Based on the ratio of the aqueous diffusion coefficient of TCE compared to the daughter products, the D_{eff} for the daughter products was multiplied by 1.2 (Huq, 1968, Cussler, 1984, USEPA 1996). K_d for the daughter products was assumed to be the same as for TCE, as verified by ethane tracer tests performed through the rock in the diffusion cell. It is noted that, based on the model simulations, decreasing the K_d value for the daughter products by as much as an order of magnitude resulted in only a 10% change in the regressed first order rate constant.

Furthermore, to facilitate evaluation, a bulk first order degradation rate coefficient (k') is defined:

$$k' = k K_d \rho \quad \text{Eq. 3.9.2.3}$$

A finite difference model was developed in Microsoft Excel® to solve Eqs. 3.9.2.1 and 3.9.2.2 (Crank, 1995), and operator splitting (Lansner, 1999) was used to numerically solve the coupled diffusion and first order reaction processes in the diffusion cell experiments. Agreement between the analytical solution (Eq. 3.9.2) and the numerical solution for TCE diffusion through the rock verified the numerical model; the analytical solution for first-order reaction (Fetter, 1999) was used to verify the reaction portion of the numerical model (using a simulation with negligible diffusion). The time interval used in the model was less than 1600 seconds, and

the length interval was one-sixth of the rock thickness. The first order rate constant was determined via regression to the experimental data (i.e., TCE daughter products measured in the sink reservoir of the cell) using the Microsoft Excel® Solver non-linear regression package.

3.9.3- Determination of Observed Diffusivity of Permanganate into Rock Matrices

The observed diffusivity of the oxidant through the rock was determined by assuming one-dimensional diffusion and reaction of permanganate into the rock, which is described as follows:

$$\frac{\partial C}{\partial t} = D_{obs} \frac{\partial^2 C}{\partial x^2} \quad \text{Eq. 3.9.3}$$

where C is the manganese concentration, t is the time [s], D_{obs} is the observed diffusivity [cm^2/s], and x is the distance into the rock [cm]. Eq. 3.9.3 was solved assuming an initial condition of $C=0$ throughout the rock, a constant permanganate concentration at the rock interface (C_i , determined from the SEM data at the rock interface), and $C=0$ for all times at $x=\text{infinity}$. This one-dimensional semi-infinite medium solution is well known (Crank, 1995; Cussler, 2009):

$$\frac{C-C_i}{C_i} = \text{erf} \left[\frac{x}{\sqrt{4 D_{obs} t}} \right] \quad \text{Eq. 3.9.3.1}$$

Eq. 3.9.3.1 was regressed to the experimental data to determine the measured value for D_{obs} for each rock type. 95% confidence intervals for the regressed values were calculated based on the methodology described previously (Smith et al., 1998).

For comparison, a calculated value of the observed diffusivity was determined as follows:

$$D_{obs,calc} = \frac{D_{eff}}{R} \quad \text{Eq. 3.9.3.2}$$

$$R = 1 + \frac{\rho \alpha}{\theta C_{ox}} \quad \text{Eq. 3.9.3.3}$$

where R is the retardation factor, θ is the rock porosity (water uptake porosity, measured by Schaefer et al., 2013 for each of the rock types examined), and ρ is the rock density [assumed to be 2.6 kg/L]. The rock oxidant demand, α [g/kg], was determined from the oxidant demand tests described in Section 3.4.4. C_{ox} is the permanganate concentration in the reservoir. D_{eff} is the effective diffusion coefficient (where D_{eff} accounts for the decrease in diffusion due to an increased tortuous pathway (Fetter, 1999) for permanganate through the rock [cm^2/s]. D_{eff} values were previously calculated for each rock type for either iodide or trichloroethene as noted above

in Section 3.9.1 and 3.9.2; multiplying these values by the ratio in aqueous diffusivity between permanganate ($4.0 \times 10^{-5} \text{ cm}^2/\text{s}$, (Kyriacou et al., 2006)) and the previously employed solute allowed for determination of D_{eff} for permanganate. Thus, the calculated values of $D_{\text{obs,cal}}$ from Eqs. 3.9.3.2 and 3.9.3.3 were compared to the measured value of D_{obs} from Eq. 3.9.3.1.

4.0 Results and Discussion

4.1. Intact Rock Core Collection – Phase I (outside the TCE plume): Verifying the Cores were Minimally Disturbed

Exposure to Dissolved Oxygen

Dissolved oxygen concentrations in the re-circulating drilling fluids generally remained at or below approximately 1.5 mg/L. This DO concentration was only about 3-times greater than the naturally occurring DO levels (~0.5 mg/L) in conductive fractures at the NAWC site, based on groundwater DO readings collected from both the Stockton and Lockatong formations in the vicinity of where the bedrock cores were collected prior to coring. Thus, considering the relatively short duration to which the bedrock was exposed to this nominal increase in DO, artificial oxidation of the bedrock matrices during coring activities were judged to be insignificant.

Bromide Tracer

Results of the bromide tracer testing used to determine the extent of drilling fluid impacts on the rock matrices are summarized in Table 4.1. Our results show that the bromide concentrations in the rock matrices were approximately 10% of the bromide concentrations present in the re-circulating drilling fluids. Thus, the impact of the drilling fluids on the rock matrices was minimal. The low permeability of the rock matrix limited the entry of drilling fluids, and any migration of solutes into the rock matrix were likely controlled by slow diffusion processes. This observation, coupled with the observation that the DO levels in the re-circulating fluids were only nominally greater than background DO levels, indicates that drilling fluids and coring activities did not result in artificial oxidation of bedrock matrix minerals.

Table 4.1. Results of bromide tracer testing in rock matrices. Rock cores from two boreholes (B1 and B6) collected from the NAWC site were examined. Borehole locations are shown in Figure 3.2.2

| Rock Type | Borehole | Approximate Depth (feet below ground surface) | Bromide concentration in rock ¹ (mg/L) | Bromide concentration in re- circulating drilling fluid (mg/L) |
|-----------|----------|---|---|--|
| Mudstone | B1 | 50 | 20 | 362 |
| Mudstone | B1 | 65 | 21 | |
| Sandstone | B6 | 30 | 69 | 345 |
| Sandstone | B6 | 44 | 58 | |
| Sandstone | B6 | 59 | 12 | |

NOTES:

¹ Based on a 10% rock matrix porosity, as estimated using water uptake testing

SEM Imaging

Results from 3 of the imaged cores are shown in Figures 4.1 through 4.1.2. Results from these core locations all indicated that there was no significant micro-fracturing that could have occurred during the drilling process. Images taken from the edges of the cores were similar to those in the center of the core with nearly identical porosity distribution. No artificial fractures were visible near the edges of the cores. These results further support that no alteration of the rock porosity occurred during the coring process. Thus, drilling did not measurably alter the porosity of the collected rocks.

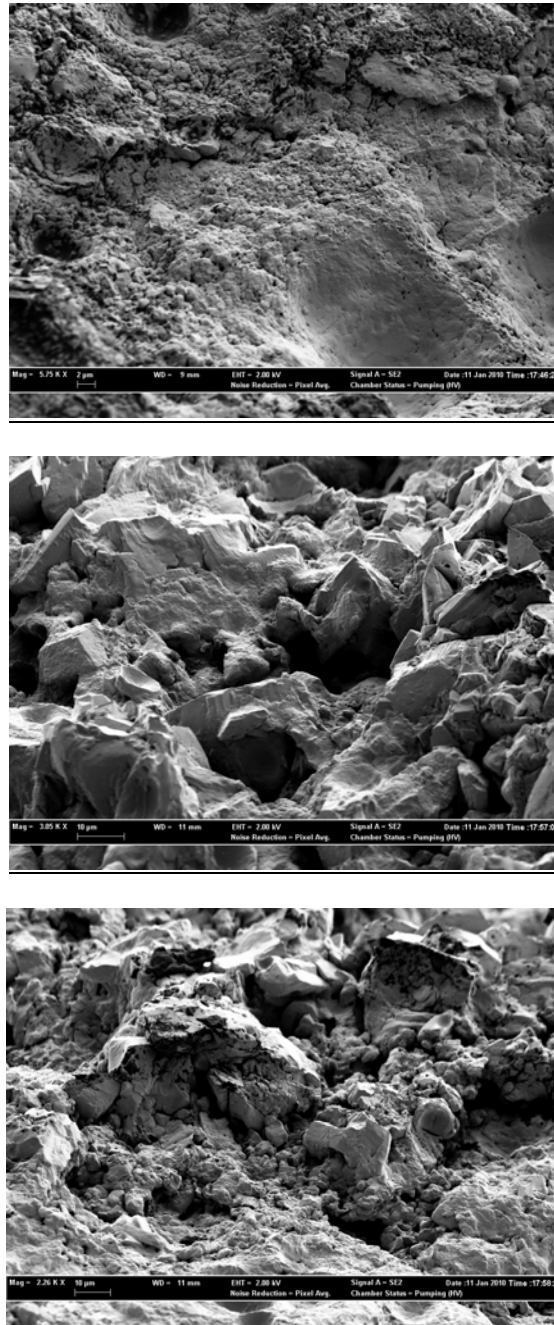


Figure 4.1. SEM images along a fracture face of a mudstone core collected from approximately 36 ft. bgs at borehole 1. Images show (from top to bottom) the left, center, and right of the core along a fracture face. Images from a total of 4 coring locations were collected and evaluated. No evidence of micro-fracturing was observed in any of the images, and images of the center of the cores were similar to those collected along the edges.

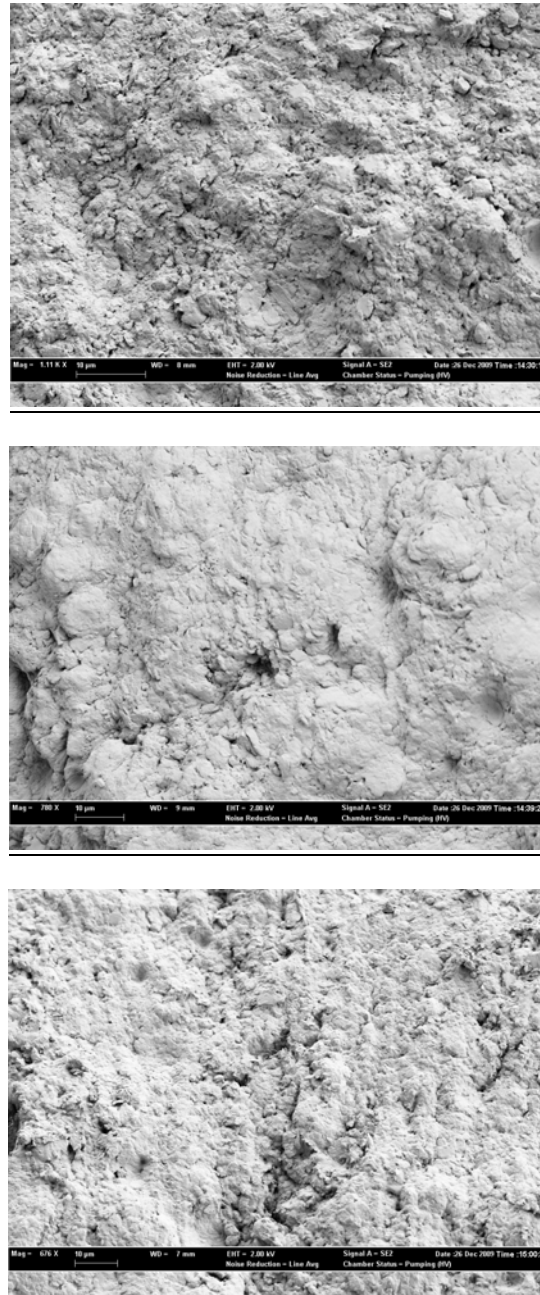


Figure 4.1.1. SEM images along a fracture face of a mudstone core collected from approximately 50 ft. bgs at borehole 1. Images show (from top to bottom) the left, center, and right of the core along a fracture face. No evidence of micro-fracturing was observed in any of the images, and images of the center of the cores were similar to those collected along the edges.

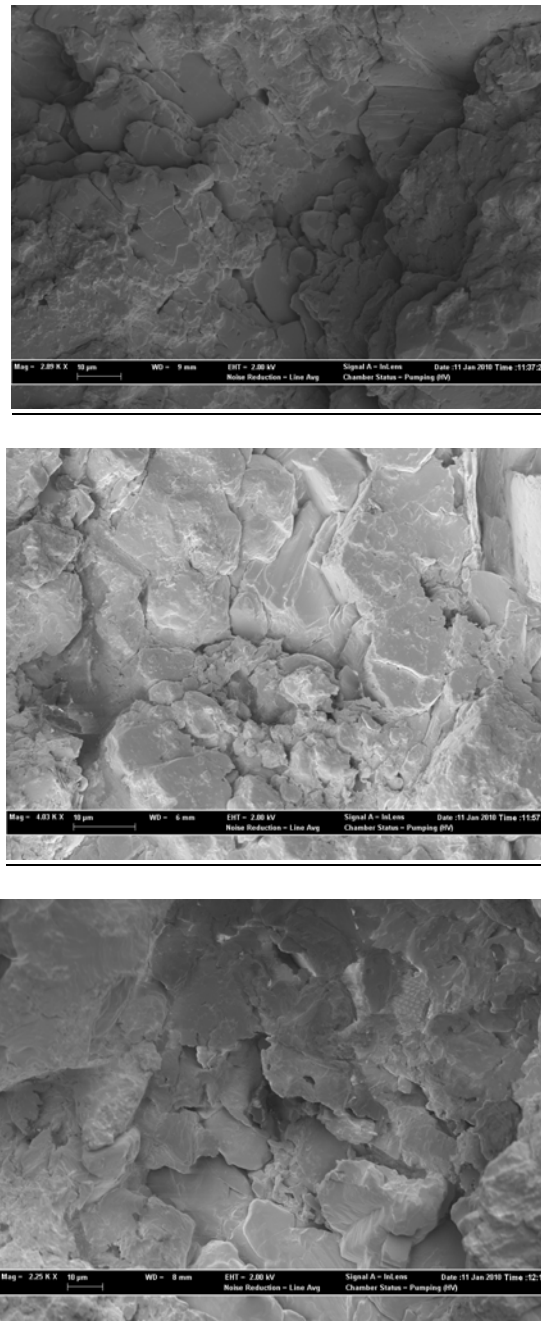


Figure 4.1.2. SEM images along a fracture face of a mudstone core collected from approximately 43 ft. bgs at borehole 6. Images show (from top to bottom) the left, center, and right of the core along a fracture face. No evidence of micro-fracturing was observed in any of the images, and images of the center of the cores were similar to those collected along the edges.

4.2 Groundwater Characterization

Groundwater samples were collected to provide a geochemical characterization of the site groundwater at the NAWC outside the TCE plume. Groundwater was collected from both the Stockton and Lockatong Formations. Analytical results from the pH, alkalinity, and anions analyses are summarized in Table 4.2. Groundwater collected from each location is similar, but with significant differences in chloride and ferrous iron.

Table 4.2. Results of groundwater characterization from samples collected from the two coring locations outside the TCE plume at the NAWC site.

| Parameter | Lockatong Formation | Stockton Formation | Units | Method Code |
|------------------------------|----------------------------|---------------------------|--------------|--------------------|
| Anions | | | | |
| Fluoride | 0.16 | 0.06 | mg/L | EPA 300.0 |
| Chloride | 16.1 | 2.83 | mg/L | EPA 300.0 |
| Nitrite as N | 0.1 | 0.1 | mg/L | EPA 300.0 |
| Sulfate as SO ₄ | 18.7 | 12 | mg/L | EPA 300.0 |
| Bromide | 0.1 | 0.1 | mg/L | EPA 300.0 |
| Nitrate as N | 0.1 | 0.13 | mg/L | EPA 300.0 |
| Chlorate | 0.1 | 0.1 | mg/L | EPA 300.0 |
| | | | | |
| Total Metals Analysis | | | | |
| Calcium | 32800 | 18400 | ug/L | SW846 |
| Magnesium | 11800 | 4770 | ug/L | SW846 |
| Potassium | 1920 | 3910 | ug/L | SW846 |
| Sodium | 19500 | 7410 | ug/L | SW846 |
| | | | | |
| Limited Chemistry | | | | |
| Alkalinity/CaCO ₃ | 119 | 54.3 | mg/L | SM2320B |
| pH | 7.75 | 6.24 | SU | SM4500-H B |
| Fe ²⁺ | 0.25 | 6.65 | mg/L | Hach Test |

A synthetic groundwater (SGW) was prepared based on the groundwater geochemistry at the former NAWC facility. This groundwater was used in all of the diffusion experiments, and consisted of deionized water amended with contents listed in Table 4.2.1. Lockatong SGW was used in experiments with rocks collected from the Lockatong Formation, and Stockton SGW was used with the rock collected from the Stockton Formation. To maintain anaerobic conditions SGW was purged with nitrogen for a minimum of 60 minutes prior to use.

Table 4.2.1. Composition of Synthetic Groundwater (SGW) recipes for the two coring locations. All reagent grade chemicals from Sigma-Aldrich 137 (St. Louis, MO).

| Synthetic Groundwater | Ions | Concentration (mg/L) | pH |
|-----------------------|---|--------------------------------|----------------------------|
| Lockatong | CaCl ₂ – 2H ₂ O NaHCO ₃ NaNO ₃ MgSO ₄ – 7H ₂ O KCO ₃ | 120 70 0.10 60 4.0 | Adjusted to 7.7 using NaOH |
| Stockton | CaCl ₂ - 2H ₂ O NaHCO ₃ NaNO ₃ MgSO ₄ - 7H ₂ O KCO ₃ | 68 27 0.15 35 7.0 | Adjusted to 6.2 using HCl |

4.3 Rock Characterization

Detailed physical, geochemical, and mineralogical analyses were performed on rocks collected at NAWC outside the TCE plume.

4.3.1. Rock porosity

Initial porosity measurements were taken as a function of bedding orientation. SEM images for each rock type were taken parallel and normal to bedding. These SEM-based porosity measurements (described in Section 3.4.1) are discussed in greater detail in Section 4.4.2, where they are discussed with respect to their impacts on diffusion coefficients normal and parallel to mineral bedding. The water-uptake porosities (or, water accessible porosities) for each rock type are provided in Figure 4.3.1, as well as the SEM and Hg porisimetry-based porosity measurements. As shown in Table 4.3.1, these water uptake porosities were in excellent

agreement with porosity measured via mercury intrusion and SEM analysis (taking the average SEM value for the normal and parallel bedding orientations). SEM-measured porosity is actually a measure of the effective pore cross-sectional area in the orientation (e.g., normal or parallel to bedding) of the image. It has been well established that the pore cross-sectional area (or formation factor) can be a function of orientation in rocks (Worthington, 2001; Dullien, 1992). Here, we employed the use of SEM to estimate an “apparent porosity” both normal and parallel to bedding. Although porosity is a scalar quantity that is independent of orientation, our use of “apparent porosity” incorporates the effects of pore cross-sectional area associated with bedding orientation. In a similar approach, Desbois et al. (2010) noted differences in “porosity fabric” in clay cross sections normal and parallel to bedding, where a clear difference in the pore cross-sectional area was observed in the presented SEM images. Sato and Suzuki (2003) hypothesize that differences in these pore cross-sectional areas (or, apparent porosities) as a function of orientation could be responsible for the anisotropic diffusion observed in their experiments. Based on the water uptake and mercury intrusion testing, the effective porosity for each rock type is similar, ranging between 6% and 9%. For the dark gray mudstone, the SEM-calculated apparent porosity was greater in parallel bedding compared to normal bedding. The porosities for the tan sandstone and red sandstone were similar in each orientation. It is significant to note that, in all cases, the average apparent porosity (normal and parallel to bedding) for each rock was approximately equal to the porosity measured via water uptake and mercury intrusion, thereby confirming that the apparent porosity measured via SEM (and based on the fraction of pore cross-sectional area in each orientation) provided a reasonable description of the porosity. Similar agreement between fractional pore cross-sectional area and porosity was observed by Yokoyama and Nakashima (2005).

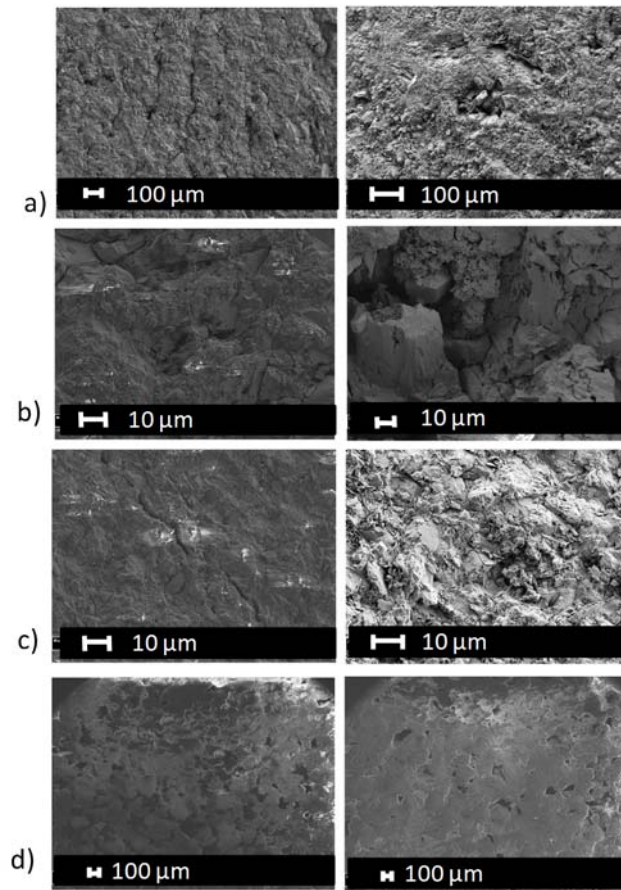


Figure 4.3.1. SEM images of normal (left) and parallel (right) orientations for the a) red sandstone, b)tan sandstone, c) dark gray mudstone, and d) quarry sandstone. Multiple SEM images were collected for each sandstone orientation.

Table 4.3.1. Rock mineralogy and porosity for the rocks used in the diffusion and reaction experiments. *The last three rocks in the table were collected during the second phase of core collection (i.e., within the TCE plume).* NM = not measured.

| Rock Type | Mineralogy (%) | Total Fe (mmol/g) | Fe²⁺ (mmol/g) | Water Uptake Porosity | SEM Porosity | Hg Intrusion Porosity |
|-----------------------------|--|--------------------------|---------------------------------|------------------------------|----------------------------------|------------------------------|
| Red Sandstone | albite (51), quartz (35), montmorillonite (6.4), muscovite (2.5), hematite(2.2), goethite (0.9), siderite (0.2), biotite (0.1), lepidocrocite (0.1) | 0.03 | 0.01 | 0.061 | Normal: 0.074 Parallel: 0.069 | 0.057 |
| Tan Sandstone | quartz (48), albite (39), pyrophyllite (10), muscovite (2.5), tourmaline (0.5) | 0.09 | 0.005 | 0.079 | Normal: 0.068 Parallel: 0.085 | 0.071 |
| Light Gray Mudstone | albite(26), kaolinite(12), chlorite(11), orthoclase(11), vermiculite(9.4), illite(8.8), clinochlore(5.9), brookite(4.4), dolomite(4.0), calcite(1.9), montmorillonite(1.6), biotite(1.6), microcline(1.3), quartz(1.2) | 1.23 | 0.38 | 0.064 | NM | NM |
| Dark Gray Mudstone | albite(25), clinochlore(15), kaolinite(13), illite(15), chlorite(8.7), microcline(7.1), dolomite(5.4), quartz(3.2), orthoclase(2.7), calcite(2.6), vermiculite(1.5), biotite(1.0) | 0.96 | 0.30 | 0.089 | Normal: 0.050 Parallel: 0.11 | 0.080 |
| Pyrite-Rich Mudstone | pyrite(59), dolomite(20), ankerite(9.4), anorthite(5.3), iron-mica(3.1), quartz(2.2), biotite(0.5), goethite(0.4) | 1.23 | 0.73 | 0.064 | NM | NM |
| Pyrite Seam | pyrite (100) | 5.0 | 4.6 | 0.030 | NM | NM |
| 90BR49' | albite(45), dolomite(19.2), microcline(19), muscovite(7), orthoclase(7), quartz(2.8) | 2.90 | 0.845 | 0.086 | NM | NM |
| 90BR53' | albite(54), dolomite(7.6), mica(16.5), orthoclase(12.5), dickite (9.6) | 3.00 | 1.61 | 0.073 | NM | NM |
| 90BR83' | albite(41.6), chlorite (14.3), muscovite(15.8), mica(19.8), quartz(8.5) | 5.40 | 3.79 | 0.064 | NM | NM |

4.3.2. Rock mineralogy

Mineralogical analyses of the rocks show that the rocks vary in their mineral composition (Table 4.3.1) and that all rocks contain measurable levels of total and ferrous iron, Fe(II), with the largest quantities of ferrous iron expectedly observed in the rocks containing visible pyrite minerals. It is possible that the reactive portion of Fe(II) is adsorbed on these fine-grained clay materials, and not necessarily associated with clay mineral structures (Szecsody et al., 2004, Stucki et al., 1984).

Tan Sandstone was collected from 18.7 to 23.7 ft bgs. The iron in this core is very low at 0.09 mmole/g total and 0.005 mmole/g Fe(II). The mineralogy consists mostly of quartz, albite, pyrophyllite, and muscovite. This core contained water bearing fractures around 20 ft, 22 ft, and 23 ft, and had three distinct color zones going from tan, green, black, and red.

Red sandstone was collected from 44.9 and 49 ft. bgs. The iron is very low, 0.03 mmol/g total Fe and 0.01 mmol/g Fe(II) of rock. The overall mineralogy is quartz, albite, montmorillonite, muscovite and hematite along with trace amounts of goethite, siderite. Hematite is the apparent cause for the red color. X-mapping results show that the whole sample is homogeneously made up of quartz and feldspars, and the dark bandings do not show up. The banding is possibly due to organic impurities. There is Fe, but no sulfur in the sample, consistent with XRD identification of hematite (Fe_2O_3), possibly on the fracture surface (Figure not shown). The BET surface area of these two samples is 1.2 and 3.0 m^2/g , respectively.

Dark and Light Gray Mudstones were collected at depths of 43 and 49 ft. bgs. Visually these two are homogeneous mudstones with total iron content ranging from 0.96 to 1.23 mmol/g, and a Fe(II) content ranging from 0.3 to 0.38 mmol/g, respectively. The overall mineralogy is dominated by feldspars, layer silicates (including clay minerals). There are no iron oxides. The BET surface area of these two samples is 1.7 and 6.3 m^2/g . An additional dark grey mudstone was cored at 66.9 ft. bgs. The overall mineralogy is dominated by feldspars and layer silicates, but there are some important differences. For example, on the fracture surface, there is iron oxide goethite (FeOOH).

The Pyrite Seam was cored at a depth of 67.5 ft. bgs. Visually it is a pyrite seam. Both total Fe and Fe(II) contents (5.0 and 4.6 mmole/g) are much higher within the pyrite seam than in the bulk rock, as consistent with the presence of abundant pyrite. XRD analyses confirmed pyrite (FeS_2) within the pyrite seam, but it is absent in the bulk rock. SEM X-maps confirmed identification of pyrite in the seam. In addition to pyrite, other surrounding minerals include various feldspars (sanidine, albite, microcline), layer silicates, and carbonates.

4.3.3. Total Organic Carbon

Naturally present reactive reductants, such as total organic carbon (TOC) and reduced forms of iron, manganese, and sulfur, can impact the effectiveness of ISCO technology. For this reason it was important that TOC be measured in the rock matrix. Results can be seen in Table 4.3.4. TOC ranged from 16.7 g/kg of rock to 463 g/kg of rock with the tan sandstone having the least and the dark gray mudstone containing the most organic carbon. This result suggests that TOC will be readily available in the dark and light gray mudstones to reduce oxidants.

Table 4.3.4. Rock total organic carbon (TOC) and rock permanganate oxidant demand in g/kg.

| Rock type | Total organic carbon (g/kg) |
|---------------------|------------------------------------|
| Dark gray mudstone | 463.0 |
| Light gray mudstone | 132.0 |
| Red sandstone | 27.3 |
| Tan sandstone | 16.7 |

4.3.4 Rock Oxidant Demand

In order to assess the chemical reactivity of persulfate and permanganate with the rock matrix, oxidant demand testing was performed. Results for total oxidant demand for selected rock types based on permanganate and persulfate batch reactions are provided in Table 4.3.5.

The crushed rocks (~1cm) displayed varying degrees of oxidant demand, with the sandstones exhibiting low oxidant demand and the mudstones exhibiting high oxidant demand. All the oxidant (both permanganate and persulfate) was consumed in the dark gray mudstone experiments, thus the oxidant demand is listed as >2.8g oxidant/kg rock for this rock type. The light gray mudstone also showed elevated levels of oxidant demand at 1.1g oxidant/kg rock for permanganate and 1.0g. oxidant/kg rock for persulfate. One reason for this high reactivity in the mudstones is the high organic content, as shown in Table 4.3.5. Natural organic matter in the dark gray mudstone and light gray mudstone is likely the cause for the elevated oxidant demand in these rocks. This result is consistent with a previous study where reported oxidant demand values were highly correlated with TOC, but not with amorphous Fe (Xu and Thomson, 2009). Both sandstones exhibited low oxidant demand, as the sandstones have negligible organic matter.

The rocks showed increased oxidant demand in powdered form compared to the crushed pieces (Table 4.3.5) Oxidant demand increased by approximately 10-fold for the permanganate exposed rocks, and increased from 3-10 fold for persulfate exposed rocks compared to the results using 1-cm sized crushed rock particles. Using the rock powder exposed more of the internal rock matrix

to the oxidants, resulting in an increased in the observed oxidant demand. These elevated values may represent the true oxidant demand for the rocks, and are likely more reflective of the oxidant demand available to oxidants as they diffuse through the rock matrix.

Table 4.3.5. Total oxidant demand per rock type based on permanganate and persulfate in g.Ox/kg rock

| Rock type | Persulfate demand (g oxidant/kg rock) | | Permanganate demand (g oxidant/kg rock) | |
|---------------------|--|----------|--|----------|
| | Crushed | Powdered | Crushed | Powdered |
| Tan sandstone | 0.16 | 1.3 | 0.11 | 4.2 |
| Red Sandstone | 0.32 | 1.9 | 0.19 | 4.8 |
| Light Gray Mudstone | 1.1 | 6.9 | 1.0 | 10.0 |
| Dark Gray Mudstone | >2.8 | 9.4 | >2.8 | 22.0 |

4.4. Diffusion Experiments-Outside the TCE Plume

4.4.1 Preliminary Diffusion and Reaction Experiments

NOTE: These are the results of initial screening testing prior to the more quantitative coupled diffusion and reaction experiments performed in the diffusion cell. These results served as an initial guide for subsequent experiments.

Batch Experiments were conducted for both iodide and TCE to monitor their sorption and reaction with rock matrices. Results for the iodide batch sorption tests are shown in Table 4.4.1.1. Both a linear sorption coefficient and a matrix retardation factor are calculated. Results indicate that measurable sorption of the iodide to the rocks occurred. Sorption in the mudstones was greater than in the sandstones, apparently due to the presence of various clay minerals such as clinocllore, vermiculite (Table 4.3.1). Interestingly, the sorption of iodide to the mudstones in the rod batch experiments was significantly less than in the crushed mudstone experiments; this discrepancy (as discussed for the TCE batch results noted below) was even more apparent for TCE. Our current hypothesis for this discrepancy is that the manual crushing procedure we used to generate the rock particles created a noticeable quantity of rock powder (no noticeable powder was generated for the sandstones). ***These very fine rock particles may have facilitated solute sorption due to artificial enhancement of the rock surface area.***

Table 4.4.1.1. Partition coefficient (K) and matrix retardation factor (R) for iodide based on batch and rod experiments.

| | Red Sandstone | Weathered Mudstone | Light Grey Mudstone | Dark Grey Mudstone | Sandstone Block | Light Grey Mudstone | Dark Grey Mudstone |
|-----------|---------------|--------------------|---------------------|--------------------|-----------------|---------------------|--------------------|
| Parameter | Crushed Rock | | | | | Rods | |
| K, L/kg | ~0 | 0.027 | 0.11 | 0.46 | ~0 | 0.091 | 0.1 |
| R | 1 | 1.4 | 5.4 | 14 | 1 | 4.6 | 4.0 |

Results for the TCE batch sorption tests are shown in Table 4.4.1.2. Both a linear sorption coefficient and a retardation factor are calculated, as well as the molar ratio of TCE dechlorinated (based on generation of ethene, ethane, and acetylene daughter products) to ferrous iron. Sorbed TCE mass was calculated as the difference in mass between the controls and the rock-amended samples, less the mass of daughter products generated. Data (not shown) indicate that sorption equilibrium was reached within approximately 3 weeks for the rod experiments; similar kinetic testing was performed on the crushed rock experiments.

Measurable sorption of TCE was observed on all of the rocks tested, except for the red sandstone. Apparently, the sandstones were dominated with quartz and feldspars which did not contain sufficient reactive surface area for measureable TCE sorption in these experiments. The extent of TCE sorption observed in the mudstone rods is substantially less than observed in the crushed mudstones. As previously discussed for iodide, our hypothesis is that the generation of fine rock powders during the crushing process resulted in an artificial increase in sorption capacity for these rocks.

Finally, dechlorination daughter products were observed for all the rock types tested. However, the extent of dechlorination did not appear to be related to the ferrous iron content of the rock. This relationship is further explored in Section 4.4.3. To determine the first order TCE dechlorination rate constant in the intact (rod) light gray mudstone, the diffusion model (Eq. 3.9.2.1) was applied to this system, where a no flux boundary ($D=0$) was used on the epoxy-sealed faces of the rod, and back-diffusion of daughters into the 40-mL reservoir was measured. Values of the effective diffusion coefficient and sorption coefficient (K_d) determined from the light gray mudstone diffusion cell experiments explained in Section 4.4.3 were used in the model, thus the only regressed parameter in the model was the first order rate constants. The regressed rate constant for each experiment was $9 \times 10^{-9} \text{ s}^{-1}$, which is in good agreement with the values measured in the diffusion cell experiments ($6.4 \pm 4.1 \times 10^{-9} \text{ s}^{-1}$), as discussed in Section 4.4.3. This result also suggests that any impacts from the metallic components in the diffusion cell did not have a measureable impact on the abiotic dechlorination rate constants.

Table 4.4.1.2. Partition coefficients (K) and matrix retardation factors (R) for TCE based on crushed rock and rod experiments. The molar ratio of TCE reacted (sum of ethene, ethane, and acetylene) to ferrous iron also is provided.

| | Red Sandstone | Weathered Mudstone | Light Grey Mudstone | Dark Grey Mudstone | Pyrite seam | Light Grey mudstone | Dark Grey Mudstone |
|--|---------------|--------------------|---------------------|--------------------|-------------|---------------------|--------------------|
| Parameter | Crushed Rock | | | | | Rods | |
| K, L/kg | 0.17 | 0.050 | 9.4 | 110 | 1.3 | 0.036 | 0.81 |
| R | 8.3 | 1.7 | 380 | 3200 | 110 | 15 | 24 |
| mmole TCE dechlorinated: mmole mineral Fe ²⁺ | 0 | 0.0022 | 0.0029 | 0.0030 | 0.012 | > 0.0057 | > 0.0089 |

4.4.2 Effective Diffusion Coefficients- Bedding Plane Orientation Experiments

Diffusion of dissolved contaminants into or from bedrock matrices can have a substantial impact on both the extent and longevity of dissolved contaminant plumes. For layered rocks, bedding orientation can have a significant impact on diffusion. A series of laboratory experiments was performed on minimally disturbed bedrock cores to measure the diffusive flux both parallel and normal to mineral bedding of four different anisotropic sedimentary rocks.

Typical iodide diffusion curves, based on measured iodide concentrations in the sink reservoir of the stainless steel diffusion cell, are shown in Figure 4.4.2.1. The initial non-linear unsteady-state portion of the diffusive elution curve, which occurred within the first 12 days for the experiment shown in Figure 4.4.2.1, was not used in the linear regression. The regressed slope was used in Eq. 3.9.1.2 of Section 3.9.1 to determine the effective diffusion coefficient. The standard errors of the effective diffusion coefficients calculated from regression of the slope for individual diffusion experiments were less than 13% of the regressed value (and were typically less than 8% of the regressed value). Effective diffusion coefficients measured in each rock for both diffusion parallel and normal to mineral bedding are shown in Table 4.4.2.1. Results indicate that the regressed diffusion coefficients were reasonably repeatable. Tests performed on separately cut rock sections for the dark gray mudstone and red sandstone suggest that the rock sections used within the diffusion cell were generally representative of the local rock geology (with respect to iodide diffusion). The magnitude of the measured effective diffusion coefficients are within the range measured by others for sedimentary rocks (Boving and Grathwohl, 2001; Descostes et al., 2008; Cavé et al., 2010)

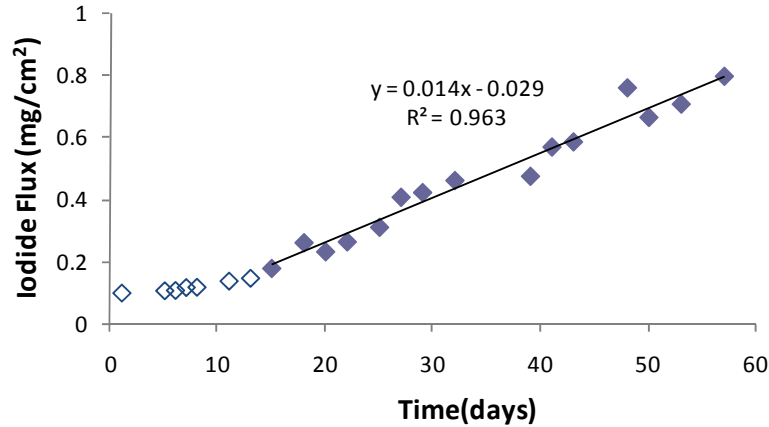


Figure 4.4.2.1 Iodide diffusion data (quarry sandstone). Non-filled symbols were not used in the regression, as these data were collected during the initial unsteady-state phase of the experiment. The slope, intercept, and correlation coefficient for the regression are shown.

Table 4.4.2.1 Measured iodide effective diffusion coefficients for each rock type and orientation. \pm values represent the standard error.

| Rock Type | Number of Experiments | Effective Diffusion Coefficient (cm ² /s) |
|--------------------|--|--|
| Red Sandstone | Normal: 2 Parallel: 4 ¹ | Normal: $1.8 \pm 0.6 \times 10^{-7}$ Parallel: $2.3 \pm 0.4 \times 10^{-7}$ |
| Tan Sandstone | Normal: 2 Parallel: 3 | Normal: $1.3 \pm 0.4 \times 10^{-7}$ Parallel: $1.9 \pm 0.4 \times 10^{-7}$ |
| Dark Gray Mudstone | Normal: 3 ² Parallel: 3 ² | Normal: $4.9 \pm 1.3 \times 10^{-8}$ Parallel: $2.8 \pm 0.5 \times 10^{-7}$ |
| Quarry Sandstone | Normal: 3 Parallel: 2 | Normal: $6.5 \pm 1.1 \times 10^{-7}$ Parallel: $6.8 \pm 0.8 \times 10^{-8}$ |

¹ Three separate cut rock sections were used.

² Two separate cut rock sections were used.

For the red sandstone, no significant difference in the magnitude of the effective diffusion coefficient was observed when comparing diffusion parallel and normal to bedding. For the tan sandstone, a slightly greater effective diffusion coefficient was observed parallel to bedding compared to normal to bedding, but this difference was minimal. For the dark gray mudstone,

diffusion parallel to bedding was approximately 7-times greater than diffusion normal to bedding; diffusion was approximately 10-times greater perpendicular to bedding than parallel to bedding in the quarry sandstone.

These results, consistent with the observations of others (Van Loon et al., 2004; Esteban et al., 2006; Cavé et al., 2010), show that bedding orientation can have a substantial impact on the effective diffusion coefficient through the rock. What is further demonstrated in this current work is that the effective diffusion coefficient anisotropy is directly related to the apparent porosity anisotropy (or fraction of pore cross-sectional area) as determined via SEM imaging, as shown in Table 4.4.2.2. The extent of available pore cross-sectional area controls the rate of diffusion. For the red sandstone, where no statistical difference in SEM-measured apparent porosity is observed as a function of bedding orientation, no anisotropy is observed for the effective diffusion coefficient. For the tan sandstone, where the SEM-measured apparent porosity is slightly greater in the parallel to bedding compared to normal to bedding, the effective diffusion coefficient correspondingly is slightly greater in the parallel orientation compared to the perpendicular orientation. Similar correspondence is demonstrated in the quarry sandstone and dark gray mudstone, where a substantially greater SEM-measured apparent porosity in one orientation corresponds to an increased effective diffusion coefficient in that same orientation. Thus, the apparent porosity as measured by SEM provides an explanation for the differences in the effective diffusion coefficient in parallel versus normal bedding orientations, as the change in apparent porosity (or fraction of pore cross-sectional area) relative to a given bedding orientation results in a proportional change in the effective diffusion coefficient. These experimentally coupled apparent porosity and diffusion measurements are in qualitative agreement with the diffusion simulations performed by Nakashima et al. (2008).

Table 4.4.2.2. Characterization of rock porosities.

| Rock Type | SEM Apparent Porosity | Water Accessible Porosity | Hg Intrusion Porosity |
|---------------------------|--|----------------------------------|------------------------------|
| Red Sandstone | Normal: 0.074 ± 0.004 Parallel: 0.069 ± 0.007 | 0.061 | 0.057 |
| Tan Sandstone | Normal: 0.068 ± 0.005 Parallel: 0.085 ± 0.002 | 0.079 | 0.071 |
| Dark Gray Mudstone | Normal: 0.050 ± 0.006 Parallel: 0.11 ± 0.005 | 0.089 | 0.080 |
| Quarry Sandstone | Normal: 0.085 ± 0.013 Parallel: 0.037 ± 0.012 | 0.069 | 0.075 |

Applying Eq. 3.9.1.1 for each rock type and orientation, and with a best-fit value of m of 1.7, model predictions versus the experimental data are shown in Figure 4.4.2.2. Results indicate that the modified model presented in Figure 4.4.2.2 provides a substantially improved prediction of the experimental data (compared to the Boving and Grathwohl (2001) model as shown in Figure A.1 in Appendix A), with model predictions falling within a factor of two of the experimental data. This level of accuracy is similar to the level of model accuracy previously observed for Eq. 3.9.1 with isotropic rocks (Boving and Grathwohl, 2001). The Quarry sandstone (normal orientation) is an apparent outlier, which is not readily explained. The regressed value of m in Eq. 3.9.1.1 is similar to the exponent obtained by others using Eq. 3.9.1, where previous values of m for rocks have ranged from 1.6 to 3 (Adler et al., 1994, Boving and Grathwohl, 2001; Descostes et al., 2008; Cavé et al., 2010). The model presented in Eq. 3.9.1.1 also describes the impact of bedding orientation on the effective diffusion coefficient, thereby relating rock physical properties to observed diffusion behavior.

We note here that this improved model (Eq. 3.9.1.1), with a regressed exponent value of 1.7, will provide improved estimates of the effective diffusion coefficient of contaminants through rock

matrices, *where the previous model (Figure A.1 in Appendix A) would underpredict the effective diffusion coefficient by nearly an order of magnitude*. Thus, the improved model will allow for greatly enhanced uptake and release from the rock matrix (for rock with pronounced mineral bedding) compared to current estimates of this diffusion limited process. *This will likely result a large decrease in the estimated (or, simulated) MNA timeframes in bedrock aquifers, and thus will be an important factor in management decisions in TCE-impacted bedrock aquifers.*

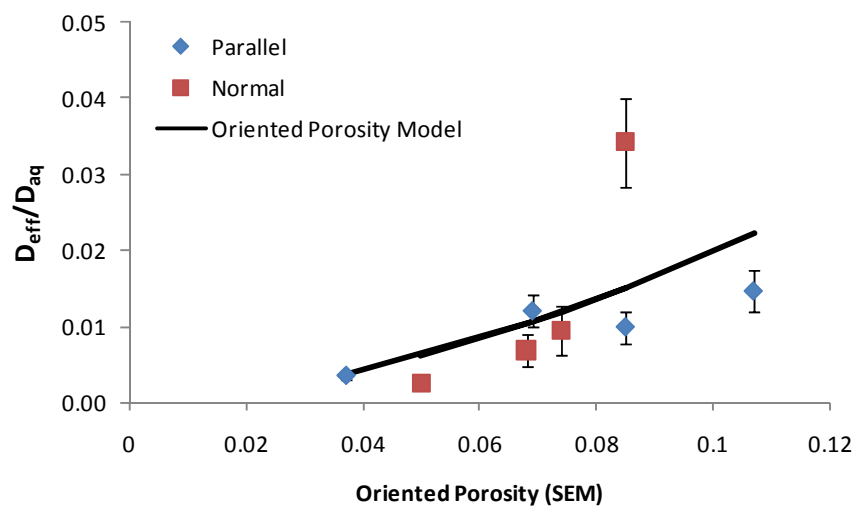


Figure 4.4.2.2. Prediction of the experimental data using the oriented porosity model (Eq. 3.9.1.1). Error bars represent the standard error.

4.4.3. TCE Coupled Diffusion and Reaction Experiments

This section discusses the results from the coupled TCE diffusion and reaction experiments performed in the stainless steel diffusion cell (Figure 3.5.3)

Results

In each experiment, the breakthrough of TCE across the rock disc and the generation of daughter products on the sink side of the cell were measured. TCE and daughter product (sum of ethane, ethene, and acetylene) breakthrough curves, and the corresponding model simulations (Eq. 3.9.2.1), for each rock type are shown in Figure 4.4.3. In some cases, trace levels of TCE and/or daughter products (<10% of the final concentrations observed in the sink of the stainless steel reaction vessel at the end of the experiments) were observed in the sink at time 0, likely due to

cross-contamination within the anaerobic chamber during preparation of the cell. Plotted and regressed data were adjusted to these baseline levels so as to avoid biasing regressed rate constants to high values. A breakdown of the daughter product generation (acetylene, ethene, and ethane) for one experiment for each rock type is provided as Supplemental Figure A.2. Measurable TCE daughter products were observed in all experiments, indicating that measurable abiotic reaction occurred for all rock types studied.

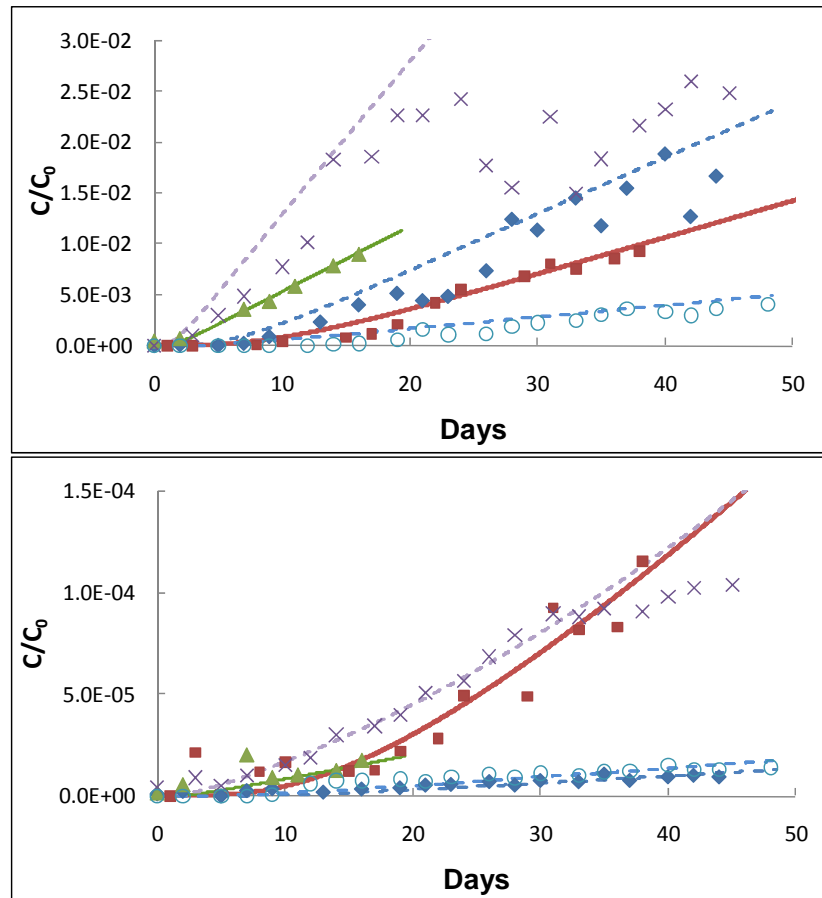


Figure 4.4.3. Comparison of experimental data (symbols) and model simulations (solid and dashed lines for Eq. 3.9.1.1) for TCE (top) and daughter products (bottom) for each rock type. Molar units are used. Both TCE and daughters are plotted as a function of the initial molar TCE concentration in the source side of the diffusion cell. As discussed for Figure 4.4.3.2 later in this section, a decrease in the porosity for the pyrite seam created a decrease in the diffusional flux over time, which is why the model over-predicts the late-time data for the pyrite seam. ♦ - Red Sandstone, ■ - Light Gray Mudstone, ▲ – Dark Gray Mudstone, X – Pyrite Seam, ○ – Pyrite Rich Mudstone.

To assess the extent to which any abiotic reactions between the cell materials and the TCE may have impacted determination of abiotic reaction rates in the rocks, daughter product generation in the cell in the absence of any rock was measured. Three no-rock experiments were performed (one with mercuric chloride, and two without). Results of this testing showed that only 15% of the generated daughter products, using the red sandstone as a comparison (which is the least reactive rock, as shown in Table 4.3.3), was attributable to interactions with the cell materials. The relative impact of the cell with respect to reaction was even less for the more reactive rock materials. In addition, data from the preliminary rock rod experiment (described in Section 3.5.2 and 4.4.1) performed in duplicate on the light gray mudstone showed that the observed bulk first order rate constant observed in a small glass reaction vessel ($9 \times 10^{-9} \text{ s}^{-1}$) was in good agreement with that observed in the metallic diffusion cell. Thus, these control experiments showed that contributions of abiotic reaction between TCE and the reaction vessel materials had a negligible impact on the results of this study.

Monitoring of TCE concentrations in the source reservoir was performed to verify that TCE mass loss (due to processes such as leakage) from the diffusion cell was less than 10%. Based on measured daughter product concentrations in the sink chamber, less than 10% of the TCE migrating through the rock reacted. Thus, the reaction did not have a significant impact of the observed TCE diffusional flux through the rock (i.e., for the length scale of these experiments, the impact of the reaction term in Eq. 3.9.2.1 for TCE was negligible).

Acetylene, ethene, and ethane were the dominant reaction products observed in the sink; no measurable chlorinated daughter products were observed in the sink, with the exception of one experiment as noted below in Table 4.4.3. While it is possible that generation of chlorinated daughter products were not observed due to diffusional retardation within the rock, the fact that TCE and ethane exhibited similar diffusional retardation (i.e., similar K_d) suggests that absence of chlorinated daughter products due to sorption was unlikely. The gaseous daughter products generated (particularly acetylene) are consistent with an abiotic reductive beta-elimination pathway, which has been shown to occur via ferrous iron minerals for TCE (Lee and Batchelor, 2003, Butler et al., 2001 & 2012). Based on this pathway and the concentrations of daughter products generated, it is estimated that less than 2% of the ferrous iron in the rocks was consumed, assuming the observed abiotic reactions were due to the presence of the ferrous iron in the rocks. Experiments performed with mercuric chloride yielded similar results to experiments performed without mercuric chloride (Table 4.4.3), verifying that the generated gases were due to abiotic processes.

Table 4.4.3. Rock TCE reaction and diffusion results. For the initial experiments performed on the dark gray mudstone and pyrite seam, only the steady state linear portion of the curve (prior to the apparent decrease in diffusive flux) was used to regress the value of the effective diffusion coefficient and k' (Eq. 3.9.2.1 and 3.9.2.1.3). Values of k' in parentheses, or denoted by **, indicate the replicate experiments where mercuric chloride was added.

| Rock Type | Replicates | k' (s^{-1}) | D (cm^2/s) |
|-------------------------|------------|--|--|
| Red Sandstone | 4 | $1.3 \pm 0.48 \times 10^{-9}$ (8.3×10^{-10} , 1.9×10^{-9})** | $1.3 \pm 0.44 \times 10^{-7}$ |
| Light Gray Mudstone | 5* | $6.4 \pm 4.6 \times 10^{-9}$ (3.9×10^{-9} , 4.1×10^{-9})** | $6.5 \pm 2.0 \times 10^{-8}$ |
| Dark Gray Mudstone | 7 | 4.2×10^{-8} 4.0×10^{-9} 6.9×10^{-9} 4.0×10^{-8} (2 nd rock) 1.6×10^{-8} (2 nd rock)** 4.1×10^{-9} (2 nd rock)** NM (2 nd rock)** | 5.9×10^{-7} 1.2×10^{-8} 9.3×10^{-9} 1.5×10^{-7} (2 nd rock) 7.6×10^{-8} (2 nd rock) 8.4×10^{-8} (2 nd rock) NM (2 nd rock) |
| Pyrite Seam | 2 | 3.4×10^{-8} 3.9×10^{-8} | 7.9×10^{-7} 3.1×10^{-7} |
| Pyrite-Rich Mudstone*** | 3 | $1.2 \pm 0.25 \times 10^{-8}$ (1.0×10^{-8})** | $1.4 \pm 0.34 \times 10^{-8}$ |

NM = Not measurable, as no breakthrough of TCE or daughter products were observed over the 66-day test duration.

* The 5th replicate for the light gray mudstone was performed on a new rock slice. The measured value for k' for this rock slice was $4.1 \times 10^{-9} s^{-1}$.

** Experiments performed with mercuric chloride present

*** The first replicate for the pyrite-rich mudstone showed trace *cis*-1,2-dichlorethene generation, equal to approximately half the molar concentration of the sum of the daughter product (acetylene+ethene+ethane) concentration.

The ratio of the daughter products (acetylene:ethene:ethane) varied among the experiments, showing little consistency among rock types or replicates. Subsequent testing in a control experiment containing no rock but only dissolved acetylene and mercuric chloride, showed that abiotic reaction occurred between the acetylene and the cell materials, yielding ethane and ethene. Similar observations have been observed by others (Scherer et al. 2007), where acetylene was shown to degrade to ethane and ethene in the presence of aluminum foil. Thus, the extent to which acetylene further degraded to ethene and ethane due to rock minerals versus diffusion cell materials is unclear. Thus, for the purposes of this study and to eliminate the impacts of the experimental artifacts of acetylene degradation by the cell materials in our analysis of abiotic TCE degradation within the rocks, no distinction is made between these daughter products, and only the net reaction of TCE to the sum of the non-chlorinated reduced gases (acetylene + ethene + ethane) is considered for abiotic reaction within the rock.

Regressed first order bulk rate constants and effective diffusion coefficients for TCE are presented in Table 4.4.3. Replicate experiments, performed using the same rock section or on replicate sections of the same rock, indicate that the measured bulk rate constants were generally repeatable. No significant decreasing trend in k' was observed over the replicate experiments. The observed lack of decrease in TCE degradation, which occurred over periods ranging from 83 to 342 days (sum over all replicate experiments per rock slice), is consistent with the negligible fraction of ferrous iron consumption (based on TCE consumption via Fe(II)) that occurred. The exception was the dark gray mudstone. For both rock slices tested on the dark gray mudstone, the bulk first order degradation rate constant decreased by an order of magnitude between the initial experiments and the subsequent experiments. Both the initial and final regressed rate constants for each of the two slices of dark gray mudstone examined showed reasonable agreement, thus confirming that the capacity for abiotic degradation of TCE in the rock showed a substantial decrease after initial exposure to TCE. Data from the second and third experiments on the first rock slice suggest that the bulk rate constant stabilized at approximately $5 \times 10^{-9} \text{ s}^{-1}$, suggesting that this latter value was more indicative of the expected long-term and steady state degradation rate that might be expected with the dark gray mudstone.

For the red sandstone, the light gray mudstone, and the pyrite-rich mudstone, the measured effective diffusion coefficients for TCE were reasonably repeatable and showed no measurable decreasing trend for subsequent replicate experiments. However, for both the dark gray mudstone and the pyrite seam, decreases in the effective diffusion coefficient were observed over time. This was first apparent during the initial experiments for each of these rock types, where a decrease in the diffusive flux was observed as a function of the diffusive elution time. As shown in Figure 4.4.3.2, the decrease in slope during the steady-state linear portion of the curve is consistent with an effective diffusion coefficient that is decreasing over time. Subsequent experiments on the same rock slices for the dark gray mudstone and pyrite seam showed a

substantial decrease in the regressed value (Eq. 3.9.2) of the effective diffusion coefficient, consistent with the apparent decreases in observed diffusion coefficients (Figure 4.4.3.2) that occurred during the initial experiments. Experiments performed on the second slice of dark gray mudstone rock slice showed a similar decrease in the effective diffusion coefficient as the first rock slice, although the magnitude of the decrease was not as large through the first three replicates. A decrease in flux was observed towards the end of the third replicate on the second rock slice (similar to the decrease in flux shown in Figure 4.4.3.2), and no measurable diffusion (through 66 days) was observed in the final replicate for the second slice. Thus, overall, both the trend and magnitude in the decrease in effective diffusion coefficient for the second rock slice were similar to the first rock slice, although somewhat delayed for the second rock slice. Sample limitations with the pyrite seam precluded performing a similar replicate test on that rock sample.

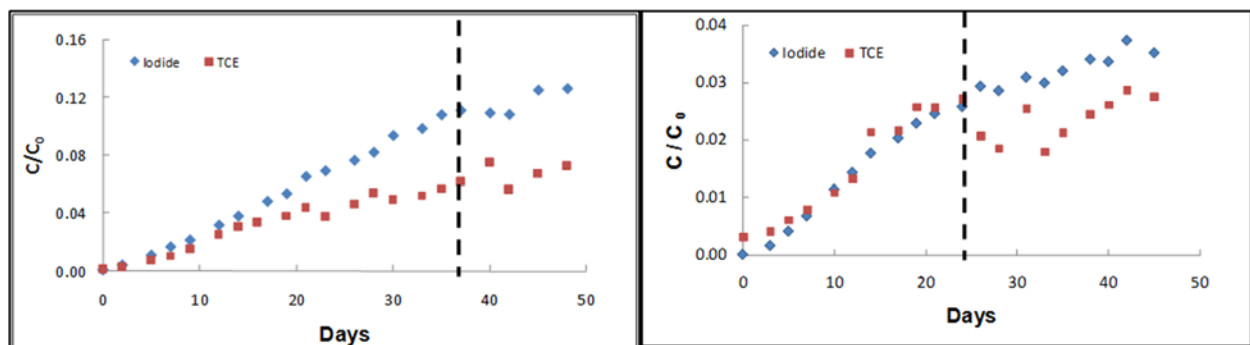


Figure 4.4.3.2. TCE and iodide concentrations on the sink side of the diffusion cell for the initial experiment performed for the dark gray mudstone (left) and the pyrite seam (right). The decrease in slope observed after 37 days for the dark gray mudstone and 25 days for the pyrite seam is due to a decrease in the effective diffusion coefficient, likely caused by a decrease in effective porosity resulting from exposure to TCE. The dashed lines indicate when the decrease in slope occurred.

The bulk rate constants (Eq. 3.9.2.3) observed in this study are (upon conversion to effective first-order rate constants) within the range observed by Darlington et al. 2008, who examined abiotic reaction in crushed sandstone samples. However, we did not detect the generation of any of the organic acids that were observed in the anaerobic study of Darlington et al; such organic acid generation has been observed in aerobic systems with TCE and pyrite present (Pham et al. 2008). In addition, the rock capacity for abiotic transformation in the study of Darlington et al. was apparently consumed within 2 to 3 months; in our current study, the capacity of the rocks to

abiotically degrade TCE was not consumed after as long as 10 months of testing at average TCE concentrations within the rock that were approximately 2 orders of magnitude greater than those used by Darlington et al. Since TCE degradation accounted for less than 2% of the ferrous iron in the tested rocks, it is not surprising to observe that the capacity for abiotic reaction did not diminish over the experimental duration. The reason for the discrepancies between our study and that of Darlington et al. is unclear. Differences in rock mineralogy may provide one possible explanation, as the ferrous minerals in the rocks used by Darlington et al. may have been less reactive than those used in the current study. Alternately, the rock crushing procedure and/or autoclaving used in the former study may provide a plausible explanation, as these processes can lead to chemical reactions with mineral surfaces (Tratnyek and Wolfe, 1993, Saruwatari et al. 2004); such reactions may have inhibited or altered the reactions with TCE.

The bulk rate constants (Eq. 3.9.2.3) measured for each rock type did not show any apparent correlation to ferrous iron content or BET surface area. We hypothesized that the abiotic reaction was controlled by the *available* ferrous iron, where we are defining the *available* ferrous iron as the fraction of the ferrous iron that is exposed to the rock porosity and readily available for reaction, as described in the experimental methods. Since much of the ferrous iron associated with the rock may not be accessible (or, less accessible) to the pore water containing TCE, use of the *available* ferrous iron should provide a more useful metric for assessing abiotic reaction rates. The SEM, EDS, and overlay images for the light gray mudstone are shown in Figure 4.4.3.3. As shown in Figure 4.4.3.4, the bulk first order rate constants (k') measured for the rocks correlate well to the available ferrous iron determined for each rock, suggesting that the available ferrous iron was a primary factor in determining the observed rates of TCE degradation observed in our study. The percentage of available ferrous iron in each rock type shown in Figure 4.4.3.4 ranged from 8 to 20% of the ferrous iron content of the rock. For the dark gray mudstone, the initially elevated values of the bulk rate constant were not used in Figure 4.4.3.4, but rather the “stabilized” values observed in the second, third, and sixth experiments.

No hydrogen sulfide was measured in the pyrite rich mudstone and light gray mudstone experiments (one experiment for each of these rock types), either on the source or sink sides of the diffusion cell. However, the detection limit for the hydrogen sulfide was approximately 0.5 mg/L. It is possible that much lower levels of hydrogen sulfide were being generated due to oxidation of ferrous minerals by TCE, but low concentration monitoring of dissolved sulfides was not performed in our studies. In addition, for experiments where ferrous iron (100 mg/L dissolved ferrous iron) was added to the source side diffusion cell, no measureable impact on TCE dechlorination was observed. It is unclear if this was due to absence of any enhancement of the mineral dechlorination reactions, insufficient migration of the ferrous iron into the rock matrix, or both.

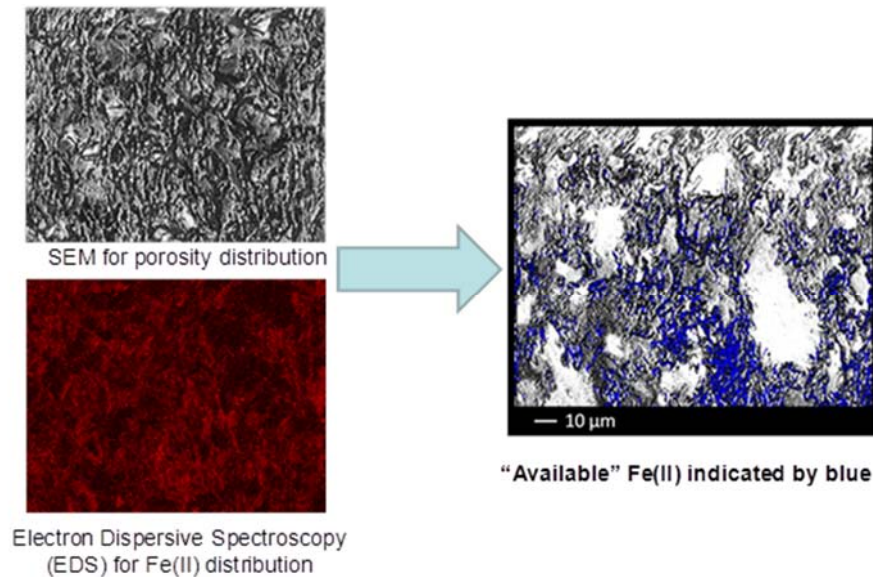


Figure 4.4.3.3. Approach used for estimating the available ferrous iron in each rock. Results for the light gray mudstone are shown as an example.

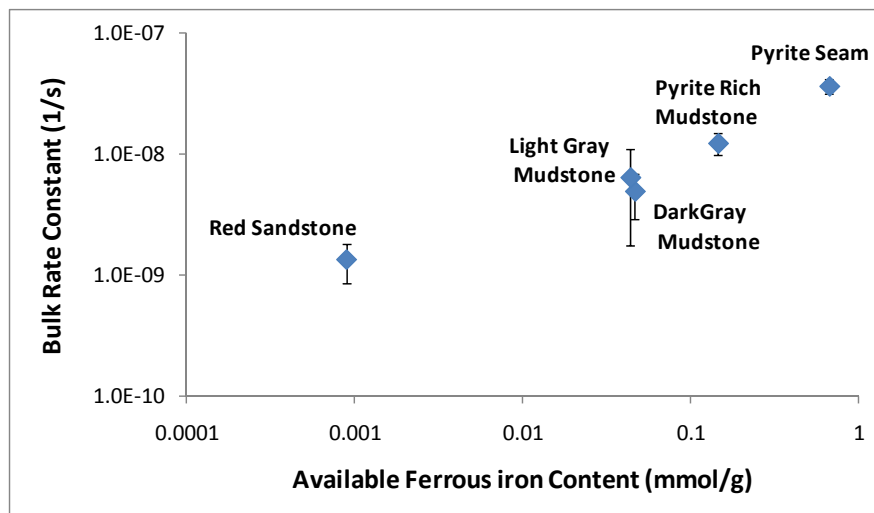


Figure 4.4.3.4. Measured bulk first order rate constants (Eq. 3.9.2) plotted as a function of the *available* ferrous iron content for each rock type. Error bars represent 95% confidence intervals. For the dark gray mudstone, initial experiments which showed an elevated reactivity were not used in this comparison, but rather bulk rate constant values that appeared to stabilize near $5 \times 10^{-9} \text{ s}^{-1}$.

Discussion

The decrease in the effective diffusion coefficient observed for the dark gray mudstone and the pyrite seam was hypothesized to be caused by the decreases in the effective porosity that occurred after exposure to TCE (20% and 50%, respectively), as porosity is the primary parameter expected to impact diffusion through the rock matrix (Schaefer et al., 2012, Boving and Grathwohl 2001). These results suggest that exposure to TCE resulted in a reduction in the effective porosity in the rocks, possibly due to oxidation of ferrous minerals and subsequent alteration of the pore structure. It is of note that decreases in the effective diffusion coefficient over time were not observed in the dark gray mudstone in our previous studies, where the rock was not exposed to TCE (Schaefer et al. 2012). This finding has potential significance for field scale processes, as the diffusive flux of TCE through rock matrices in contaminated rock aquifers may be less than expected due to a reduction in rock porosity caused by abiotic TCE degradation.

While results shown in Table 4.4.3 from the first rock slice for the dark gray mudstone suggest that the decrease in the effective diffusion coefficient (or, porosity) and the decrease in k' were potentially related (as these values both decreased substantially after the initial experiment), results from the second dark gray mudstone rock slice and the pyrite seam suggest that the decreases of the D_{eff} and k' are not related. One possibility is that the small fraction of ferrous iron consumed in the dark gray mudstone might represent reactive sites that are highly exposed to the TCE. XRD data collected before and after exposure to TCE (Table 4.4.3.1) show measurable decreases in the ferrous minerals for the rocks examined, even though the overall fraction of ferrous iron removal due to TCE oxidation was small. Exposure to the nitrate or air (brief exposure to air occurred between experiments) may have oxidized some of the ferrous minerals.

While the first order rate constants measured in this study were relatively slow, typically resulting in less than 5% removal of the TCE and having a negligible impact on TCE flux through the rock discs in the experimental diffusion cell, these rates may be significant for the time and length scales for fractured bedrock aquifers. Rock matrix diffusion length scales at the field scale are expected to be substantially longer, and diffusion times substantially greater than those observed in the laboratory, thereby causing the slow reaction rates observed in this study to have a significant impact on contaminant fate. The matrix diffusion model developed by West and Kueper (West and Kueper, 2010) suggests that the abiotic degradation rates of TCE measured in our study would likely substantially reduce monitored natural attenuation timeframes associated with back diffusion in fractured rock aquifers.

Rock matrix diffusion length scales at the field scale are expected to be substantially longer, and diffusion times substantially greater than those observed in the laboratory. The matrix diffusion

model developed by West and Kueper, 2010 suggests that the abiotic degradation rates of TCE measured in our study would likely substantially reduce monitored natural attenuation timeframes associated with back diffusion in fractured rock aquifers. To further evaluate the potential impacts of the measured abiotic reactions on field scale processes, the enhancement in mass transfer caused by a first order homogeneous chemical reaction is assessed by applying the following equation (Cussler, 1984):

$$E_{MT} = \sqrt{\frac{Dk'}{D^2}} \coth \left[\sqrt{\frac{Dk'}{D^2}} \right] \quad \text{Eq. 4.4.3.1}$$

where E_{MT} is the enhancement in TCE removal through the rock matrix due to diffusion [dimensionless] and L is the diffusion length [cm]. Eq. 3.9.2.4 provides a relative measure of the importance of reaction processes on the diffusive migration of TCE through rock, where values approaching unity indicate the impacts of reaction are negligible.

Using the light gray mudstone as the model rock (with values of D and k' taken from Table 4.4.3), the value of E_{MT} (enhancement in TCE removal through the rock matrix due to diffusion (Cussler, 1984)) for the laboratory experiments (with a diffusion length of 0.5 cm) is 1.01; this value of E_{MT} indicates that there is negligible enhancement of TCE mass removal from (or through) the rock due to reaction, and that reaction can be neglected when considering impacts on TCE diffusion. However, if a field diffusion length scale of 30 cm is considered (which would imply a 2-foot spacing between conductive fractures), the values of E_{MT} becomes 9.4, indicating that TCE mass removal from the rock is 9.4-times greater than if removal occurred via diffusion alone, and that the impacts on TCE diffusional migration are substantial. Thus, the slow abiotic reactions observed in this study may play an important role in natural attenuation processes in fractured bedrock systems. However, demonstration of these reactions *in situ*, along with measurement of their rates, is needed to verify and quantify the impacts of abiotic matrix reactions on chlorinated solvent plumes in fractured bedrock. Of particular interest is verification of the sustainability of these abiotic reaction rates in the field, where rocks have been exposed to chlorinated ethenes for decades. ***This will be discussed in Section 4.5.***

Table 4.4.3.1. Comparison of rock mineralogy before and after exposure to TCE.

| Rock Type | Mineralogy (%) | Mineralogy after TCE Exposure (%) |
|-----------------------------|--|--|
| Red Sandstone | albite (51), quartz (35), montmorillonite (6.4), muscovite (2.5), hematite (2.2), lepidocrocite (0.1), goethite (0.9), siderite (0.2), biotite (0.1) | albite (52), quartz (35), montmorillonite (4.5), muscovite (2.5), hematite (3.0), lepidocrocite (2.2), goethite (0.9) |
| Light Gray Mudstone | albite (26), kaolinite (12), chlorite (11), orthoclase (11), vermiculite (9.4), illite (8.8), clinocllore (5.9), brookite (4.4), dolomite (4.0), calcite (1.9), montmorillonite (1.6), biotite (1.6), microcline (1.3), quartz (1.2) | albite (26), illite (13), kaolinite (10), chlorite (11), orthoclase (10), vermiculite (8.5), chlinocllore (4.6), brookite (4.4), dolomite (2.6), calcite (2.2), montmorillonite (1.8), biotite (2.1), quartz (1.9), microcline (1.6) |
| Dark Gray Mudstone | albite (25), clinocllore (15), kaolinite (13), illite (15), chlorite (8.7), microcline (7.1), dolomite (5.4), quartz (3.2), orthoclase (2.7), calcite (2.6), vermiculite (1.5), biotite (1.0) | albite (25), dolomite (16), calcite (14), illite (9.5), clinocllore (9.4), chlorite (8.7), microcline (8.7), kaolinite (7.0), quartz (3.1), vermiculite (3.1), orthoclase (1.7), biotite (0.7) |
| Pyrite-Rich Mudstone | pyrite (59), dolomite (20), ankerite (9.4), anorthite (5.3), iron-mica (3.1), quartz (2.2), biotite (0.5), goethite (0.4) | pyrite (40), ankerite (20), dolomite (14), iron-mica (13), anorthite (5.7), biotite (2.6), quartz (2.3), goethite (1.9) |

Due to limited sample volume, mineralogy after exposure of the pyrite seam to TCE were not obtained

4.4.4 Oxidant Diffusion/Reaction

These experiments were performed to evaluate the migration and reactivity of chemical oxidants into the rock matrices. Both permanganate and persulfate were used as model oxidants. Tested rocks included the red sandstone, the tan sandstone, dark gray mudstone, and the light gray mudstone. For both oxidants, and with diffusion times of up to 8 weeks, no measureable breakthrough of the oxidants to the sink side of the diffusion cell was observed.

In order to quantify the extent to which, if any, the persulfate had penetrated into the rock matrices during the oxidant diffusion experiments, line scanning with a Zeiss Supra 35 VP Field Emission Scanning Electron Microscopy with an EDAX Genesis 2000 X-ray Energy Dispersive Spectrometer was performed to track the elemental changes on the cut surfaces. Results for the persulfate rocks can be seen in Figures 4.4.4 and 4.4.4.1 No elemental changes were observed in persulfate diffusion rocks, with the exception of minor elevations of carbon detected only at the rock surface. Further investigation of the carbon showed no traces around the edges of the rock leading us to believe the carbon was due to contamination from handling. We suspect that background sulfur levels prohibited detection of persulfate (or sulfate) within the rock matrix. Thus, estimates of persulfate penetration into the rock could not be attained.

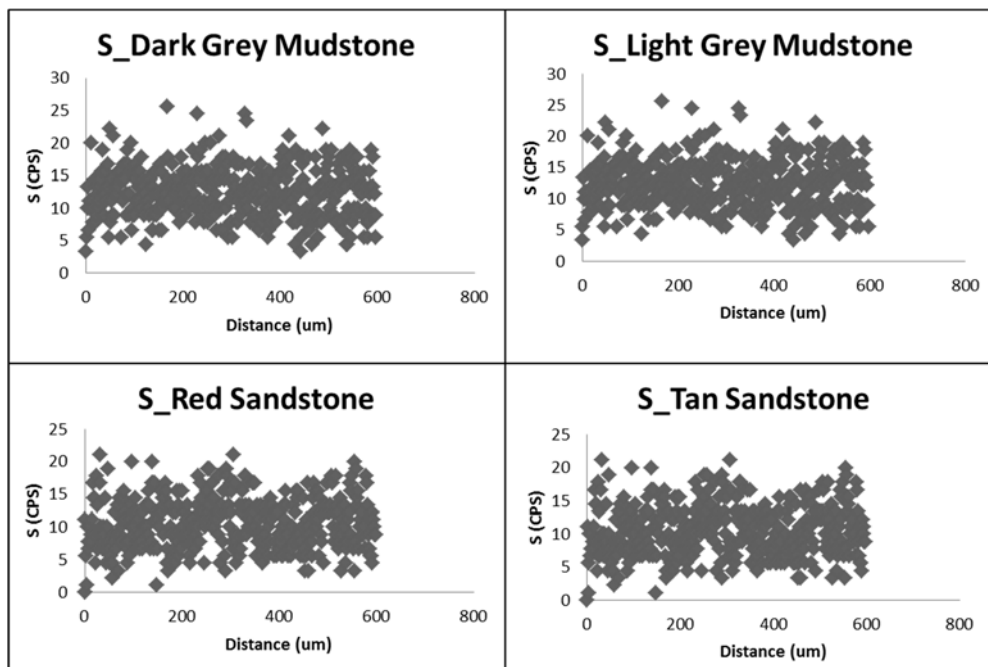


Figure 4.4.4. Sulfur Profiles of sodium persulfate diffusion in different sedimentary rocks after 7-8 weeks of exposure to a persulfate solution (2000 ppm).

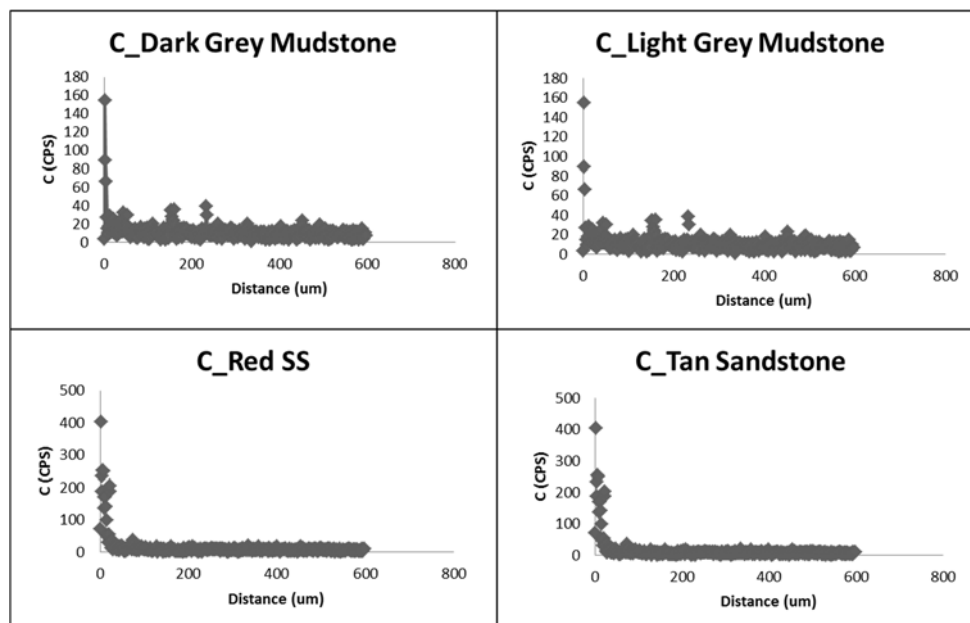


Figure 4.4.4.1 Carbon Profiles of sodium persulfate diffusion in different sedimentary rocks after 7-8 weeks of exposure to a persulfate solution (2000 ppm).

For permanganate (KMnO_4), SEM-EDS line scanning results obtained from cross sections of all rock types showed that there was a Mn concentration gradient from the exposed surface into the rock matrix along the direction of Mn diffusion (Figure 4.4.4.2). Overall, the permanganate penetration distance varied from ~ 50 to $400 \mu\text{m}$ for the different rock types. These diffusion profiles were fitted to obtain D_{obs} values. Table 4.4.4.1 shows a summary of the regressed D_{obs} values for the 4 rock types (in duplicate), along with the calculated values of $D_{\text{obs,cal}}$ (based on Eqs. 3.9.3.2 and 3.9.3.3) and effective diffusion coefficient for each rock type. Measured D_{obs} values are generally on the order of 10^5 -times less than the previously measured effective diffusion coefficients (measured for TCE or iodide) through the rock (Schaefer et al., 2012; Schaefer et al., 2013). The calculated $D_{\text{obs,cal}}$ values are on the same order of magnitude as the measured D_{obs} values. Considering the extremely small diffusion distances into the rocks, and the natural heterogeneity of the rock matrices, this agreement is reasonable and suggests that the slow diffusional migration of the oxidant into the rock is greatly hindered by the reaction between permanganate and naturally occurring reductants within the rocks. Thus, the reaction between permanganate and the rock matrix is the primary cause for the very low values of D_{obs} . Based on the limited penetration distance into the rock and the low value of D_{obs} , it is unlikely that application of chemical oxidants will provide treatment for target contaminants residing at distances greater than a few hundred microns into the rock. The exception may be rocks that have extremely low oxidant demand (much less than those measured for the rocks used in this

study) and longer oxidant persistence (much greater than the 2 month period of this study), which would allow for a more rapid migration of oxidant into the rock.

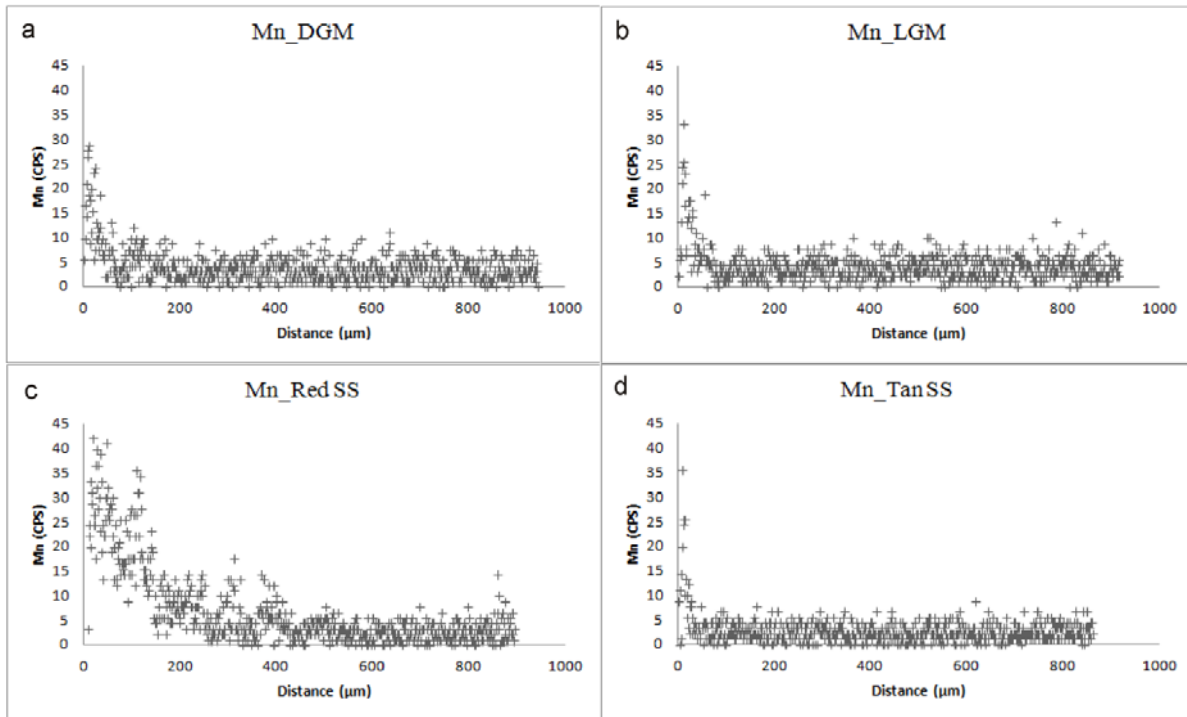


Figure 4.4.4.2 Manganese profiles of permanganate diffusion in different sedimentary rocks after 7-8 weeks of exposure to a permanganate solution (2000 ppm). These profiles were obtained from cross sections perpendicular to the permanganate-exposed rock surface using SEM-EDS line scanning. The left edge of a rock slice corresponds to distance of zero. CPS: counts per second.

Table 4.4.4.1. Permanganate D_{obs} values and effective diffusion coefficients for different rock types. Measured (D_{obs}) and calculated ($D_{\text{obs,cal}}$) values were obtained from duplicate experiments based on Eqs. 3.9.3 – 3.9.3.3. 95% confidence intervals are shown. \pm values represent the standard error.

| Rock type | D_{obs} (cm^2/s) | $D_{\text{obs,cal}}$ (cm^2/s) | Effective diffusion coefficient (cm^2/s) |
|---------------------|---|---|--|
| Dark gray mudstone | $9.5 \pm 5.2 \times 10^{-13}$ | 1.1×10^{-12} | $2.3 \pm 1.4 \times 10^{-7}$ |
| | $1.4 \pm 0.6 \times 10^{-12}$ | | |
| Light gray mudstone | $7.1 \pm 6.6 \times 10^{-13}$ | 1.3×10^{-12} | $2.6 \pm 1.1 \times 10^{-7}$ |
| | $6.2 \pm 5.4 \times 10^{-13}$ | | |
| Red sandstone | $3.2 \pm 0.01 \times 10^{-12}$ | 7.1×10^{-12} | $4.2 \pm 3.4 \times 10^{-7}$ |
| | $1.3 \pm 0.5 \times 10^{-11}$ | | |
| Tan sandstone | $5.3 \pm 3.2 \times 10^{-13}$ | 4.4×10^{-12} | $2.3 \pm 1.0 \times 10^{-7}$ |
| | $1.1 \pm 0.4 \times 10^{-12}$ | | |

To determine the extent to which exposure to the oxidant may have impacted solute diffusion through the rocks, an iodide tracer on the oxidant impacted rocks was conducted. Results of the iodide tracer testing are provided in Table 4.4.4.2. An increase in iodide diffusion was observed over the course of several weeks. Average diffusion coefficients are of the same order as the prior iodide diffusion bedrock orientation experiments (Section 4.4.2) indicating that no retardation had occurred, and therefore persulfate has a negligible impact on diffusion.

Table 4.4.4.2. D_{eff} values prior to oxidant exposure compared to D_{eff} after exposure to oxidant (Schaefer et al., 2012; Schaefer et al., 2013).

| Rock type | D_{eff} (prior to oxidant) (cm^2/s) | D_{eff} (post permanganate) (cm^2/s) | D_{eff} (post persulfate) (cm^2/s) |
|---------------------|--|---|---|
| Light gray mudstone | 1.3×10^{-7} | 1.1×10^{-7} | 7.8×10^{-8} |
| | | 1.1×10^{-7} | 6.4×10^{-7} |
| | | | 6.4×10^{-7} |
| Red sandstone | 2.0×10^{-7} | 1.2×10^{-7} | 4.3×10^{-7} |
| | | 5.5×10^{-7} | 3.5×10^{-7} |
| Tan sandstone | 1.6×10^{-7} | 4.0×10^{-8} | 2.1×10^{-7} |
| | | 1.0×10^{-7} | 1.5×10^{-7} |
| | | 1.6×10^{-7} | |

Our data further illustrated that over the course of permanganate diffusion, permanganate was reduced by naturally present chemical reductants within the rocks. SEM-EDS line scanning results revealed that manganese (Figure 4.4.4.2) and carbon (Figure 4.4.4.3) exhibited a similar diffusion profile, both of which showed a decreased concentration with penetration distance into the rock matrix. This Mn and C coupling was further confirmed by SEM-EDS elemental maps obtained from a cross section of the red sandstone (Figure 4.4.4.4), where the spatial distribution of Mn was approximately correlated with carbon, but not with any other elements. However, in this two-dimensional map, the correspondence between Mn and C was not exact. In fact, Mn was enriched near the upper left corner of the image, whereas C was enriched in the lower left.

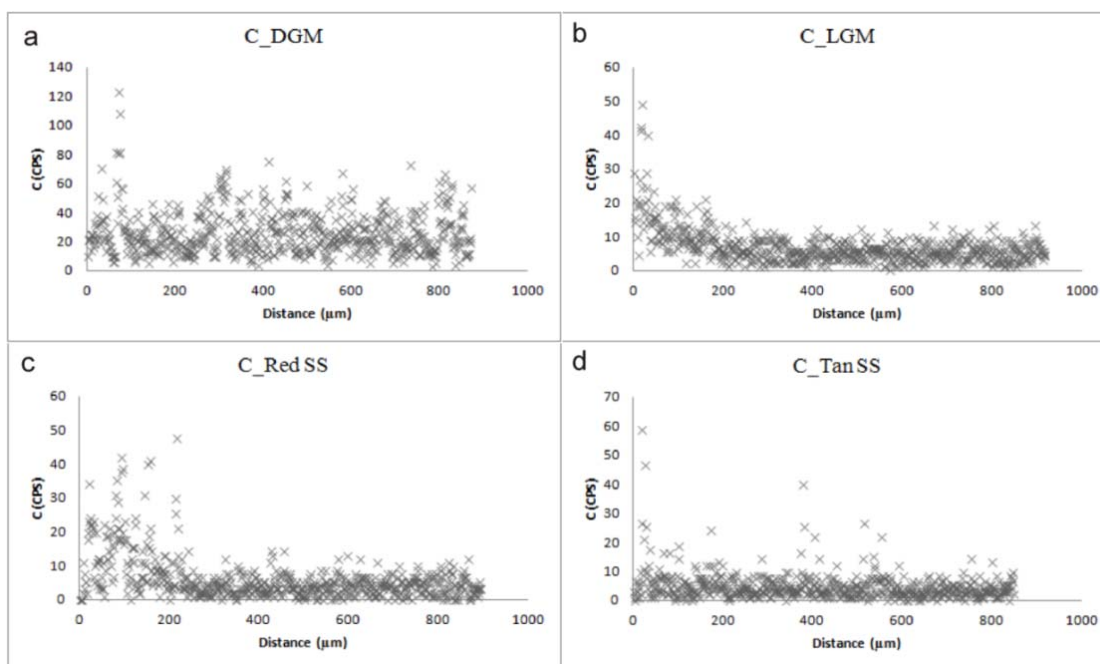


Figure 4.4.4.3. Carbon profiles in different sedimentary rocks after 7-8 weeks of exposure to a permanganate solution (2000 ppm). These profiles are similar to the Mn profiles.

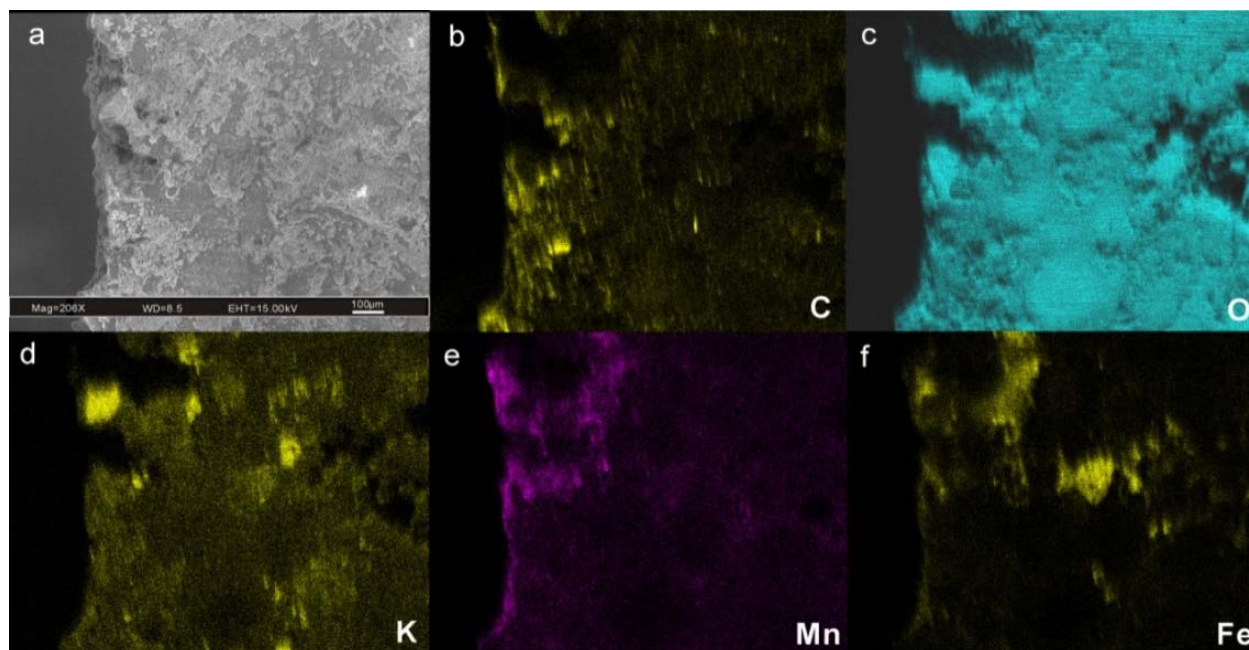


Figure 4.4.4.4. SEM-EDS elemental maps showing the distributions of C, O, K, Mn, and Fe, as well as a secondary image for the red sandstone sample. The brighter areas on the photos indicate higher elemental concentrations. These maps do not distinguish different forms of elements (such as organic or inorganic carbon) or different oxidation states and only represent total elemental concentrations.

It was unexpected to observe a similar, rather than an opposite, diffusion profile between the Mn (as an oxidant) and C (as a reductant), especially in the light gray mudstone and red sandstone (Figure 4.4.4.2). No such carbon enrichment was observed in a control sample (which was not exposed to oxidant), therefore ruling out the possibility of carbon contamination from sample preparation. We speculate that the C profile may be a result of carbon re-distribution. Once organic carbon was oxidized by permanganate, the resulting inorganic carbon may diffuse from within the rock matrix toward the surface. Because the permanganate diffusion process may have wetted the rock and opened rock pores on the reservoir side, inorganic carbon may have diffused towards the permanganate chamber much faster than the opposite direction (e.g., towards the sink side) and may have accumulated near that surface. This process of organic carbon oxidation followed by re-distribution of the resulting inorganic carbon may have accounted for the enrichment of inorganic carbon near the permanganate-exposed surface of the rocks, where Mn enrichment was also observed. This inorganic carbon redistribution hypothesis would explain the correlation between the C and Mn elemental maps (Figure 4.4.4.4), where the correspondence between the Mn and C elemental distribution was not exact but with some offset. Although not

directly verified, this carbon enrichment on the rock surface may be either adsorbed or associated with carbonates. For the dark gray mudstone and the tan sandstone, carbon enrichment is less obvious (Fig. 4.4.4.2), possibly because there was little inorganic carbon redistribution. If carbon only changes the form (from organic carbon to inorganic carbon) without redistribution, local enrichment near rock surface is not expected.

The coupling between Mn and inorganic C was also consistent with the positive correlation between permanganate oxidant demand and TOC (Table 4.3.4), where more permanganate reduction would oxidize more TOC and produce more inorganic carbon. This correspondence of Mn and C diffusion profile and the positive correlation between the natural oxidant demand values and TOC strongly suggest that organic matter served as a chemical reductant to reduce permanganate (Mn^{7+}) to $\text{Mn}^{2+}/\text{Mn}^{4+}$ (e.g., birnessite). These results suggest that the reaction between permanganate and TOC was responsible for the small travel distance of permanganate into rock matrix. This conclusion is consistent with previous studies where organic matter in sedimentary rock was found as the primary component in the reaction with permanganate (Hønning et al., 2007a; Hønning et al., 2007b).

A previous study (Hartog et al., 2002) suggested that the relative importance of organic matter vs. ferrous iron (in pyrite and siderite) in reducing molecular oxygen was dependent on sediment grain size. The oxidation of sedimentary organic matter (SOM) in a fine grain size fraction was less important than the oxidation of pyrite and siderite, while SOM oxidation was very important in a coarse grain size fraction. The authors ascribed this difference to a decreased reactivity of sedimentary organic matter in the fine fractions as a result of physical protection through sorption and complexation of organic matter by clay minerals or to a higher degree of mineralization of the original organic matter during diagenesis. Our results suggest that TOC, not ferrous iron, was responsible for natural oxidant demand. The higher reactivity of TOC than ferrous iron in our samples could be due to two reasons: 1) Fe(II) is largely associated with non-reactive clay minerals (e.g., chlorite), not with reactive pyrite and siderite; 2) TOC is not protected by clay minerals and may be readily accessible to permanganate. Protection of organic matter by clay minerals is largely through sorption into the interlayer space of expandable clays such as smectite (Kennedy et al., 2002), but in our samples, there is little smectite-like minerals, even in the mudstones.

Results of the iodide tracer testing performed on the permanganate- and persulfate-exposed rocks are provided in Table 4.4.4.1. Results are presented for only three rock types, as the dark gray mudstone was not available for this testing. Iodide tracer results show that exposure to either of the oxidants for 2 months did not result in a significant (greater than approximately a factor of 2) decrease in the measured D_{eff} . Thus, oxidant exposure and any accumulation of Mn minerals near the surface of the rock (which were visually observed for the permanganate treated rocks)

did not have a substantial impact on diffusional flux through the rock. This finding suggests that precipitation of Mn minerals along the fracture surface following application of *in situ* chemical oxidation, or any other impacts on the rock porosity due to exposure of these strong oxidants, likely will not have a large impact on mitigating the back-diffusion of chlorinated ethene contaminants emanating from the rock matrix, at least after a 2 month exposure to the oxidant.

Mineralogical changes as a result of permanganate reaction varied across different rock types. Major minerals, such as quartz (<71.8%), kaolinite (<20.4%), and albite (10.8-38.8%), were dominant in all of these rock samples (Table 4.4.4.3). No distinct Fe(II)-containing minerals were detected, and it is likely that Fe(II) measured by chemical extraction resides within chlorite and muscovite. Abiotic reduction of permanganate resulted in precipitation of various Mn minerals on the Mn-exposed side of the rocks, including birnessite (2.8-7.5%) and manganocalcite (<2.9%) (Table 4.4.4.3). SEM observations confirmed these results and revealed various morphologies/sizes and composition of these precipitates (Figure 4.4.4.3). Unlike the non-permanganate-reacted rocks most of these Mn minerals were present as rod-like particles on rock surfaces with various elements, such as O, C, Mn, Si, and Al (Supplemental Figure A.3). Si and Al were likely derived from surrounding silicate minerals. This is consistent with previous studies where semi-amorphous potassium-rich birnessite and MnO₂(s) particles were identified during TCE remediation process using permanganate (Crimi and Siegrist, 2004; Li and Schwartz, 2004; Loomer et al., 2010; Zhang and Schwartz, 2000).

Table 4.4.4.3 Mineralogy of permanganate reacted surfaces of sedimentary rocks.

| Minerals | Formula | Dark gray mudstone (%) | Light gray mudstone (%) | Red Sandstone (%) | Tan Sandstone (%) |
|----------------|---|------------------------|-------------------------|-------------------|-------------------|
| Quartz | SiO ₂ | 8.2 | | 29.1 | 69.8 |
| Albite | Na(AlSi ₃ O ₈) | 21.2 | 10.8 | 38.8 | 23.6 |
| Kaolinite | Al ₂ Si ₂ O ₅ (OH) ₄ | 10.2 | 20.4 | 9.6 | |
| Amesite | (Mg ₂ Al)(AlSi ₃ O ₅ (OH) ₄) | | 38.3 | | |
| Microcline | KAlSi ₃ O ₈ | 10.3 | | | |
| Calcite | CaCO ₃ | 4.8 | | | |
| Dolomite | CaMg(CO ₃) ₂ | 15.8 | | | |
| Anorthite | CaAl ₂ Si ₂ O ₈ | 13.9 | | | |
| Muscovite | KAl ₂ (Si ₃ Al)O ₁₀ (OH) ₂ | 9.9 | | 14.9 | |
| Chlorite | Mg ₂ Al ₃ (Si ₃ Al)O ₁₀ (OH) ₈ | | 23.0 | | |
| Birnessite | (K,Na) ₄ Mn ₁₄ O ₂₇ (H ₂ O) ₉ | 2.8 | 7.5 | 7.5 | |
| Manganocalcite | (Ca,Mn)CO ₃ | 2.9 | | | |
| Ramsdellite | MnO ₂ | | | | 6.6 |

Our results show that Mn mineralogy resulting from abiotic reduction of permanganate depended on the rock type and mineralogy. For example, manganocalcite ((Ca,Mn)CO₃) was only detected in the dark gray mudstone, where TOC content was the highest among the four rock types, and calcite (CaCO₃) was present in the original rock. This result suggests that TOC may be readily available in the dark gray mudstone to reduce permanganate and to form manganocalcite. The reduced Mn²⁺ (ionic radius $r=0.80 \text{ \AA}$) may have substituted for Ca²⁺ ($r=0.99 \text{ \AA}$) within the calcite structure due to their similar charge and ionic radius (Gunasekaran and Anbalagan, 2008; Pingitore, 1978). The formation of the lowest Mn oxidation state (2+) in manganocalcite would increase the amount of permanganate consumption, and may have partially accounted for its highest oxidant demand in this rock.

The nature of these Mn mineral precipitates could have important implications for the development of strategies for controlling the stability of these reaction products because settling of these Mn solid particles has a potential to deposit in the subsurface and to impact the flow regime in and around permanganate injection points. However, our iodide tracer testing results indicated that within 2 months of permanganate exposure, the accumulation of Mn minerals near

the surface of the rock, regardless the nature of these minerals, did not have a notable impact on diffusional flux through the rock. Nonetheless, this impact cannot be ruled out if the rocks are exposed to permanganate for a prolonged time. Also, Mn mineral accumulation may have a more pronounced effect in hydraulically conductive fractures.

4.5 Diffusion Experiments – Rock Collected *Within* the TCE Plume

4.5.1 Groundwater characterization

Discrete groundwater sampling during the second phase of coring activities confirmed that TCE was present in the adjacent conductive fractures (203, 463, and 24800 µg/L in the fractures at 49, 53, and 83 feet below land surface, respectively). Potential TCE abiotic degradation products, including ethene, ethane, and acetylene (Butler and Hayes, 1999; Weerasooriya and Dharmasena, 2001; Lee and Batchelor, 2002; O’Loughlin and Burris, 2003; Liang et al., 2009; He et al., 2010), also were observed at trace (<5 µg/L) concentrations at these discrete intervals.

4.5.2 Rock characterization

Rock mineralogy, total and ferrous iron content, and porosity for the mudstone collected from each depth interval are summarized in Table 4.3.1. Rock from each of the 3 intervals was, as expected based on visual observation, similar in many of the characterized properties. However, an increase in ferrous iron content and slight decrease in porosity was observed with depth. Measured porosities were in the range typically observed for mudstones (Yang and Aplin, 2010; Schaefer et al., 2012); iron contents also were within the range observed for mudstones (Durrance et al., 1978; Macquaker et al., 1997; Schaefer et al., 2013).

4.5.2- Reaction Cell Experiments-TCE impacted Rocks

For all rocks tested in the 40 mL vials, abiotic daughter products were observed; no daughter products were observed in the controls. Abiotic daughter products included ethane, ethene, propane, and occasionally trace levels of acetylene. For the un-spiked samples, the approximate molar ratio of ethane:ethene:propane for the two shallow zones was 4:1:1. For the deepest interval, no propane was observed and the ethane:ethene ratio was approximately 1:1. It is unclear why the apparent abiotic TCE degradation products differed in the deepest interval, but the increased ferrous iron content and/or the increased TCE concentrations associated with the deepest interval may have contributed to the difference.

Of these compounds, the generation of propane (in both the un-spiked samples and spiked samples discussed in Section 4.5.3) was the most surprising. In our previous studies with these rocks, using core collected from outside the historic TCE plume, ethene, ethane, and acetylene were identified as the primary abiotic daughter products (Section 4.4.3). The generation of propane, but not acetylene, from these rock cores was unexpected, although propane and longer chain hydrocarbons have been observed as trace products of abiotic degradation of chlorinated ethenes using zero-valent iron (Arnold and Roberts, 2000; Liu et al., 2005). It has been suggested that these higher coupling products proceed from further reduction of either ethene or acetylene on zero-valent iron (Schrack et al., 2002; Elsner et al., 2008; Audi-Miró et al., 2013); hitherto observations of these higher coupling products with ferrous minerals have not been reported. Trace levels of propane, upon re-examination of the groundwater data, was observed at each of the sampling intervals (2.4, 2.4, and 0.3 $\mu\text{g/L}$ in the fractures at 49, 53, and 83 feet below land surface, respectively). The difference in results between the rock core collected from *outside* compared to *within* the TCE plume with respect to propane generation is not readily explained, but may be related to long-term exposure of the rock to TCE.

TCE was detected in the un-spiked vials, but concentrations were near or below the quantifiable detection limit (100 $\mu\text{g/L}$), indicating that trace levels of TCE were present, but not readily quantifiable via the analytical method. This TCE was present due to desorption/diffusion from the rocks, which were exposed to TCE *in situ* for decades. The measured increase in abiotic daughter products at day 22 in the un-spiked vials is shown in Figure 4.5.2 for each depth interval, where the sum of abiotic daughter products is presented as the molar equivalent of TCE degraded (1 mol TCE per mole of ethene, ethane, or acetylene; 1.5 mol of TCE per mole of propane). With the exception of the 49 ft depth interval, a decreasing trend in TCE daughter product is observed for the unspiked samples moving inwards from the fracture interface into the rock matrix; this suggests that the TCE degradation reactions were generally greater near the fracture faces, perhaps due to the presence of the TCE source in the conductive fractures. As the TCE source for these rocks were at the fracture interfaces, this result is not unexpected. The rocks' capacity for TCE dechlorination as a function of distance from the fracture interface is further explored and discussed in Section 4.5.3.

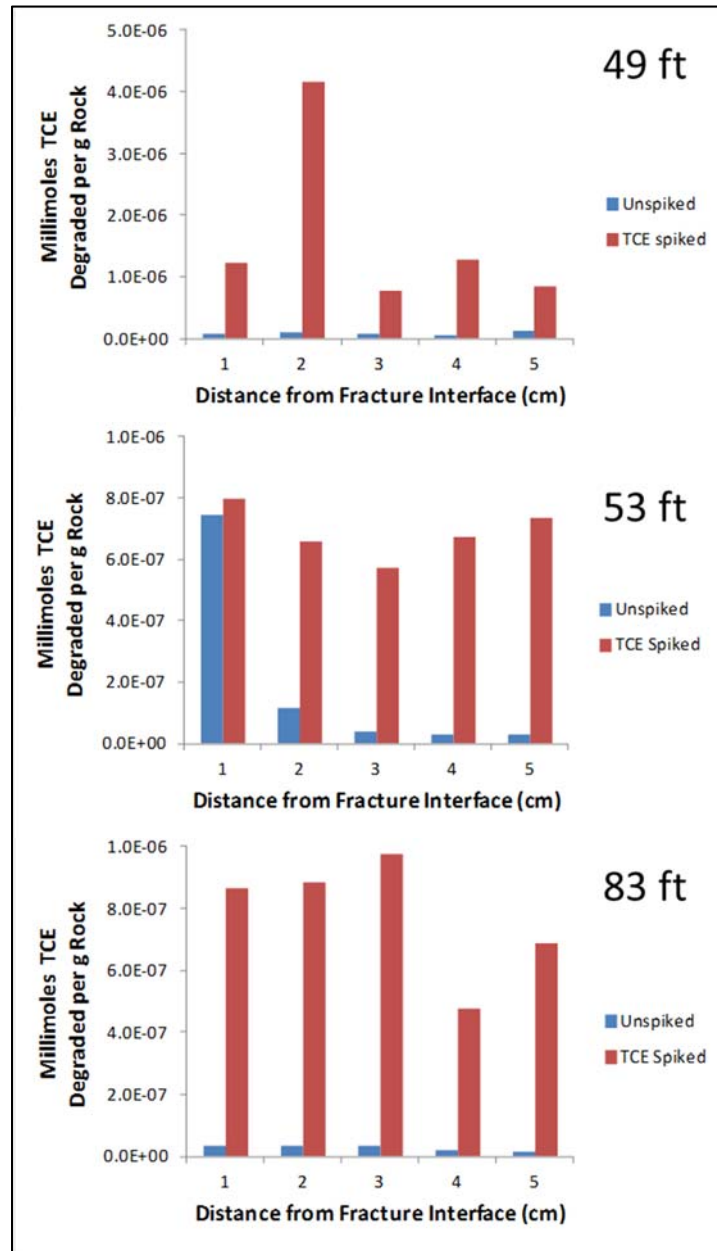


Figure 4.5.2. Comparison of observed abiotic degradation (calculated based on daughter product generation) of TCE in TCE-spiked and un-spiked samples for each of the 3 depths after 22 days of laboratory incubation. Results are shown for each of the 5 distances from the fracture face for each depth.

No increasing trends in daughter product concentrations were observed for the un-spiked samples between 22 and 49 d, with the exception of the 53 ft depth interval, where a 21% increase was observed at 49 d. We note that daughter products in the un-spiked samples were likely due to continued abiotic reaction with the TCE in the system and/or the back-diffusion of abiotic reaction products from the rock matrix (from abiotic TCE dechlorination reactions that had occurred *in situ*); the ethene in the un-spiked samples also could have been generated via biotic reaction *in situ*. Thus, results from the unspiked samples alone could not be used to determine if abiotic reaction between the rock matrix and TCE was ongoing, or was the result of reactions that had occurred prior to sample collection.

4.5.3 Reaction Cell Experiments-Rock Core spiked with TCE

For all rocks tested, similar to the un-spiked samples described in Section 4.5.2, abiotic daughter products were generated including ethane, ethene, propane, and occasionally trace levels of acetylene. For the TCE spiked samples, the ethane:ethene:propane molar ratio was approximately the same for each depth interval at 1:1:0.3. The difference in the daughter product molar ratios between the spiked and unspiked (see Section 4.5.2) samples suggests that time of exposure to TCE (along with mineralogy) may play a role in the abiotic degradation products. No decrease in TCE concentration was observed in the spiked samples, as the generation of abiotic daughter products accounted for less than 1% of the TCE mass in the bottles.

Results presented in Figure 4.5.2 show that no trend was observed for the spiked samples as a function of distance from the fracture face, indicating that rock reactivity with respect to TCE degradation was not a function of distance within the first several centimeters of the rock. ***This result is of note, indicating that the abiotic dechlorination activity of rock at the fracture-matrix interface is not measurably impacted due to any changes in mineralogy (i.e., oxidation) that may have occurred over time at the fracture-matrix interface.*** It is possible, however, that the length scale with respect to mineralogical changes that would impact dechlorination activity are much smaller (e.g., microns) compared to the centimeter length scale of the rock slices.

To determine if abiotic dechlorination reactions with TCE were still occurring in the rock matrices (or, if the rock still retained capacity for abiotic dechlorination despite exposure to TCE for decades), daughter product generation in the TCE-spiked samples was compared to the un-spiked samples. Figure 4.5.2 compares daughter product generation in the spiked versus un-spiked samples at 22 d. In nearly every case, the total moles of TCE degraded (estimated by the molar sum of the ethene, ethane, and propane) is substantially greater in the spiked samples than in the un-spiked samples. ***The results shown in Figure 4.5.2 indicate that, despite decades of exposure to TCE, the rock has maintained measureable abiotic reactivity with respect to TCE***

dechlorination, and that abiotic dechlorination reactions within the rock likely are occurring in situ. It is also of note that the first rock slice for each depth interval had only the natural fracture face exposed to the TCE solution, whereas all other slices had a cut face exposed. These data indicate that exposure of the cut face to the TCE did not result in any artificially-enhanced TCE degradation (i.e., by exposing fresh mineral surfaces).

The daughter products observed, particularly the ethane, propane, and acetylene, are consistent with an abiotic degradation pathway; these daughter products account for the majority of the TCE degradation. Ethene can be an abiotic or biotic daughter product. It is also noted that ethane can be a biotic daughter product of ethene under anaerobic conditions, but this process is not common (de Bruin et al., 1992; Koene-Cottaar and Schraa, 1998; Schaefer et al., 2009, 2010). Furthermore, we have shown in our previous work using this rock type (Schaefer et al., 2013; Section 4.4.3) that the rate of daughter product generation was not impacted by the presence of the microbial inhibitor mercuric chloride, which also is consistent with abiotic degradation processes.

The TCE-spiked samples also were monitored for organic acids (i.e., glycolate, lactate, acetate, formate), as generation of these acids have been observed by others (Darlington et al., 2013). However, no generation of organic acids was observed. There also was no observable generation of *cis*-1,2-dichlorethene or vinyl chloride (potential biotic degradation products), but the 200 µg/L detection limits for these compounds were much greater than the detection limits for the reduced gases.

Figure 4.5.3 shows the cumulative TCE degradation for each depth interval (average value over all 5 slices per interval) in the spiked samples through 118 days. No observable decrease in reactivity (i.e., in the first-order rate constant) was observed during the study. Considering the rock has measureable reactivity with TCE after decades of exposure to TCE, these results appear reasonable. It also is noted that, given the rates of TCE reaction observed in this study, the ferrous content of the rock, and the TCE concentrations in spiked samples, less than 0.01% of the ferrous iron mass in each sample was consumed during the laboratory experiment (assuming 6 moles of ferrous iron consumed per mole of TCE). Given that the TCE concentrations in the laboratory were an order of magnitude greater than those observed in the field, along with this low ferrous consumption, this result suggests that the rock matrix will retain its capacity to reduce TCE for many decades.

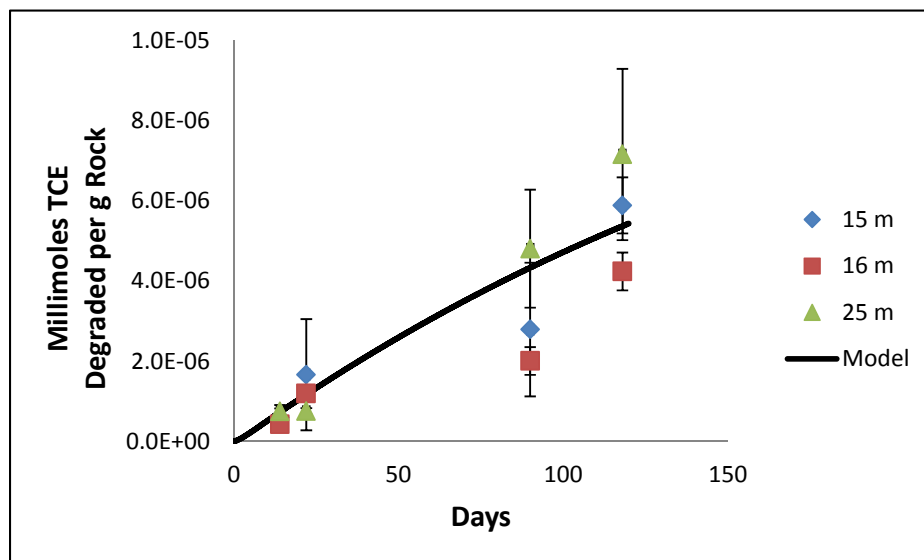


Figure 4.5.3. Abiotic TCE degradation in the TCE-spiked samples. Average values for the five rock slices for each depth are shown for each sampling time (i.e., days 14, 22, 90, and 118). Error bars represent the 95% confidence intervals among the 5 rock slices at each depth. The model simulation, using the average regressed first-order rate constant value of $1.3 \times 10^{-8} \text{ s}^{-1}$, is shown.

Using our coupled diffusion and first order reaction model for TCE in rock matrices (Section 3.9.2.1), along with the previously measured diffusion coefficient of TCE through the dark gray mudstone ($1.5 \times 10^{-7} \text{ cm}^2 \text{ s}^{-1}$), bulk first-order TCE abiotic degradation rate constants (defined as the first order rate constant multiplied by the linear sorption coefficient and the rock density) were regressed to the measured daughter product generation in the bottles. The regressed first order bulk rate constant, averaged over all intervals for the spiked samples, was $1.3 \pm 0.2 \times 10^{-8} \text{ s}^{-1}$. This rate constant described the transformation of TCE to the sum of the reduced gases (ethene + ethane + acetylene + propane). This value is in very good agreement with the bulk rate constant measured for the mudstones in rock core that had been collected from a location outside of the TCE plume ($\sim 10^{-8} \text{ s}^{-1}$). Thus, the impacts of long-term exposure to TCE do not appear to have a substantial impact on the observed dechlorination rate of TCE in the rock matrix. The bulk first order rate constant reported herein also is on the same order of magnitude as first order rate constants determined by Ferrey et al. (2004) for *cis*-1,2-dichloroethene in aquifer sediments containing magnetite.

Using our previously published diffusion and reaction model for TCE through rock matrices (Schaefer et al., 2013; Section 3.9.2.1), and applying the finite difference model to diffusion into

30 cm of rock matrix ($\Delta x = 5$ cm, $\Delta t = 1 \times 10^5$ s), a first order bulk rate constant of $1.3 \times 10^{-8} \text{ s}^{-1}$ results in an approximate 10-fold decrease in TCE mass within the rock matrix over a 10 year period compared to the simulated case where no reaction occurs. ***Thus, these abiotic reactions can have a significant impact on TCE uptake and release in rock matrices, and ultimately on back diffusion processes. Furthermore, as the abiotic TCE degradation rates measured in this study appear to be sustainable even after prolonged exposure to TCE, these abiotic processes will likely play a significant role in the long term in situ attenuation processes of the bedrock system.***

4.6 Contaminant Profiles in Rock Matrices

For the NAWC and Calf Pasture Point sites, measurement of the TCE concentration profiles into the rock (as described in Section 3.7) showed that the TCE concentrations were below the analytical detection limit of $78 \text{ } \mu\text{g/kg}$. We recognize that employing a more rigorous extraction technique and using an increased solid:liquid ratio for the extraction may have resulted in measurable detections of TCE within these rock matrices. However, the fact that both of these rock types exhibited substantial abiotic dechlorination activity coupled with the absence of elevated TCE concentrations in bedrock was at least consistent with the hypothesis that these abiotic dechlorination reactions may be limiting contaminant storage in the rocks

The results from the rock cores collected at Loring AFB and Edwards AFB were more insightful than those collected at NAWC and Calf Pasture Point. As shown in Figure 4.6, PCE concentrations going inwards from the fracture interface showed no increasing or decreasing trend in the Edwards AFB granite. In contrast, PCE concentration decrease rapidly (within a centimeter) going inwards from the fracture interface in the Loring AFB limestone. In the absence of any dechlorination reaction, and assuming a constant PCE source in the fractures that has persisted for decades (which is the case for both Loring and Edwards), the diffusion profile observed in Figure 4.6 for Edwards AFB would be expected for both sites. One explanation for the Loring AFB PCE profile in the rock matrix, based on our coupled diffusion/reaction model, is that abiotic dechlorination of PCE has limited the diffusional uptake of PCE into the rock matrix.

Figure 4.6.1 shows the millimoles of TCE degraded per day per g of rock for both the Edwards AFB and Loring AFB rocks; these degradation rates were based on crushed rock samples in batch systems, as described in Section 3.7.2. Results show that the rate of abiotic dechlorination activity in the Loring AFB rock is approximately an order of magnitude greater than in the Edwards AFB rock. This enhanced rate of abiotic reaction in the Loring AFB rock provides a plausible explanation for the low uptake of PCE in the rock matrix compared to the matrix

uptake at Edwards AFB (Figure 4.6). It is of note that the rates of reaction observed for Loring AFB are approximately 20-times less than those observed for the mudstones at NAWC. We believe that the PCE uptake in the Loring rock is so much less than the Edwards rock primarily because of the abiotic dechlorination activity of the Loring rock.

While the comparisons shown in Figures 4.6 and 4.6.1 were performed for only two bedrock types, they serve as an illustrative example of how abiotic dechlorination reactions in rock matrices can impact chlorinated ethene uptake, and ultimately back-diffusion timeframes.

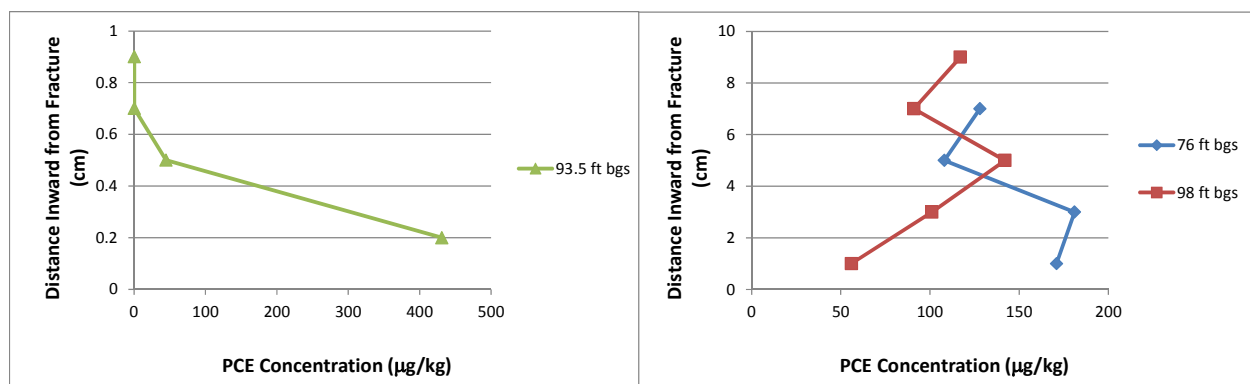


Figure 4.6. PCE concentration profile into the rock matrices for Loring AFB (left) and Edwards AFB (right). The limestone rock collected at Loring AFB exhibited significant abiotic PCE dechlorination, while the granite rock collected at Edwards AFB exhibited negligible abiotic PCE dechlorination (see Figure 4.6.1 below).

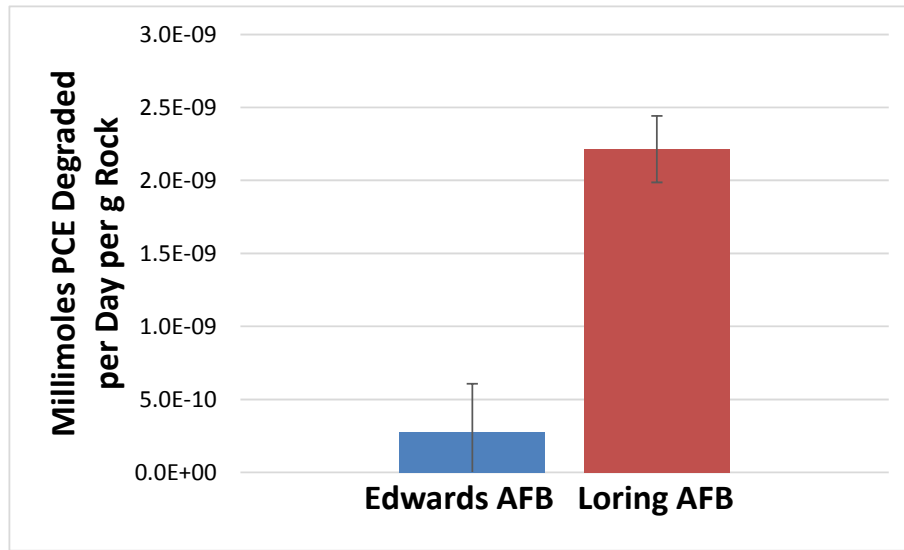


Figure 4.6.1. Abiotic PCE degradation rates for Edwards Air Force Base (through 13 days) and Loring AFB (through 14 days). The averages of triplicate samples are shown. Error bars represent 95% confidence intervals. PCE degradation was based on the sum of measured daughter products (sum of ethene, ethane, acetylene, and propane).

We have demonstrated in our laboratory that TCE abiotic reactions may be occurring in many bedrock matrices despite decades of exposure to TCE, and preliminary evidence suggests that these reactions impact TCE uptake in rock matrices. These abiotic degradation rates were observed for multiple rock types, suggesting that contaminant storage in rock matrices may persist far less than what is currently believed, and may help make a monitored natural attenuation (MNA) approach feasible.

4.7 Assessment of Abiotic Reaction with EDB.

4.7.1 Batch testing

Results for the batch experiments with EDB to evaluate the sorption and reaction to the JB Kwik epoxy showed that JB Kwik epoxy had a significant reaction with EDB with approximately 3.8×10^{-5} mmole ethane, ethene, and propane being generated in the batch experiments. This dehalogenation reaction with the epoxy was unexpected, especially when considering that the reaction between TCE and the epoxy were negligible compared to the TCE reaction with the rock. Because of this reaction between the EDB and epoxy, the coupled diffusion and reaction experiments using rock “rods” were performed without epoxy, thereby exposing the entire

surface area of the rock to the EDB solution. In applying our diffusion and reaction model, the total surface area of the rock was used, where migration (and coupled dehalogenation reaction) of the EDB occurred radially inwards into the rock rod. Because the EDB diffusion distance into the rock was small (i.e., < the effective radius of the rock), our model could be applied without any modifications to the boundary conditions.

4.7.2 Reaction Cell experiments - EDB

Daughter product generation from the dehalogenation of EDB was measured in both the light gray mudstone and the red sandstone. Testing through 43 days is shown in Figures 4.7.2 (light gray mudstone) and 4.7.3 (red sandstone), where the molar sum of the measured daughter products is shown. Ethene was the dominant daughter product for each rock type, although daughter product generation in the red sandstone was minimal compared to that observed in the light gray mudstone. The relatively low extent of dehalogenation observed in the red sandstone relative to the light gray mudstone is consistent with the TCE data, and suggests that the available ferrous iron in these rocks is responsible for the observed EDB dehalogenation.

Using our developed coupled diffusion and first-order reaction model for TCE in rock matrices, along with the previously measured diffusion coefficient of TCE through the light gray mudstone ($6.5 \pm 2.0 \times 10^{-8}$), bulk first-order EDB abiotic degradation rate constants (defined as the first order rate constant multiplied by the linear sorption coefficient and the rock density) were regressed to the measured daughter product generation (ethane, ethene, and propane) in the bottles; this regression was only performed for the light gray mudstone, since daughter product generation throughout the 43 day study for the red sandstone was negligible. The regressed first order bulk rate constant (Eq. 3.9.2.3) for the light gray mudstone, averaged for the duplicate samples, was $1.2 \times 10^{-8} \text{ s}^{-1}$. To calculate this rate constant, the K_d value for EDB was estimated by multiplying the value of K_d for TCE in the light gray mudstone (0.15 L/kg) by the K_{OC} ratio for EDB:TCE (0.084) (based on USEPA Sol Screening Guidance: User's Guide 9366.4-23, 1996). The resultant K_d value for EDB in the light gray mudstone was 0.0126 L/kg, which was multiplied by the first order reaction rate constant (Eq. 3.9.2.1 regressed to the experimental data) to attain the first order bulk rate constant of $1.2 \times 10^{-8} \text{ s}^{-1}$. Our results for EDB are consistent with previous studies that have shown that EDB degrades via dihaloelimination to ethene in the presence of iron-sulfur species (Kuder et al. 2012).

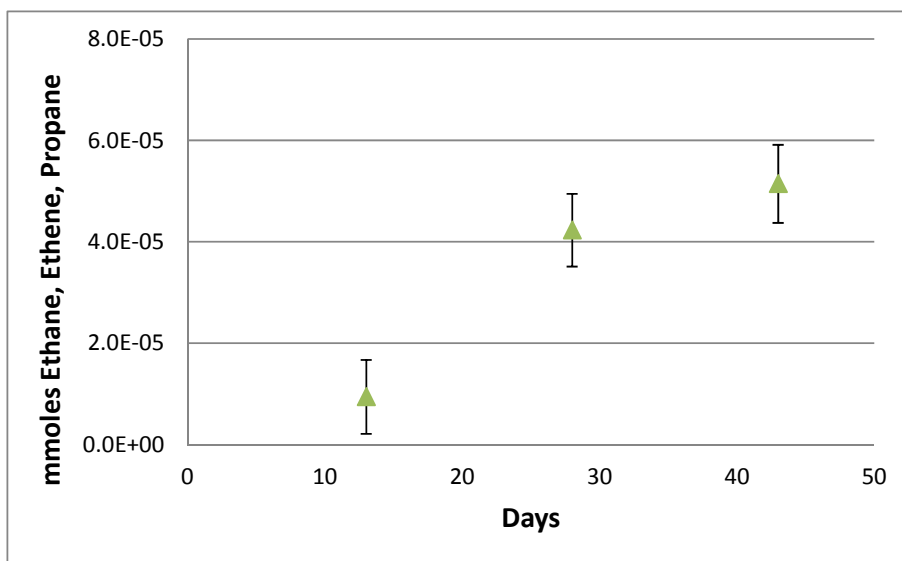


Figure 4.7.2. The sum of ethene, ethane, and propane generation from abiotic EDB degradation for the light gray mudstone. Ethene was the most abundant daughter product, accounting for greater than 90% of the molar sum of dehalogenated daughter products. Error bars represent 95% confidence intervals.

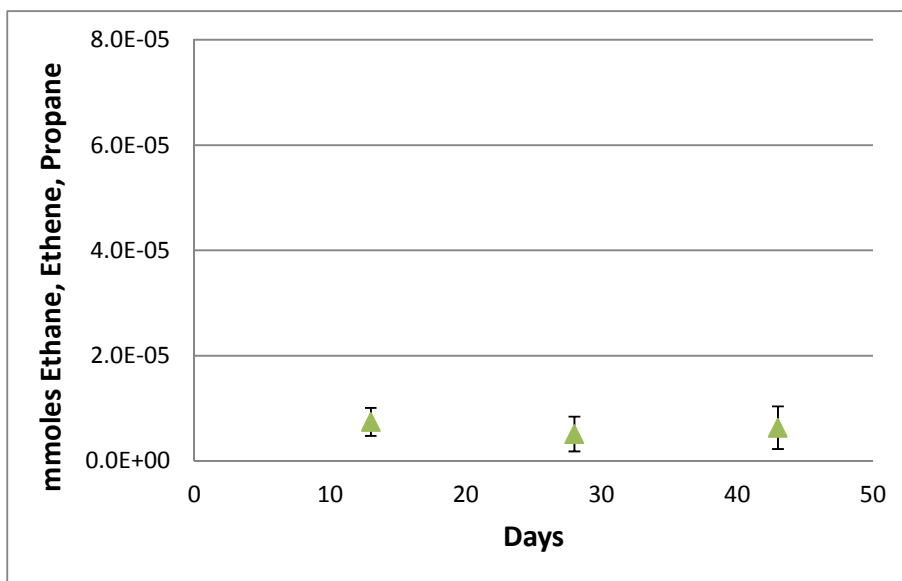


Figure 4.7.3. The sum of ethene, ethane, and propane generation from abiotic EDB degradation for the red sandstone. Sustained dehalogenation activity was not observed, and daughter product generation was minimal, indicating that EDB abiotic dehalogenation in this low ferrous iron content rock was negligible. Error bars represent 95% confidence intervals.

5.0 Conclusions and Implications for Future Research/Implementation

To the best of our knowledge, this research project was the first detailed study to evaluate the coupled diffusion and reaction processes of TCE in intact rock matrices. Both diffusion and reaction processes were investigated as a function of rock mineralogy, and the impact of these processes on TCE uptake into rock matrices was assessed. ***Key findings from this research include the following:***

- Mineral bedding can have a substantial impact on the effective diffusion coefficient of contaminants and other solutes through the rock matrix. Using SEM techniques to provide a 2-D estimate of the porosity in the orientation of the diffusion gradient, along with a simple empirical correlation, the effective diffusion coefficient can be predicted with respect to mineral bedding orientation. This improved method of determining the effective diffusion coefficient in rock matrices will facilitate substantial improvements in fractured bedrock aquifer scale models that predict matrix back-diffusion timeframes and overall plume longevity.
- Ferrous minerals present in rock matrices can facilitate the abiotic dechlorination of TCE (and PCE). While these dechlorination reactions are slow compared to the dechlorination rates typically considered useful for natural attenuation, these dechlorination reactions have a substantial impact on contaminant fate and transport in rock matrices, as these rates are large compared to the length and diffusional time scales associated with typical rock matrices.
- The abiotic dechlorination reactions noted above are on-going in rock that has been exposed to TCE *in situ* for decades, thus verifying that these abiotic reactions likely are an important attenuation mechanism at many fractured bedrock sites where ferrous minerals are present in the rock matrix.
- The magnitude of these abiotic dechlorination reactions are related to the “available” ferrous iron content of the rock, which is the ferrous iron content in direct contact with the rock porosity.
- Oxidants such as persulfate and permanganate are unlikely to be effective for treating contaminant mass within the rock matrix, as the rock matrix oxidant demand likely will limit oxidant migration into the rock to several hundred microns. The exception may be rock with extremely low oxidant demand, where oxidant migration into rock matrices may occur much more rapidly and effectively treat TCE.
- Mineral precipitates formed at the fracture-matrix interface, after prolonged exposure to permanganate or persulfate, did not serve as a physical barrier to diffusion through the

rock. Thus, our data suggest that chemical oxidants are unlikely to mitigate back-diffusion.

- EDB, a brominated ethane, also was shown to undergo abiotic dehalogenation in rock matrices. This suggests that several classes of halogenated compounds may be amenable to the abiotic dehalogenation reactions observed in this study.

We believe these key findings have great importance in our understanding of chlorinated ethene plumes in fractured bedrock. Perhaps the most significant finding was the identification and quantification of the naturally occurring abiotic dechlorination reactions that occur under anoxic conditions. This important natural attenuation mechanism will likely impact how these plumes are managed, and may serve as a means to justify an MNA approach at bedrock sites where these dechlorination reactions are occurring.

While this research has yielded some important and exciting results, there remain many fundamental and applied questions that need to be addressed in future studies. These questions and issues include the following:

- *How many fractured bedrock sites impacted by chlorinated ethenes have these naturally occurring abiotic dechlorination reactions occurring?* Through this SERDP project, as well as ongoing efforts on ESTCP and remedial bedrock projects, we have identified 4 sites (NAWC, Calf Pasture Point, Pease AFB, and Loring AFB) where these reactions are occurring; one site (Edwards AFB) did not exhibit such beneficial dechlorination reactions. It remains unclear what percentage of DoD bedrock sites benefit from these dechlorination reactions.
- *What specific ferrous minerals are responsible for the observed dechlorination reactions?* While our current work has attributed the observed dechlorination reaction to the “available” (i.e., in direct contact with the rock porosity) ferrous iron content, it remains unclear as to which ferrous minerals are controlling the dechlorination reactions. Further studies to determine the specific minerals responsible for these reactions will improve our ability to predict, and possibly enhance, these reactions.
- *How do geochemical conditions impact these observed abiotic dechlorination reactions?* Our experiments investigating TCE dechlorination in the rock matrices were performed under anoxic conditions. The presence of dissolved oxygen likely will have a substantial impact on these reactions. In addition, dissolved oxygen may interact with ferrous minerals, potentially generating hydroxyl radicals. Changes in pH, which may result due to implementation of remedial technologies to treat TCE in conductive fractures, also may impact these dechlorination reactions, at least near the fracture-matrix interface.

- *What impacts will biostimulation/bioaugmentation for treatment of chlorinated ethenes have on these abiotic reactions?* Biologically induced reducing condition, and the formation of iron sulfide species, may have a substantial impact on the rock mineralogy near the matrix-fracture interface. Understanding how biostimulation/bioaugmentation impacts mineralogy, and subsequently impacts abiotic dechlorination rates, currently is unknown.
- *Can the relatively slow (but relevant with respect to MNA timeframes) abiotic dechlorination rates we have observed in the rock matrices be enhanced?* The first order rate constants for TCE dechlorination measured in this study demonstrate an important natural attenuation mechanism for (potentially) many bedrock sites. Identifying and demonstrating cost-effective methods to enhance these naturally occurring rates to remove contaminant mass in the rock matrix in typical remedial timeframes (i.e., 1 to 5 years) would provide a great benefit to the DoD and other stakeholders.
- *What other contaminants are amenable to abiotic treatment via these ferrous iron-induced reactions?* While we have demonstrated useful rates of dehalogenation reactions for PCE, TCE, and EDB, the extent to which other contaminants of concern are amenable to abiotic degradation or treatment in rock matrices has (to the best of our knowledge) not been examined. Heavy metals, radionuclides, nitrate, and other halogenated organic contaminants are among the compounds that are likely of most interest to the DoD, DoE, and USEPA.

We believe addressing these questions are among the logical next steps in addressing the most pressing and pertinent future research needs. As the technical challenges and elevated costs associated with managing fractured bedrock sites continue to be one of the top environmental issues facing the both the DoD and environmental industry as a whole, efforts to capitalize on these intrinsic remedial processes will likely continue to prove beneficial.

.....

6.0 Literature Cited

1. Arnold, W.A.; A.L. Roberts. Pathways and kinetics of chlorinated ethylene and chlorinated acetylene reaction with Fe(0) particles. *Environ. Sci. Technol.* 2000, 34, 1794-1805.
2. Audi-Miró, C., Cretnik, S., Otero, N., Palau, J., Shouakar-Stash, O., Soler, A., Elsner, M. 2013. Cl and C isotope analysis to assess the effectiveness of chlorinated ethene degradation by zero-valent iron: Evidence from dual element and product isotope values. *Appl. Geochem.* 32, 175-183.
3. Boving, T.B., Grathwohl, P., 2001. Tracer diffusion coefficients in sedimentary rocks: correlation to porosity and hydraulic conductivity. *Journal of Contaminant Hydrology* 53, 85–100.
4. Brown, R.A.; Wilson, J.T.; Ferrey, M. Monitored natural attenuation forum: the case for abiotic MNA. *Remed. J.* 2007, 17, 127-137.
5. Butler, E.C., Hayes, K.F., 1999. Kinetics of the transformation of trichloroethylene and tetrachloroethylene by iron sulfide. *Environ. Sci. Technol.* 33, 2021-2027.
6. Butler, E.C.; Hayes, K.F., 2001. Factors influencing rates and products in the transformation of trichloroethylene by iron sulfide and metal. *Environ. Sci. Technol.* 35, 3884-3891.
7. Chapman, S.W.; Parker, B.L., 2005. Plume persistence due to aquitard back diffusion following dense nonaqueous phase liquid source removal or isolation. *Wat. Resour. Res.* 41, 1-17.
8. Cavé, L., Al, T., Xiang, Y., Loomer, D., 2010. Investigations of diffusive transport processes in sedimentary rock. Nuclear Waste Management Organization, TR-2010-04, Toronto, Ontario, CA.
9. Chapman, S.W.; Parker, B.L., 2005. Plume persistence due to aquitard back diffusion following dense nonaqueous phase liquid source removal or isolation. *Wat. Resour. Res.*, 41, 1-17.
10. Conrad, S.H., Glass, R.J. and Peplinski, W.J., 2002. Bench-scale visualization of DNAPL remediation processes in analog heterogeneous aquifers: surfactant floods and in situ oxidation using permanganate. *Journal of Contaminant Hydrology*, 58(1-2): 13-49.
11. Crank, J. 1995. *The Mathematics of Diffusion*. Second edition. Oxford Science Publications.
12. Crimi, M., Siegrist, R., 2004. Impact of reaction conditions on genesis during permanganate oxidation. *J. Environ. Eng.* 130 (5), 562–572.
13. Cussler, E.L. *Diffusion – mass transfer in fluid systems*, Cambridge University Press. 1984.
14. Darlington, R.; Lehmicke, L.G.; Andrachek, R.G.; Freedman, D.L., 2013. Anaerobic abiotic transformations of cis-1,2-dichloroethene in fractured sandstone. *Chemosphere*, 90, 2226-2232.
15. De Bruin, W.P., Kotterman, M.J., Posthumus, M.A., Schraa, G., Zehnder, A.J., 1992. Complete biological reductive transformation of tetrachloroethene to ethane. *Appl. Environ. Microbiol.* 58, 1996–2000.
16. Desbois, G., Urai, J.L., De Craen, M., 2010. In-situ and direct characterization of porosity in Boom Clay (Mol site, Belgium) by using novel combination of ion beam cross-sectioning, SEM and cryogenic methods. External Report of the Belgian Nuclear Research Centre10/MDC/P-26, ISSN 1782-2335. .

17. Descostes, M., Blin, V., Bazer-Bachi, F., Meier, P., Grenut, B., Radwan, J., Schlegel, M.L., Bruschaert, S., Coelho, D., Tevissen, E., 2008. Diffusion of anionic species in Callovo-Oxfordian argillites and Oxfordian limestones (Meuse/Haute-Marne, France). *Appl. Geochem.* 23, 655-677.
18. Dullien, F.A.L., 1992. *Porous Media — Fluid Transport and Pore Structure*. 526 Academic Press, Inc., San Diego, CA.
19. Durrance, E.M., Meads, R.E., Ballard, R.R.B., Walsh, J.N., 1978. Oxidation state of iron in the Kittleham Mudstone Formation of the New Red Sandstone series (Permian-Triassic) of southeast Devon, England. *Geol. Soc. Amer. Bulletin* 89, 1231-1240.
20. Elsner, M., Chartrand, M., VanStone, N., Couloume, G.L., Sherwood Lollar, B., 2008. Identifying abiotic chlorinated ethene degradation: Characteristic isotope patterns in reaction products with nanoscale zero-valent iron. *Environ. Sci. Technol.* 42, 5963-5970.
21. Esteban, L., Géraud, Y., Bouchez, J.L., 2006. Pore network connectivity anisotropy in Jurassic argillite specimens from eastern Paris Basin (France). *Phys. Chem. Earth* 32, 161-169.
22. Ferrey, M.L.; Wilkin, R.T.; Ford, R.G.; Wilson, J.T., 2004. Nonbiological removal of cis-dichloroethylene and 1,1-dichloroethylene in aquifer sediment containing magnetite. *Environ. Sci. Technol.* 38, 1746-1752.
23. Fetter, C.W. *Contaminant Hydrogeology*, Prentice-Hall, Inc., 1999.
24. Goldstein, K.J., Vitolins, A.R., Navon, D., Parker, B.L., Chapman, S., Anderson, G.A., 2004. Characterization and pilot scale studies for chemical oxidation remediation of fractured shale. *Remediation Journal* 14, 19–37.
25. Gunasekaran, S., Anbalagan, G., 2008. Optical absorption and EPR studies on some natural carbonate minerals. *Spectrochim. Acta A Mol. Biomol. Spectrosc.* 69 (2), 383–390.
26. Hartog, N., Griffioen, J. and van der Weijden, C.H., 2002. Distribution and Reactivity of O₂-Reducing Components in Sediments from a Layered Aquifer. *Environmental Science & Technology*, 36(11): 2338-2344.
27. He, Y.T.; Wilson, J.T.; Wilkin, R.T., 2010. Impact of iron sulfide transformation on trichloroethylene degradation. *Geochimica Cosmochimica Acta*, 74, 2025-2039.
28. Hønning, J., Broholm, M.M. and Bjerg, P.L., 2007a. Quantification of potassium permanganate consumption and PCE oxidation in subsurface materials. *Journal of Contaminant Hydrology*, 90(3-4): 221-239.
29. Hønning, J., Broholm, M.M. and Bjerg, P.L., 2007b. Role of Diffusion in Chemical Oxidation of PCE in a Dual Permeability System. *Environmental Science & Technology*, 41(24): 8426-8432.
30. Huq, A; Wood, T. Diffusion coefficient of ethylene gas in water. *J. Chem. Eng. Data* 1968, 13, 256-259.
31. Kennedy, M.J., Pevear, D.R. and Hill, R.J., 2002. Mineral Surface Control of Organic Carbon in Black Shale. *Science*, 295(5555): 657-660.
32. Koene-Cottaar, F.H.M., Schraa, G., 1998. Anaerobic reduction of ethene to ethane in an enrichment culture. *FEMS Microbiol. Ecol.* 25, 251–256.
33. Krembs, F.J., Siegrist, R.L., Crimi, M.L., Furrer, R.F. and Petri, B.G., 2010. ISCO for Groundwater Remediation: Analysis of Field Applications and Performance. *Ground Water Monitoring & Remediation*, 30(4): 42-53.

34. Kuder, T., Wilson, J., Philp, P., & He, Y. (n.d.), 2012. Carbon Isotope Fractionation in Reactions of 1,2-Dibromoethane with FeS and Hydrogen Sulfide. *Environmental Science & Technology*, 46(14), 7495-7502.
35. Kyriacou, G., Vadgama, P. and Wang, W., 2006. Characterization of a laminar flow cell for the prevention of biosensor fouling. *Medical Engineering & Physics*, 28(10): 989-998.
36. Lacombe, P.J., Burton, W.C., 2010. Hydrogeologic framework of fractured sedimentary rock, Newark Basin, New Jersey. *Ground Water Mon. Remed.* 30,35–45.
37. Lanser, D.; Verwer, J.G. Analysis of operator splitting for advection-diffusion-reaction problems from air pollution modelling. *J. Comp. Appl. Math.* 1999, 111, 201-216.
38. Lee, W.; Batchelor, B., 2002. Abiotic reductive dechlorination of chlorinated ethylenes by iron-bearing soil minerals. 1. Pyrite and Magnetite. *Environ. Sci. Technol.*, 36, 5147-5154.
39. Lee, W.; Batchelor, B., 2003. Reductive capacity of natural reductants. *Environ. Sci. Technol.*, 37, 535-541.
40. Li, X.D., Schwartz, F.W., 2004. DNAPL remediation with in situ chemical oxidation using potassium permanganate: part I. Mineralogy of Mn oxide and its dissolution in organic acids. *J. Contam. Hydrol.* 68 (1–2), 39–53.
41. Liang, X.; Philip, R.P.; Butler, E.C., 2009. Kinetic and isotope analyses of tetrachloroethylene and trichloroethylene degradation by model Fe(II)-bearing minerals. *Chemosphere*, 75, 63-69.
42. Lipson, D.S., Kueper, B.H., Gefell, M.J., 2005. Matrix diffusion-derived plume attenuation in fractured bedrock. *Ground Water* 43, 30-39.
43. Liu, Y., Majetich, S.A., Tilton, R.D., Sholl, D.S., Lowry, G.V., 2005. TCE dechlorination rates, pathways, and efficiency of nanoscale iron particles with different properties. *Environ. Sci. Technol.*, 39, 1338-1345.
44. Lojkasek-Lima, P., Aravena, R., Parker, B. L. and Cherry, J. A., 2012, Fingerprinting TCE in a Bedrock Aquifer Using Compound-Specific Isotope Analysis. *Ground Water*, 50: 754–764.
45. Loomer, D.B., Al, T.A., Banks, V.J., Parker, B.L. and Mayer, K.U., 2010. Manganese Valence in Oxides Formed from in Situ Chemical Oxidation of TCE by KMnO₄. *Environmental Science & Technology*, 44(15): 5934-5939.
46. Macquaker, J.H.S., Curtis, C.D., Coleman, M.L., 1997. The role of iron in mudstone diagenesis: comparison of Kimmeridge Clay Formation mudstones from onshore and offshore (UKCS) localities. *J. Sediment. Res.* 67, 871-878.
47. Mutch, R.D.; Scott, J.I.; Wilson, D.J., 1993. Cleanup of fractured rock aquifers: implications of matrix diffusion. *Environ. Monitor. Assess.*, 24, 45-70.
48. Nakashima, Y., Kamiya, S., Nakano, T., 2008. Diffusion ellipsoids of anisotropic porous rocks calculated by X-ray computed tomography-based random walk simulations. *Wat. Resour. Res.* 44, article number W12435.
49. O’Loughlin, E.O.; Burris, D.R., 2003. Reduction of halogenated ethanes by green rust. *Environ. Tox. Chem.*, 23, 41-48.
50. Pham, H.T.; Kitsuneduka, M.; Hara, J.; Suto, K.; Inoue, C., 2008. Trichloroethylene transformation by natural mineral pyrite: the deciding role of oxygen. *Environ. Sci. Technol.*, 42, 7470-7475.
51. Pingitore, N.E., 1978. The behavior of Zn ²⁺ and Mn ²⁺ during carbonate diagenesis; theory and applications. *J. Sediment. Res.* 48 (3), 799–814.

52. Roberts, A.L.; Totten, L.A.; Arnold, W.A.; Burris, D.R.; Campbell, T.J., 1996. Reductive elimination of chlorinated ethylenes by zero-valent metals. *Environ. Sci. Technol.*, 30, 2654-2659.
53. Samper, J., Yang, C., Naves, A., Yllera, A., Hernández, A., Molinero, J., Soler, J.M., Hernán, P., Mayor, J.C., Astudillo, J., 2006. A fully 3-D anisotropic numerical model of the DI-B in situ diffusion experiment in the Opalinus clay formation. *Phys. Chem. Earth.* 31, 531-540.
54. Saruwatari, K.; Kameda, J.; Tanaka, H., 2004. Generation of hydrogen ion and hydrogen gas in quartz-water crushing experiments: an example of chemical processes in active faults. *Phys Chem. Mineral.*, 31, 176-182.
55. Sato, H., Suzuki, S., 2003. Fundamental study on the effect of an orientation of clay particles on diffusion pathway in compacted bentonite. *Applied Clay Science* 23, 51–60.
56. Schaefer, C.E., Condee, C.W., Vainberg, S., Steffan, R.J., 2009. Bioaugmentation for Chlorinated Ethenes using *Dehalococcoides* sp.: comparison between batch and column experiments. *Chemosphere* 75, 141–148.
57. Schaefer, C.E., Lippincott, D., Steffan, R.J., 2010. Field scale evaluation of bioaugmentation dosage for treating chlorinated ethenes. *Ground Water Monit. Rem.* 30, 113–124.
58. Schaefer, C.E., Towne, R.M., Lazouskaya, V., Bishop, M.E., Dong, H., 2012. Diffusive flux and pore anisotropy in sedimentary rocks. *J. Contam. Hydrol.* 131, 1–8.
59. Schaefer, C.E., Towne, R.M., Lippincott, D.R., Lazouskaya, V., Fischer, T.B., Bishop, M.E., Dong, H., 2013. Coupled diffusion and abiotic reaction of trichloroethene in minimally disturbed rock matrices. *Environ. Sci. Technol.* 47, 4291–4298.
60. Scherer, M.M.; O’Loughlin, E.; Parkin, G.F.; Valentine, R.; Al-Hosney, H.; Handler, H.; Just, C.; Larese-Casanova, P.; Pasakarnis, T.; Smith, S.L. 2007. Sustainability of long-term abiotic attenuation of chlorinated ethenes. Final report submitted to the Strategic Environmental Research and Development Program. September.
61. Schrick, B., Blough, J.L., Jones, A.D., Mallouk, T.E. 2002. Hydrodechlorination of trichloroethylene to hydrocarbons using bimetallic nickel-iron nanoparticles. *Chem. Mater.* 14, 5140-5147.
62. Scott, D., Apblett, A. and Materer, N.F., 2011. Follow-up study on the effects on well chemistry from biological and chemical remediation of chlorinated solvents. *Journal of Environmental Monitoring*, 13(9): 2521-2526.
63. Seyedabbasi, M.A.; Newell, C.J.; Adamson, D.T.; Sale, T.C., 2012. Relative contribution of DNAPL dissolution and matrix diffusion to the long-term persistence of chlorinated solvent source zones. *J. Contam. Hydrol.*, 134-135, 69-81.
64. Siegrist, R.L., Crimi, M., & Simpkin, T. J. (Eds.), 2011. *In situ chemical oxidation for groundwater remediation* (Vol. 3). Springer Science + Business Media, New York.
65. Siitari-Kauppi, M., Lindberg, A., Hellmuth, K.H., Timonen, J., Vaatainen, K., Hartikainen, J., and Hartikainen, K. (1997) The effect of microscale pore structure on matrix diffusion a site-specific study on toaite, *J. Contam. Hydrol.*, 26, 147-158.
66. Sterling, S.N.; Parker, B.L.; Cherry, J.A.; Williams, J.H.; Lane Jr., J.W.; Haeni, F.P., 2005. Vertical cross contamination of trichloroethylene in a borehole in fractured sandstone. *Ground Water.* 43, 557-573.
67. Stucki, J. W.; Golden, D. C.; Roth, C. B., 1984. The preparation and handling of dithionite reduced smectite suspensions. *Clays Clay Miner.*, 32, 191-197.

68. Szecsody, J.; Williams, M.; Fruchter, J.; Vermeul, V.; Sklarew, D., 2004. In Situ reduction of aquifer sediments: enhancement of reactive iron phases and TCE dechlorination. *Environ. Sci. Technol.*, 38, 4656-4663.
69. Tratnyek, P.G.; Wolfe, N.L., 1993. Oxidation and acidification of anaerobic sediment-water systems by autoclaving. *J. Environ. Qual.*, 22, 375-378.
70. Van Loon, L.R., Soler, J.M., Muller, W., Bradbury, M.H., 2004. Anisotropic diffusion in layered argillaceous rocks: A case study with Opalinus Clay. *Environ. Sci. Technol.* 38, 5721-5728.
71. United States Environmental Protection Agency (USEPA). Soil Screening Guidance: User's Guide. Publication 9355.4-23, 1996.
72. Weerasooriya, R.; Dharmasena, B., 2001. Pyrite-assisted degradation of trichloroethene (TCE). *Chemosphere*, 42, 389-396.
73. Wersin, P., Van Loon, L.R., Soler, J.M., Yllera, A., Eikenberg, J., Gimmi, T., Hernan, P., Boisson, J.Y., 2004. Long-term diffusion experiments at Mont. Terri: first results from
74. West, M.R.; Kueper, B.H., 2010. Plume detachment and recession times in fractured rock. *Ground Water*, 48, 416-426.
75. Worthington, P.F., 2001. The influence of formation anisotropy upon resistivity–porosity relationships. *Petrophysics* 42, 83–92
76. Xu, X. and Thomson, N.R., 2009. A long-term bench-scale investigation of permanganate consumption by aquifer materials. *Journal of Contaminant Hydrology*, 110(3–4): 73-86.
77. Yang, Y., Aplin, A.C., 2010. A permeability-porosity relationship for mudstones. *Marine Petrol. Geology*, 27, 1692-1697.
78. Yokoyama, T., Nakashima, S., 2005. Diffusivity anisotropy in a rhyolite and its relation to pore structure. *Engineering Geology* 80, 328–335.
79. Zhang, H., Schwartz, F.W., 2000. Simulating the in situ oxidative treatment of chlorinated ethylenes by potassium permanganate. *Water Resour. Res.* 36 (10), 3031–3042.

APPENDIX A: Supporting Data

A.1 Diffusion in Anisotropic Rock Matrices

Applying the relationship indicated in Section 3.9.1 Eq. 3.9.1, the effective diffusion coefficient divided by the iodide aqueous diffusivity ($2.0 \times 10^{-5} \text{ cm}^2/\text{sec}$) (Cussler, 1984) is plotted versus the water accessible porosity measured via water uptake, similar to the approach employed by Boving and Grathwohl (2001) (Figure A.1). Examination of Figure A.1 reveals that the model does not provide a good prediction of the experimental data, with model predictions varying by up to an order of magnitude from experimental results. There also does not appear to be any correlation between water uptake porosity and the effective diffusion coefficient for the rock samples used in this study. In addition, the modeling approach of Eq. 3.9.1 does not describe the substantial differences in the diffusion as a function of orientation that was observed in some of the rock types.

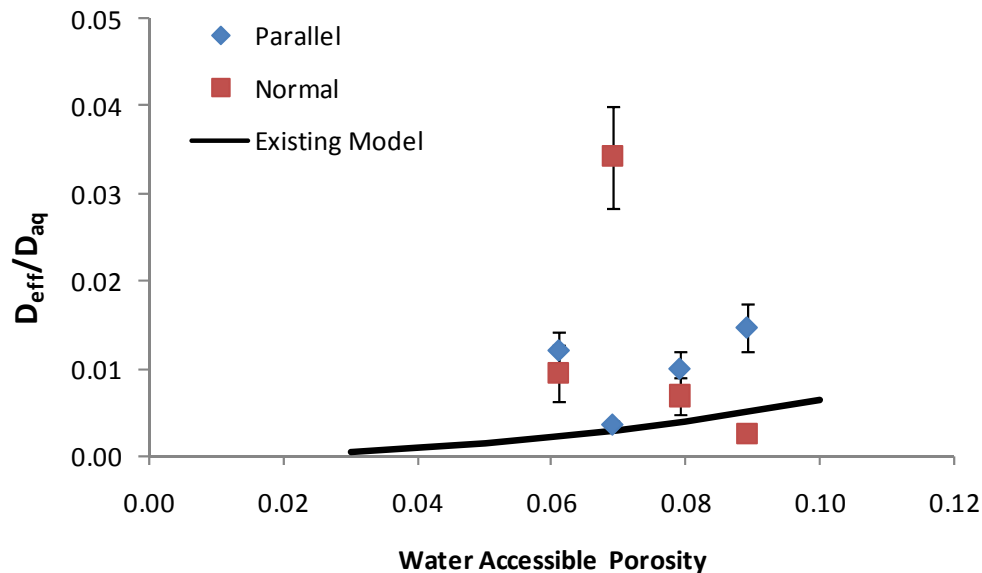


Figure A.1 Prediction of the experimental data using Eq. 3.9.1 presented in Section 3.9.1. (existing model based on Boving and Grathwohl (2001)). Error bars represent the standard error.

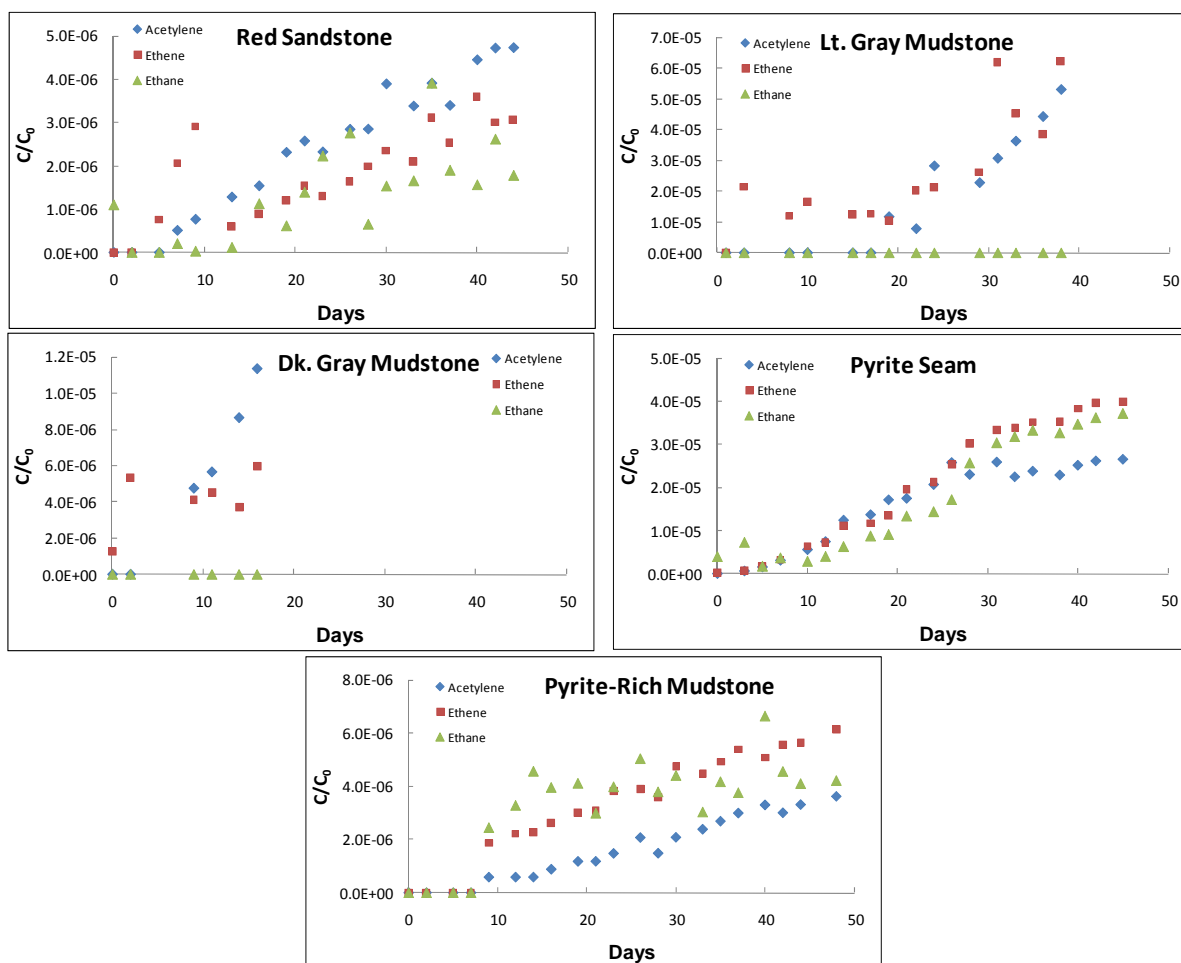


Figure A.2. Generation of acetylene, ethene, and ethane shown for one experiment for each rock type. Gas concentrations are shown as the molar fraction of the initial TCE concentration in the source side of the diffusion cell. Daughter product concentrations are plotted relative to the source side initial TCE concentration (molar basis).

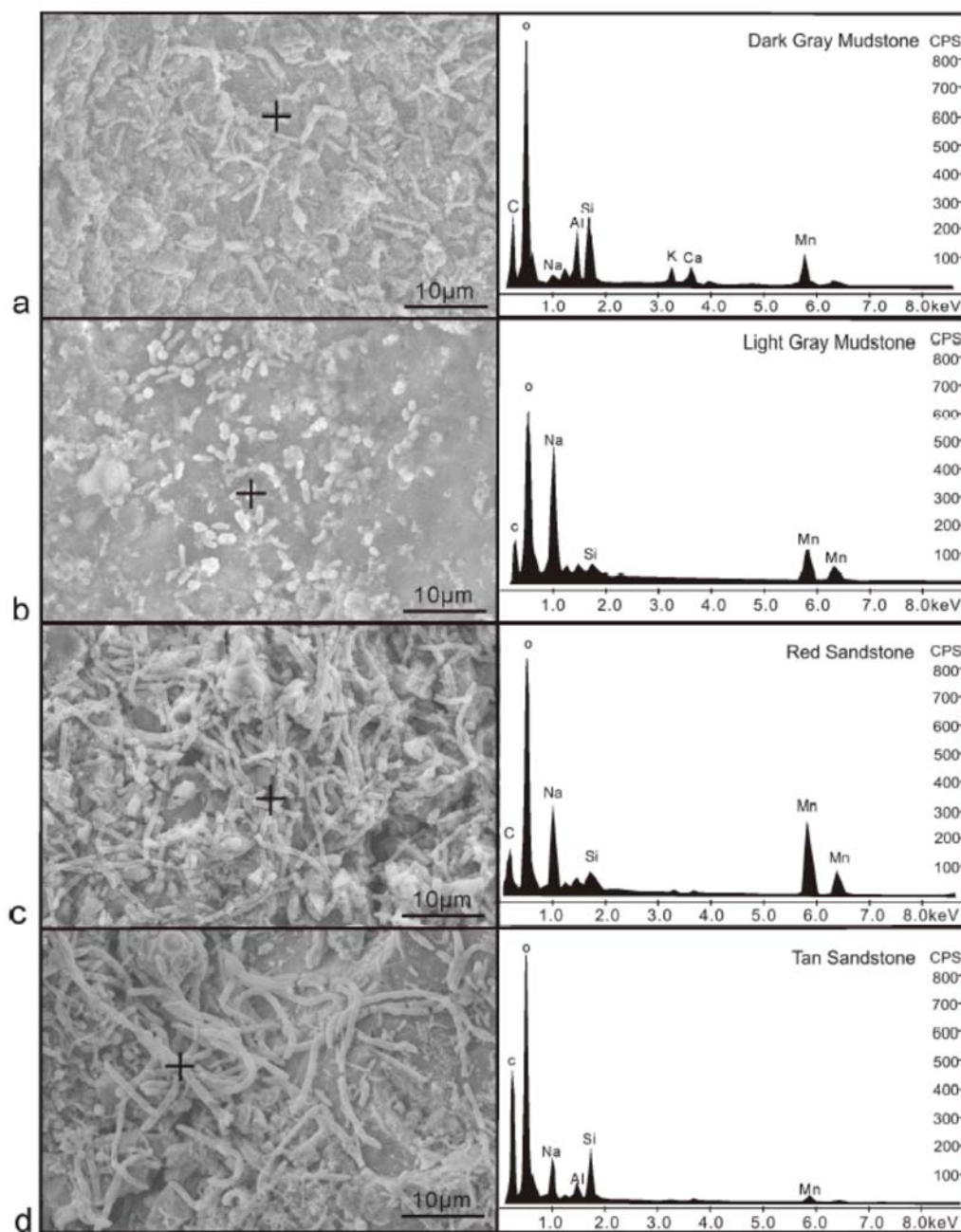


Figure A.3. SEM images (left) and EDS spectra (right) of permanganate-reacted surfaces on different sedimentary rocks, including dark gray mudstone (a), light gray mudstone (b), red sandstone (c), and tan sandstone (d). The plus signs on the images mark the location from which EDS spectra were obtained, indicating the formation of Mn mineral precipitates, such as birnessite and manganocalcite.

APPENDIX B: LIST OF PUBLICATIONS

Articles in peer-reviewed journals

Schaefer, C.E., Towne, R.M., Lippincott, D.R., Lacombe, P., Bishop, M.E., Dong, H. (2014). Abiotic Dechlorination in Rock Matrices Impacted by Long-Term Exposure to TCE. *Chemosphere* 119, 744-749.

Huang, Q., Dong, H., Towne, R.M., Fischer, T.B., Schaefer, C.E. (2014). Permanganate Diffusion and Reaction in Sedimentary Rocks, *J. Contam. Hydrol.* 159, 36-46.

Schaefer, C.E., Towne, R.M., Lippincott, D.R., Lazouskaya, V., Fischer, T.B., Bishop, M.E., Dong, H. (2013). Coupled Diffusion and Abiotic Reaction of Trichloroethene in Minimally Disturbed Rock Matrices, *Environ. Sci. Technol.*, 47, 4291-4298.

Schaefer, C.E., Towne, R.M., Lazouskaya, V., Bishop, M.E., and Dong, H. (2012). Diffusive flux and pore anisotropy in sedimentary rocks. *J. Contam. Hydrol.* 131, 1-8.

Conference Presentations

Schaefer, C.E., Towne, R.M., Lazouskaya, V., Fischer, T. and Dong, H. (2011). Coupled diffusion and reaction processes in rock matrices. presented at the NGWA Fractured Rock Conference, Burlington, VT.

Schaefer, C.E., Towne, R.M., Lazouskaya, V., and Dong, H. (2012). Coupled diffusion and reaction processes of TCE in rock matrices. presented at the Battelle International Conference on Remediation of Chlorinated and Recalcitrant Compounds, Monterey, CA.

Schaefer, C.E., Towne, R.M., Lippincott, D.R., Lacombe, P., Huang, Q. and Dong, H. (2014). Naturally occurring abiotic reaction of TCE in rock matrices. presented at the Battelle International Conference on Remediation of Chlorinated and Recalcitrant Compounds, Monterey, CA.

Schaefer, C.E., Towne, R.M., Lippincott, D.R., Lacombe, P., Bishop, M., Fischer, M., and Dong, H. (2015). Processes impacting TCE uptake and back-diffusion in rock matrices. presented at the RemTEC conference in Westminster, CO.

***** 2013 SERDP Environmental Restoration Project of the Year*****